2023-08-01

Double cantilever beam mode-I testing validation in large-scale additive manufacturing carbon composite

Luis Alfonso Camacho
University of Texas at El Paso

DOUBLE CANTILEVER BEAM MODE-I TESTING VALIDATION IN LARGE-SCALE ADDITIVE MANUFACTURING CARBON COMPOSITE

LUIS ALFONSO CAMACHO
Master's Program in Mechanical Engineering

APPROVED:

David Espalin, Ph.D., Chair

Armanj Hasanyana, Ph.D.

Amid Lopes, Ph.D.

Stephen L. Crites, Jr., Ph.D.
Dean of the Graduate School

DOUBLE CANTILEVER BEAM MODEI TESTING VALIDATION IN LARGE-SCALE ADDITIVE MANUFACTURING CARBON COMPOSITE

by

LUIS ALFONSO CAMACHO, B.S.

THESIS

Presented to the Faculty of the Graduate School of

The University of Texas at El Paso

in Partial Fulfillment

of the Requirements

for the Degree of

MASTER OF SCIENCE

Department of Aerospace and Mechanical Engineering

THE UNIVERSITY OF TEXAS AT EL PASO

August 2023

Acknowledgements

I want to thank my parents, Juan Alfonso Camacho, and Margarita Cruz, for being a great support system, not only my time in college but throughout all my life, for instilling in me work ethic and honesty not only in my professional life but also to my intrapersonal and interpersonal development. Above all the people in this world it is you two that I want to make proud. Thank you to all my siblings, all five of them, for being a crucial factor in my upbringing and having a big impact on my cultural and personality development.

I also want to thank Dr. David Espalin for being there teaching me how to take steps in this academic and professional world. Holding my hand as I stumbled throughout this process, having patience whenever I messed up, and letting go when he trusted me to complete the task at hand. I know there are a lot of things he does for us students and want to state that I know that I am one witness of the fact that he truly cares, not only for our professional development but for our personal wellbeing. I hope I can make you proud to have been my mentor.

I want to thank my peers at the Keck Center's Cotton facilities and some from campus, and the friends I have made and kept throughout my college life. You have been a fountain of leisure time through rough patches but also cheered me on when work had to be done.

Finally, I want to thank, above all things, God for putting me in the right place at the right time. For not letting my life be what I wanted it to be but instead putting me through situations that have given me the tools to face the difficulties of professional, academic, and personal life.

'Quien que no vive para servir no sirve para vivir'

Abstract

Testing for mechanical properties for additive manufacturing has been based on already existing standards for traditional manufacturing methods. For composites in large scale additive manufacturing there is a research gap in bond strength and fracture toughness for a single layer interface. By using Double cantilever beam Mode I, this thesis manuscript validates testing parameters and protocols to describe the intricacies of ABS matrix 20 wt.% carbon filled composite, specifically on the layer-to-layer interface. Studies suggest that fracture toughness is sensitive to process parameters, like deflection speed and sharpened crack tip at the layer interface of BAAM 3D printed part and by observing the type of failure it was revealed what strain rate and what sample preparation protocols are optimal for repeatable results characterization of large-scale additive manufacturing parts.

Table of Contents

List of Figures

Chapter 1: Introduction

1.1. Background

The Big Area Additive Manufacturing (BAAM) machine is a material extrusion 3D printer capable of printing large scale polymer composite materials. Standards for testing the mechanical properties of additive manufacturing (AM) do not yet exist, although there are efforts to compile standards that are used as the basis for testing in AM (Forster, 2015). The focus of this investigation is large scale material extrusion (MEX) printing of composite material development and validation of testing protocols based on already existing polymer composite testing standards, and the characterization of the prints with the developed standards.

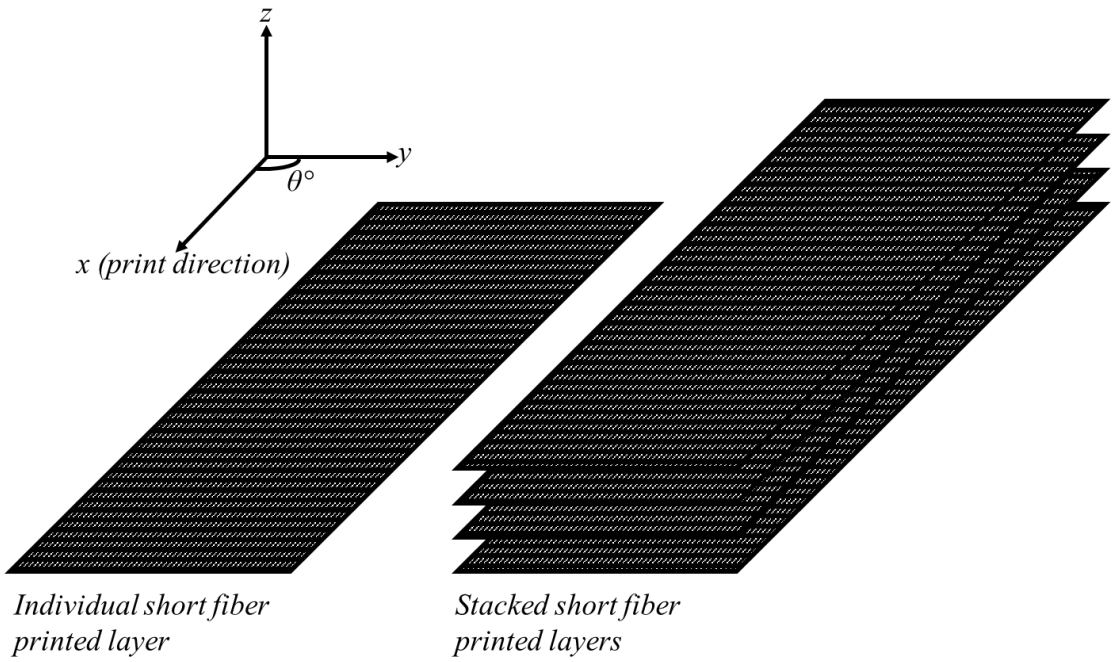

Figure 1 Matrix/fiber relation at the layer interface of a print.

For traditional manufacturing methods of polymer composites, mechanical testing standards are complex and depend on varied factors to effectively characterize mechanical properties. A reason for this is that composite materials are inherently anisotropic in their

mechanical properties, a challenge that is also present in MEX. Factors to be considered in testing for the mechanical properties of composite materials are fiber orientation, stacking sequence, and the continuity of fibers. From previous studies it is known that in large scale 3D printing there is some alignment of the short fibers to the printing direction at the layer interface (Billah et al., 2020; Kumar et al., 2021; Yang et al., 2021). Given this, it was assumed that the fiber orientation is unidirectional, this helped narrow down the search of a predetermined testing process to a standard that requires the samples to have fibers within the composite be unidirectional, which in this case is the double cantilever method. It is also important to note that due to deformation and shrinkage after dispensing the material adds a layer of complexity of the fiber orientation at the layer interface (Colón Quintana et al., 2022), also called nesting, which is a point of observation as it may impact the interaction at the layer interface. The stacking sequence is assumed to always be at 0° for every layer, in this case the reference axis being the printing direction and that fibers are short- or discontinued- as seen in Figure 1 Matrix/fiber relation at the layer interface of a print..

In older studies that looked at the impact of fibers in thermoplastics there was an increase in fracture toughness, that is, in the energy exerted to propagate a crack. Comparing it with traditional manufacturing techniques it seems that the phenomenon that best adheres to the failure at the layer interface is fiber bridging (Khan, 2019).

The double cantilever beam (DCB) method, based on the ASTM standard D5528, is used to test for fracture toughness. This is the standard of which the investigation uses to describe the layer interface behavior and the standard to be validated. Additionally, there is literature suggesting that different strain rates impact the average fracture toughness of the material (Smiley and Pipes, 1987). The range of the standard this investigation is based on suggests the strain rate to be between 1-5 mm/s. This study includes testing at different strain rates setting a precedent for future fracture

toughness testing and mechanical testing of large-scale AM prints. The test does require to have the specimen fracture specifically along a single layer interface, this is induced by having a built-in pre-crack, which will help with the validation of which strain rate or rates may be used for future testing processes development.

1.2. MOTIVATION

The study of fracture toughness in AM is not extensive, let alone in large-scale AM. This investigation focuses on the single interlayer characterization of fracture toughness, which can be used as an indicator of interlayer bond strength. Providing insight into the material capabilities and whether this is a controllable aspect. Offering an additional layer of tailoring of the material for specific applications and setting precedent for future standardization of additive manufacturing including specialized specimen geometry and strain rates. In addition to filling some knowledge gaps this paper also developed a novel approach on how fracture toughness is recorded, and the data processed by creating a MATLAB script that processed video and data after the test was complete.

Chapter 2: Literature Review

According to ISO/ASTM 52900, 'additive manufacturing (AM) is a term given to those technologies that sequentially joins material creating an object with the sequence being based on a 3D model data. There are different processes and within those processes there are technologies that focus on different applications and/or uses. Currently there are seven process categories that fall under AM. One of these processes, and the one this investigation focused on, is material extrusion (MEX) sometimes referred to its popular trademark name fused deposition modeling (FDM), which consists of selectively dispensing material through an orifice or nozzle. The MEX machine that is subject of this investigation is the Big Area Additive Manufacturing (BAAM) machine developed by Cincinnati Incorporated and Oak Ridge National Labs (ORNL), which, as the name suggests, is a large-scale additive manufacturing machine with a printing volume that falls within 140" x 65" x 72" (3.57 ×1.65 ×1.83 m^3) a nozzle diameter of 0.3 in, and the capability of printing 80 lbs/hr. (36.29 kg/hr.). The BAAM was designed to print composite and neat thermoplastics fed in the form of pellets. These pellets are first dried in a temperature controlled drier where the duration and temperature of the process varies depending on the material and its provider. Then they are fed to a hopper system that introduces pellets into screw-type plunger that pushes the material through a series of

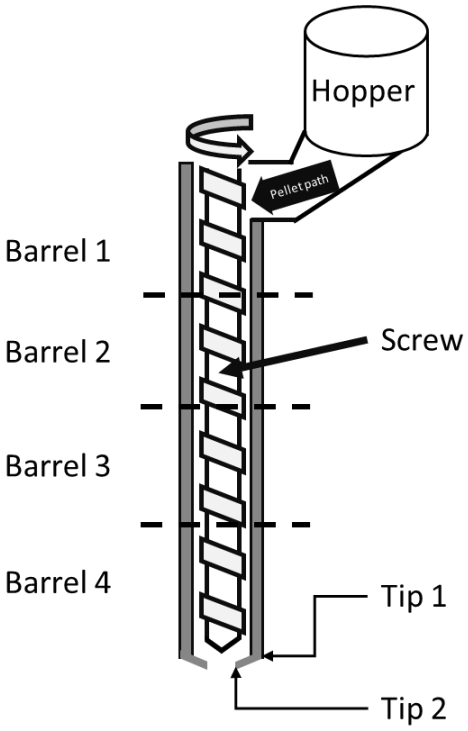

Figure 2 Extruder heated zones and hopper system.

heated zones, as shown in Figure 2 Extruder heated zones and hopper system, to have the material reach and exceed its transitioning-glass temperature and then dispense it through a nozzle.

2.1. LARGE-SCALE MATERIAL EXTRUSION

Material extrusion (MEX) in large-scale is a relatively new printing technology. Although Cincinnati and Oak Ridge National Lab's BAAM is the printer that was used for his investigation, there are other companies developing large-scale printers including, but not limited, Thermwood Corporation (Dale, IN) and Ingersoll Machine Tools (Rockford, IL). Tooling and molding are the main applications for this type of technology (Musio-Sale et al., 2020; Yeole et al., 2021). Other applications that it has been used for are developing vehicle powertrain prototype (Curran et al., 2016) and other uncited works that have applications like automotive fairing a chassis, architecture, furniture, and Rosenberg space habitat.

Printing in BAAM has a unique workflow that starts with designing and goes all the way to its post process. Compared with traditional (small-scale) MEX it is not encouraged to print with support given that support generation is not as intricate as traditional MEX where the support is easy to just break-off. It is worth mentioning that there have been attempts to have easy support removal by having a patterned ceramic powder applied that has both stability in the build but also prevents adhesion between layer as to have it easy break-off (Duty and Love, 2015). Compared to traditional MEX, large-scale printers are capable of printing at higher speeds due to higher material throughput, as mentioned before.

Printing with high material throughput does come at a cost which is a lower layer resolution. For comparison, the Stratasys Fortus400 with default parameters prints with a layer height of approximately 0.25 mm, the BAAM that was used in this investigation has printed at 3.5 mm layer height, which is fourteen times larger than the FDM printer. When it comes to printing,

manufacturers compensate for the lack of resolution by overprinting and machining excess material in the post-process to give smoother surfaces.

It is known that adding short fiber to the matrix increases its mechanical properties justifying the use of short fiber in printed composite material. In addition to improving mechanical properties, it has been found that short fibers help mitigate warpage and shrinkage that happen during building (Spoerk et al., 2018; Winter et al., 2022). Currently only short fiber composite materials for large scale are commercially available but there are attempts at printing continuous and long fiber on both large and traditional AM (Pappas et al., 2021; Yamawaki and Kouno, 2018).

There have been attempts to enhance the mechanical and structural properties of prints in large-scale AM apart from using composites. There are many factors that impact the quality of a print, some studies have recognized that the printed substrate needs to be around its transitioning glass temperature and avoid passing a certain low and high temperature threshold. A study that explored the impact of printing at higher than threshold temperatures found that the compression applied from subsequent layers will warp or even deform the print (Meraz Trejo et al., 2020). An attempt made to counter this effect is to have the extrusion stop until the average temperature of the layer drops to more stable temperature (Borish et al., 2019). On the other hand, if the temperature drops too much from the transitioning glass temperature the layers will not adhere to each other. To counter this effect other studies have opted to use infrared lamps to preheat the top layer of a print to induce better adhesion (Kishore et al., 2017; Nycz et al., 2020).

2.2. Large-scale 3D Printing Material Characterization

Material characterization through mechanical properties in large-scale MEX includes a multitude of different test processes including tension, compression, and impact resistance and

variations of these. This section looks at past work that has done mechanical testing for large-scale 3D printed neat and composite polymers.

Hill et al., reported twelve different materials that were tested for tensile mechanical properties; the geometry of the samples was taken from ASTM D638 standard type 3 (dog bone-shaped tensile specimen) (ASTM, 2022) and scaled it up to 2× the size of the dimension in the standard and reduced some of the gripping area (overall length of the specimen) attempting to add more bead paths to the gauge area. Additionally, the low resolution surfaces of the print were eliminated by machining to get smooth surfaces (Hill et al., 2018). Kumar et al., tested for tensile, flexural and, izod impact properties. All these test were based on already existing standards related to composite materials (ASTM, 2017a, 2017b, 2018a). In the same article it was attempted to characterize large-scale prints that were then used as preforms and compressed molded to shape to then be compared with large scale printed parts and traditionally manufactured compressed molded composites (Kumar et al., 2021). Kishore et al., tested for individual inter-layer strength and energy release of the crack initiation using the double cantilever mode-I testing (Kishore et al., 2017). It is also important to note that Kishore et al., work did not have to use a modified beam theory for calculation given that it only looks at crack initiation and not crack propagation which is point of study in this thesis. Meraz Trejo et al., did some compression testing on large-scale printed parts under different temperatures in an effort to get an optimal range around the glass transition temperature of the print and to understand how temperature impacted the quality of said prints (Meraz Trejo et al., 2020). Schnittker et al, performed tensile testing on a similar size doge bone to that of Hill et al, based also on the D638 ASTM standard, with a novel approach of using digital image correlation, DIC, technique to track strain in the specimen (Schnittker et al., 2019). Spreeman et al., tested mechanical properties of modified polymers (PA/ABS) with a poly

(styrene-maleic anhydride) compatibilizer with the intention of improving layer interface adhesion, testing both large-scale and small-scale MEX. The tests done were 4-point bending and Charpy impact testing according to modified version of standard D790 and D6110 (ASTM, 2018b, 2017b; Spreeman et al., 2019).

Characterizing mechanical properties of is not something new in large-scale 3D printing. Different reasons were looked at for develop testing processes, some developed strategies to find the effect of, when compared to their own work, a modified printing process and parameters on the mechanical properties while others focused on developing a precedent in mechanical testing for standardization and recognition of testing techniques that could be used in future characterization of large-scale MEX.

2.3. DOUBLE CANTILEVER BEAM TESTING

The double cantilever beam testing (DCB) is a test that was used first in large scale additive manufacturing to evaluate the improvements done from preheating the layers with IR lamps on fracture energy. The studies where this has been done do not mention which standard they are

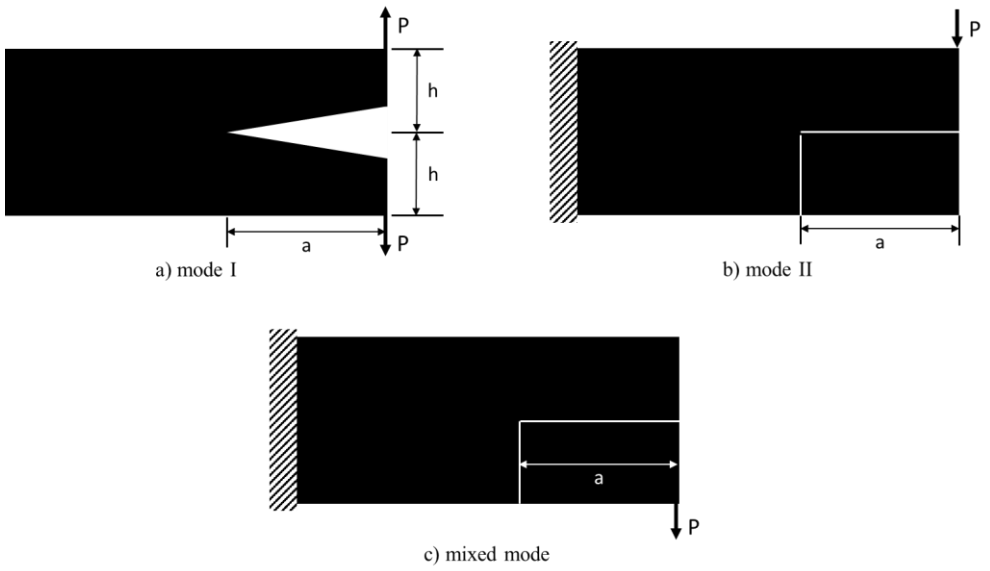

Figure 3 The DCB test a) mode-I, b) mode-II, and c) mixed mode.

based on (Kishore et al., 2017; Nycz et al., 2020). Upon further investigation it was found that a specimen description that is most like the samples used in the previously mentioned articles is that of ASTM standard D5528 (ASTM, 2021a).The DCB testing consist of applying the load in an opening manner by applying symmetrical tensile loads; this is called mode-I which is shown in Figure 3 The DCB test a) mode-I, b) mode-II, and c) mixed mode.a.

There are other test configurations, as seen in Figure 3 The DCB test a) mode-I, b) mode-II, and c) mixed mode., which will not be explained here. The DCB testing in the ASTM D5528 is designed to evaluate the Mode-I opening interlaminar fracture toughness of unidirectional fiber-reinforced material. Although the description in the scope says that the fibers need to be continuous it is only required for the test that the fibers at the interface should be in one directional. This alone does not justify testing for large-scale AM parts. The description accounts for different composite materials which is talked about in the interferences section. Fracture toughness is not a critical material property when it comes to designing 3D printed parts compared to other properties like strength or Poisson's ratio of a material. The lack of literature for fracture toughness in AM parts is attributed to this fact. This paper attempts to explore fracture toughness to further expand the capabilities and expose potential applications of large-scale 3D printer parts.

A case study with a modernized approach of this has proven that using data processing tools, such as MATLAB, outputs results faster and easier while also reducing potential errors from sample fabrication or measurement of crack length (Caltagirone et al., 2020). In addition, the number of data points has increased. This resulted in a much higher resolution of approximately 550% increase. These results justify the modernization of data processing compared to that indicated in traditional standards.

In other fracture studies it is shown that there are different types of crack growth behavior that are dependent on deflection speed, temperature, and material modifications (Kinloch et al., 1983). These types are listed as type A-ductile stable crack growth, type B- brittle unstable crack growth, and type C- brittle stable crack growth. The brittle stable curve is described to have the load rise linearly until it reaches critical value where the crack propagation starts. Brittle fracture can be seen in Figure 4 Load versus deflection curves of a) brittle stable, b) transitioning brittle stable to unstable, c) brittle unstable, d) transitioning ductile stable to brittle unstable, and e) ductile stable.a where the behavior is tagged as type C. Brittle unstable begins similar to its stable counterpart; it has a linear portion until it reaches its critical value then has a sudden drop where the crack is propagating until the stored elastic energy stops the crack propagation, this event is called arrest. When arrest happens a slight rise in load is seen and then another unstable drop happens; this will repeat in brittle unstable crack propagation until the specimen fully breaks. This fracture type can be seen in Figure 4 Load versus deflection curves of a) brittle stable, b) transitioning brittle stable to unstable, c) brittle unstable, d) transitioning ductile stable to brittle unstable, and e) ductile stable.c and it's called type B. The third type of crack is ductile stable crack propagation and although it has a linear region, like its brittle counters, this region stops distinctively at around 0.8 of the max loads, for the material studied in the referenced work. Crack then initiates and slows in a stable propagation that is dependent on the displacement rate. This can be seen in Figure 4 Load versus deflection curves of a) brittle stable, b) transitioning brittle stable to unstable, c) brittle unstable, d) transitioning ductile stable to brittle unstable, and e) ductile stable.e tagged as type A. There are transitional regions, from one type to the other where it usually

starts as either Type A or C and then transforms into type B. The tags for these combinations are appropriately named A→B and C→B and the shapes of their respective load vs deflection curves are simply combinations of the previously described types, as seen in Figure 4 Load versus deflection curves of a) brittle stable, b) transitioning brittle stable to unstable, c) brittle unstable, d) transitioning ductile stable to brittle unstable, and e) ductile stable.b and d.

The process for double cantilever testing requires load and displacement measurement tools to simultaneously measure opening displacement and force applied. Posteriorly, load and displacement are then correlated with the crack propagation at different points along the length of the sample. The output is the energy release rate of the fracture or as mentioned before, fracture toughness, G_{Ic}. There are three data reduction methods for calculating G_{IC} values that are referred to in ASTM D5528 standard (ASTM, 2021a). These methods are modified beam theory (MBT), a compliance calibration (CC), and a modified compliance calibration (MCC). During evaluation of

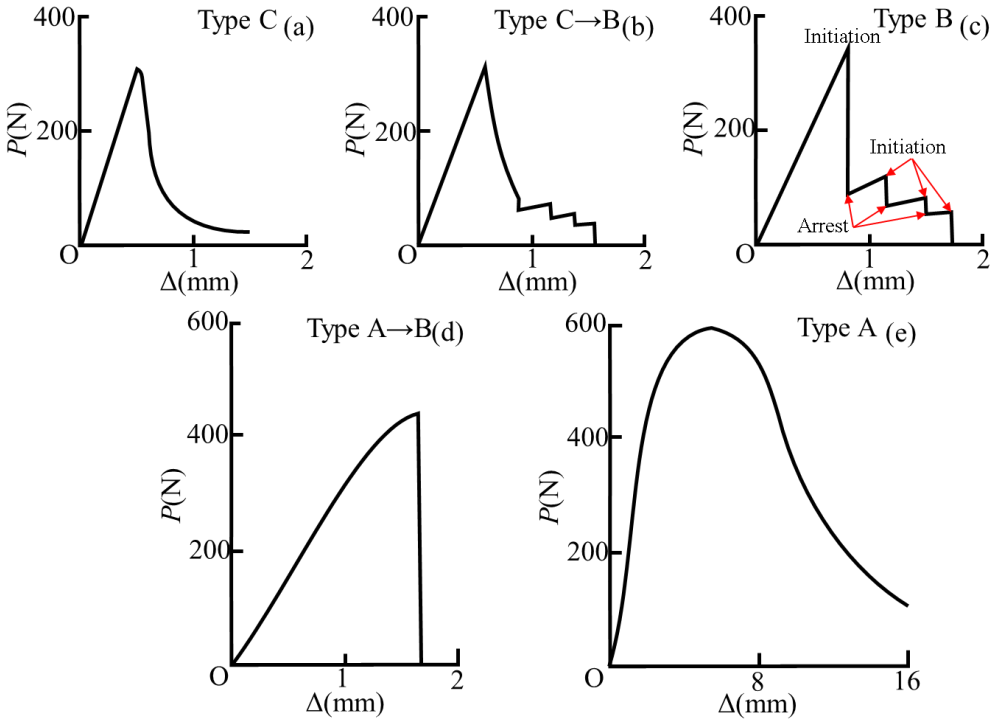

Figure 4 Load versus deflection curves of a) brittle stable, b) transitioning brittle stable to unstable, c) brittle unstable, d) transitioning ductile stable to brittle unstable, and e) ductile stable.

data reduction methods, it was found that the differences between the results did not differ beyond 3.1% which was determined to be negligible difference hence the decision to include them in the standard. Beam theory is used to express the energy release rate of static parallel beams, that is, beams that do not rotate as the load is applied. This does not consider the rotation, which is a factual occurrence in the test's performance and overestimates G_I. That is why MBT is expressed as

$$G_I = \frac{3P\delta}{2b(a + |\Delta|)} \tag{1}$$

where P is load, δ is opening displacement, b is the interlayer width, and a is the crack propagation length. The way this modification works is that it assumes that the crack propagation is slightly longer, $a + |\Delta|$, where Δ is determined experimentally by using the least squares plot of the cube root for compliance, $C^{1/3}$. The compliance, C, is the ratio of the opening displacement to the applied load, δ/P. The MBT is the method with more conservative results compared with CC and MCC. A visual representation of MCC can be seen in Figure 5 Example Plots for a) modified beam theory, b) compliance calibration, and c) modified compliance calibration.a. Compliance calibration is the analytical answer to the experimental compliance calibration, and it is expressed as:

$$G_I = \frac{nP\delta}{2ba} \tag{2}$$

The CC method generates a least squares plot of log (δ/P) versus log(a). After the line is drawn via best least-square fit calculate the exponent 'n' from the slope of this line as described in Figure 5b. It is important to mention that all these data points to calculate G_{Ic} are taken after the crack is visible.

The modified beam theory (MCC) generates a least squares plot of the delamination length normalized by specimen height Figure 7 DCB geometry measurements.*a/h* (see h in Figure 3a), as a function of the cube root of compliance, $C^{1/3}$. The slope of the line is A_1 (see Figure 5c), where the expression for G_{IC} is represented as:

$$G_I = \frac{3P^2C^{2/3}}{2A_1bh} \tag{3}$$

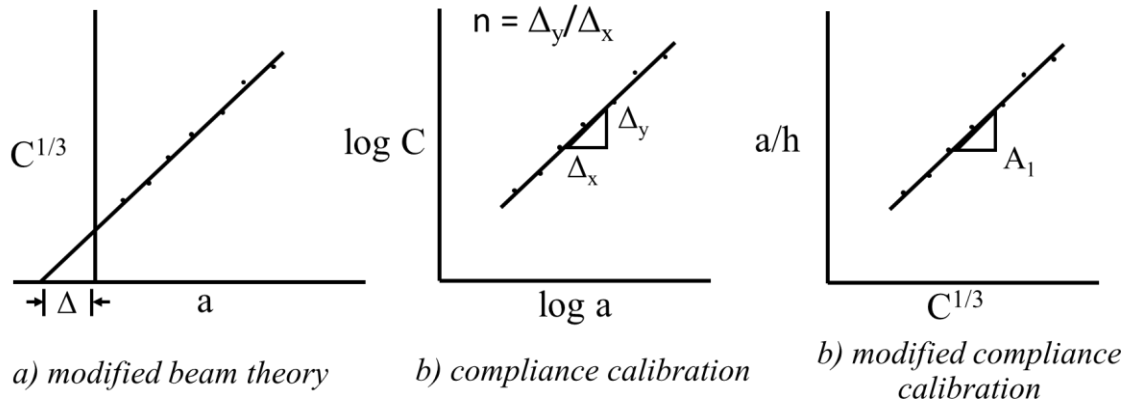

Figure 5 Example Plots for a) modified beam theory, b) compliance calibration, and c) modified compliance calibration.

2.4. FIGURE 7 DCB GEOMETRY MEASUREMENTS.FRACTURE TOUGHNESS G_{IC}

The strain-energy-release-rate, G, is defined as the energy required to extend a pre-existing crack and infinitesimal unit area. Large-scale parts have the condition where the crack extends along the layer interface plane, with negligible contraction on the bead width direction of the beam, the symbol for fracture toughness in terms of strain energy release rate is G_{IC}. Calculations mentioned in the standard (ASTM, 2021a) are derived specifically to calculate towards geometrical features that fall within certain ratios or have minimum requirements. These calculations adhere to traditionally manufactured plastic composites, specifically laminates, which

are thin in nature. These features are the height, *h*, of which identity a/h must be 10 or above, refer to Figure 3a, and the width, *b*, of the specimen which must nominally be between 20 to 25 mm in length. Although the width is not a critical feature (ASTM, 2021a; Davies and Benzeggagh, 1989) the height of the specimen, in contrast, can yield high error percentages if not properly addressed. For the particular case of this work, the height can be made smaller and the length of the specimen and pre-crack longer to adhere to the standard's requirements, but also for this work it has proved unpractical to do these changes for reasons mentioned in '3.1 Specimen Fabrication' subsection. This section of the literature review focuses on calculation for fracture toughness that better adhere to large-scale AM manufactured specimens.

It is well known that there are multiple ways for calculating G_{IC} (Davies and Benzeggagh, 1989) many of these are specific for calculating G_{IC} in laminates. After reading previous work it was found that fracture toughness tests have been done to characterize adhesives using the double cantilever method. The geometry used to calculate fracture toughness is like that of AM specimens

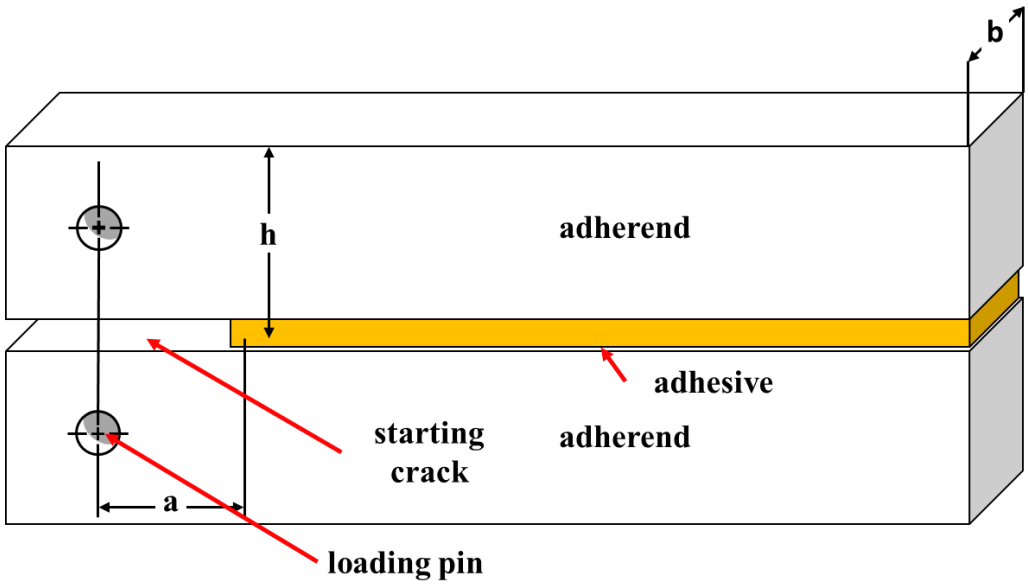

Figure 6 Specimen used to calculate fracture toughness of adhesive joints.

in this work, as seen in Figure 6. The change in energy as crack propagates happens due to displacement which changes the stress-plane area. The conservation of energy, due to this change in area, can be expressed as (Nestor Perez, 2004)

$$\frac{dU_1}{dA} - \frac{dU_2}{dA} = \frac{dU_3}{dA} + \frac{dU_4}{dA} \tag{4}$$

where U_1 is the input energy (loading), U_2 is the energy dissipated as heat during the plastic flow, U_3 is the total potential energy (stored energy), U_4 is the kinetic energy in the system, and dA is the change in fracture area for a constant width, b, and a variable crack length, a. In DCB testing, dU_2 is an isothermal case in which the change of energy transfers across the specimen's contour. For a growing crack, dU_2/dA is the energy dissipated as the fracture crack area changes and what is also referred to as fracture resistance. Given that the nature of the DCB testing is quasistatic, the change in kinetic energy becomes negligible thus making $U_4 = 0$. Combining all these identities we get the definition for energy release rate, G_I.

$$G_I = \frac{dU_1}{bda} - \frac{dU_3}{bda} \tag{5}$$

The input change in energy with respect to crack propagation that is the subject of an external load, P, that causes the crack to propagate where the load points undergo a relative displacement, $d\delta$, perpendicular to the stress plane, and extension of the crack length an amount, da, which is expressed as:

$$\frac{dU_1}{da} = P\frac{d\delta}{da} \tag{6}$$

For mode-I loading, the stored energy to determine G_I for a pre-cracked length, a, and load., P, where crack will start to propagate, is expressed as:

$$U_3 = \frac{P\delta}{2}$$

From a P-δ line, a reciprocal slope defined as the compliance of the specimen's characteristic of the crack length is expressed as:

$$C = \frac{\delta}{P}$$

Combining that last two expressions we obtain the stored energy to be:

$$U_3 = \frac{P^2 C}{2}$$

If we derive the last expression with respect to the change in crack for stored energy (Nestor Perez, 2004):

$$\frac{dU_3}{da} = \frac{P}{2}\frac{d\delta}{da} + \frac{\delta}{2}\frac{dP}{da} \tag{7}$$

After this, by substituting expressions 5 and 6 into 4 and assuming that the crack extends infinitesimally at a constant load, the expression for the energy lost to the growing crack per unit area for a crack of unit width, b, is (Ripling et al., 1971):

$$G_{IC} = \frac{dU_1}{bda} - \frac{dU_3}{bda} = \frac{P_c^2}{2b}\left(\frac{\partial C}{\partial a}\right)_p \tag{8}$$

After solving for G_{IC} there still needs to be a way to solve for partial derivative of the compliance with respect to crack length $\partial C/\partial a$. In the previous expression's compliance, C, is the ratio of the displacement to load, which can also be expressed in accordance with the strength of materials as (Mostovoy et al., 1967):

$$C = \frac{24}{Eb}\int_0^a \frac{a^2}{h^3}da + \frac{6(1+v)}{Eb}\int_0^a \frac{1}{h}da \tag{9}$$

Where E is the Young's modulus and v is the Poisson's ratio. The two terms on the right side of the equation are contributions to the compliance from bending and shear deflections, respectively.

After taking Poisson's ratio, *v*, equal to 1/3 and deriving the compliance with respect to the crack length the equation changes to

$$\frac{dC}{da} = \frac{8}{Eb}\left[\frac{3a^2}{h^3} + \frac{1}{h}\right] \tag{10}$$

implying that the *dC/da* depends only on the height of the beam and the equation hold independently of the specimen shape, to the extent that the beam theory is applicable (Mostovoy et al., 1967). In previous experimentation, compliance calibrations showed that the actual specimen deflected more under a given load than the cantilever formula predicted. This has been found out to be additional displacement of some rotation of the beam's 'built-in' end Sources dictate that an extra length denoted a_0 can simply be added to the beam crack length as seen in expression 11. This extra length is not to be confused with A_0 which in some sources is the pre-cracked (notch) length.

$$G_{IC} = \frac{4P_c^2}{Eb^2h^3}[3(a + a_0)^2 + h^2] \tag{11}$$

Chapter 3: Double Cantilever Beam Mechanical Testing

3.1. Specimen Fabrication

The material used in this investigation was Electrafil® ABS 1501 3DP (Techmer PM, Wichita, Kansas, USA), which was 20 wt.% carbon filled ABS. Prior to printing, the material was dried for 4 hours at a temperature of 90° C. The heated zoned, as described in Figure 2 Extruder heated zones and hopper system, were set to 190, 205, 245, and 245 °C for barrel 1-4, respectively, and 250 °C for both tips. The build, of where the samples were harvested, was a single wall hexagon with a 304.8 mm wall length and a height of 217.51 mm. The slicing was done using the ORNL Slicer 2 (Oak Ridge National Labs, Oak Ridge, Tennessee, USA) with a layer height of 3.5 mm. The slicer outputs a G-code that appears to have a fixed layer timer, causing it to have a different extrusion speed (screw's RPM) than the intended. By trial and error this was corrected and given an extrusion speed of 60 RPM, outputting an average bead width path of 14.7 mm.

The DCB samples were then harvested by cutting the hexagon into panels with a hacksaw and horizontal band saw to then cut individual specimens via water-jet. This decision was made given that water-jet cuts are not as thermally invasive compared to machining (milling). The specimen geometry measurements can be seen in the diagram in Figure 7 DCB geometry

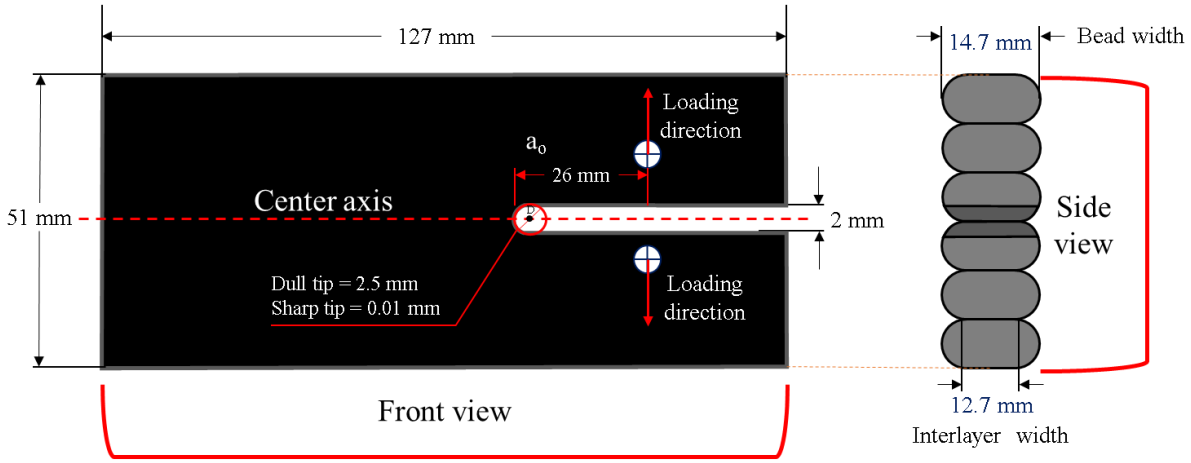

Figure 7 DCB geometry measurements.

measurements.. It is important to note that the most critical geometry features, to the calculations and crack propagation, respectively, are a_o which denotes the distance between the point where the load is applied and the tip of the pre-crack (crack initiation notch), symmetry of the specimen along the fracture plane, and the interlayer width, not to be confused with bead width (see Figure 7). The justification for having these measurements are as follows: the specimens' height, *h*, although required to be made thinner, in accordance with standard D5528, is not feasible given that the bending strength, according to TechmerPM's material data sheet, are inferior to the loads required for the material's pre-crack to propagate making this material composite have a minimum height requirement. Another fix to this would be to make the length of the pre-crack and the specimen longer, which for practical reasons is not feasible given that it would make the specimen at least 609.6 mm long which is well beyond the standards recommendations.

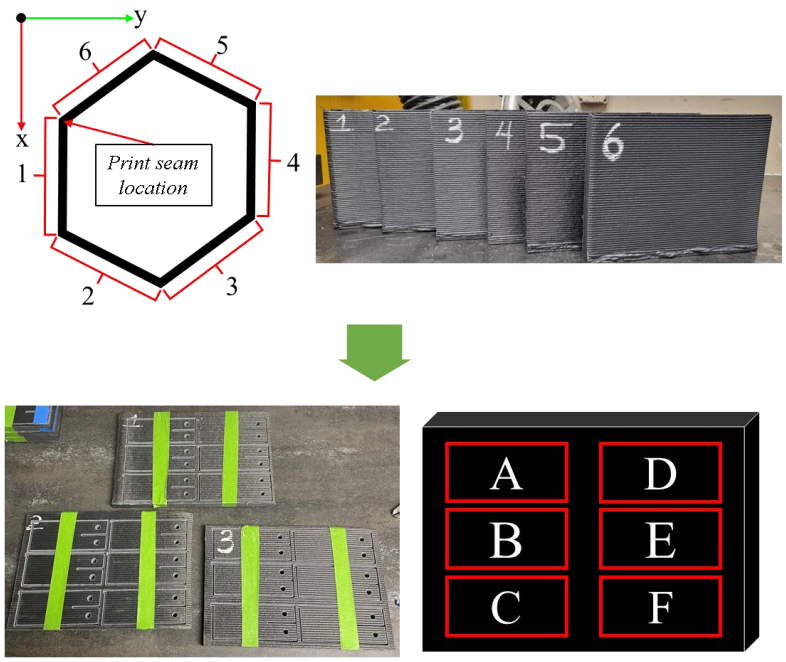

Figure 8 Double Cantilever sample nomenclature diagram.

After fabrication, specimens were then tagged according to the location (wall number) and panel position (lettered position). Each panel was numbered according to the order they were printed following the print path from 1 to 6. From each panel, six specimens were harvested then assigned a letter ranging from ‘A’ to ‘F’ in accordance with their position within the panel as shown in Figure 8 Double Cantilever sample nomenclature diagram..

For the sample preparation the testing standards indicated to store and test at the standard laboratory atmosphere of 23 °C ± 3 °C and 50 ± 10% relative humidity. To help with the conditioning the test standard referenced the ASTM standard D618 which goes into detail of conditioning procedure indicating to follow instruction of procedure C.

3.2. DCB TESTING PROCEDURE

The testing was done in an Instron 5866 with a 10 kN 2525 series load cell using the Bluehill2 software to record load and crosshead displacement (Instron, Norwood, Massachusetts, USA). In addition to getting the load and displacement curves, the specimen was video recorded as the load was being applied, using a Canon EOS 80D camera and a Canon EF 100mm f/2.8L Macro IS USM lens CA (Canon, Melville, New York, USA). The video recording was then used to correlate data points of the load/displacement curve with the specimen’s specific crack lengths. This information was subsequently used to calculate fracture toughness. Prior to testing, the specimens were measured for interlayer width, as seen in Figure 7 DCB geometry measurements.. Posteriorly, the specimens were coated with white corrector fluid and subsequently marked for calibration using a custom-made stencil, as shown in Figure 9a) Specimen coating and marking example b) Image processing capture requirements.. Before testing, grease was applied onto the fixtures loading pin holes to reduce the impact of friction from the pins during loading.

For crack propagation detection it was traditionally recommended (according to ASTM D5528 standard) to use a microscope or any other observation tool that can help visually detect, with a precision of ±0.5 mm or less, the crack length and then record these measurements to then use in calculations. This method collected eighteen points per sample and heavily relied on human observation and intervention in the recording. For this study, as load is applied a video of the specimen is recorded that would be used to then extract specific frames to measure the crack length propagation, another camera was used in tandem that faced Bluehill2 software interface screen using OBS studios, setup shown in Figure 10. This was made so, to synchronize the video with the load/displacement captured from the testing rig. The camera was placed perpendicular to the specimen crack propagation surface. The recording of the specimen required calibration dots, as seen in Figure 9a) Specimen coating and marking example b) Image processing capture requirements., that were used during image processing to calibrate the distance in relation to the pixels in the frame - this was called pixel ratio. These dots conformed two rows parallel to the direction of the crack that sit top and bottom from where the crack will happen. Each row had eleven dots and the distance between adjacent dots in a row is nominally 5 mm, note that the stencil used to mark the dots was 3D printed via vat photopolymerization and the difference between the intended geometry and the resultant part were considered for calibration. The dots can describe information of the surrounding area of where the crack will be seen and assess if there is distortion or rotation in the image, this in addition to averaging the distance between adjacent dots to get a consistent pixel ratio. The image processing and data reduction calculation were done using MATLAB software where the script extracted the exact number of frames needed depending on the size of data points outputted from the load/deflection curve taken from the testing rig. This technique allowed to use hundreds of points in the crack length rather than the traditional 18, giving

not only higher resolutions but also more conservative results being that it recorded the length of the crack at specific load/deflection points rather than relying on eyesight and human interaction

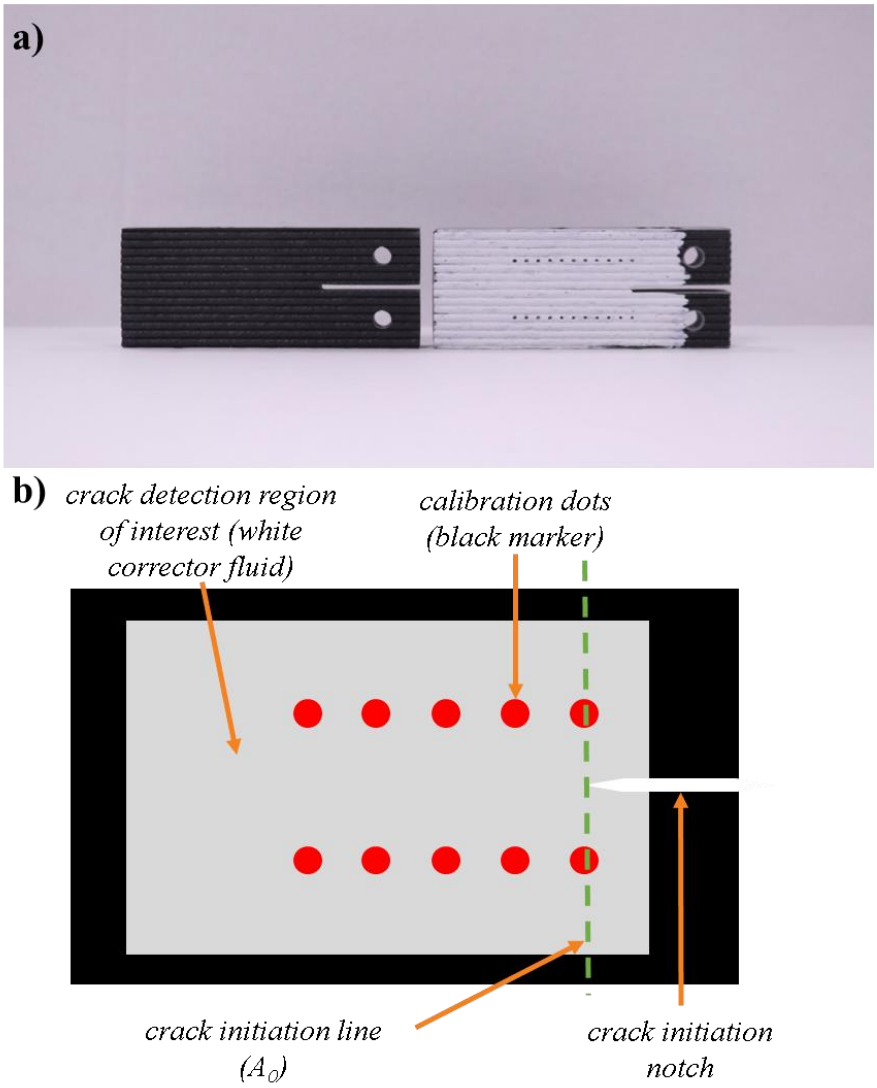

Figure 9a) Specimen coating and marking example b) Image processing capture requirements.

to record the location of the tip of the crack with respect to the markings done in the traditional testing process.

The standard, ASTM D5528, required the specimen to be loaded at least two times to compensate for the traditional specimen preparation. The notched edge is fabricated by adding a

film at the interlayer face to interrupt fusion between layers. This creates a matrix-rich region which is not expected to be seen in this work's specimens. This work includes a first round of tests that observe this event (4.1 Exploratory work). Six specimens were tested at deflection speeds of 1, 3, and 5 mm/min with and without the pre-loading. For traditionally manufactured specimens some sources mention the use of a small knife to sharpen the crack tip. Although this is not recommended for laminates, it has been found that for specimens where the pre-crack is machined or water-jetted it is encouraged to sharpen the crack tip. The reason being that the stress concentration in a crack is dependent on the geometry of the same crack. In this work the specimens have a radius on the tip of the crack; if the radius is not small enough the stress will distribute along said radius. This in turn captures structural properties instead of material properties. By making the radius smaller the crack tip stress concentration goes higher acting as a microfracture allowing to capture the material properties. A second round of tests was done where tungsten carbide box cutter blades (DeWalt, Towson, Maryland, USA) were used to create a small incision to induce high stress concentration at the crack tip. The results were compared with the first exploratory round to prove that this method should be a requirement of testing for fracture toughness in large-scale additive manufacturing.

3.3. DATA PROCESSING & CALCULATIONS

For data processing MATLAB software was used to extract and process frames and correlate them to the load/displacement data recorded from the test. The workflow for the MATLAB script (see appendix A3 Data Processing MATLAB Code) consisted of four sections: frame and data extraction, image calibration, crack propagation measuring, and fracture toughness calculations. In the continuing subsections, frame extraction, calibration and crack propagation will be grouped together to explain innovations done in the data processing of this modern

technique of data capturing for DCB mode-I testing. The full text for the MATLAB script can be seen in appendix A3.

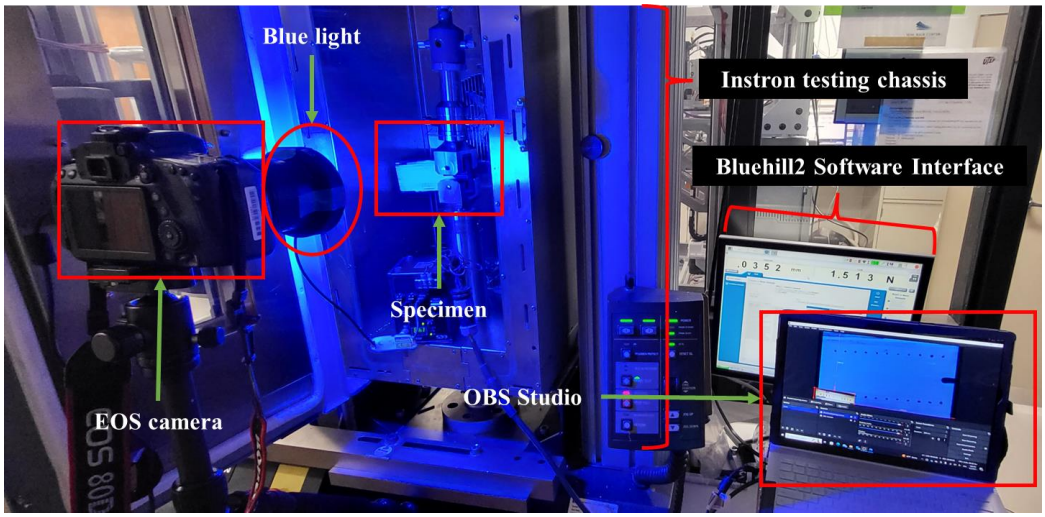

Figure 10 DCB testing video recording setup.

3.3.1. Data processing

As explained in the DCB procedure section, the video that monitored crack growth was recorded at 60 frames per second while the testing rig was recording load/displacement data every 0.334 s, this was a deliberate decision being that 0.334 is a multiplier of the number of frames in a second. The number of load/displacements data points recorded then loaded, in data processing software, was then the number of frames to be extracted from the crack propagation. A recording of the Bluehill2 software interface was used to synchronize the video of the specimen to the load and displacement data points. The video duration was then trimmed, using a computer default video editor, from the moment the test starts recording to the point where the test stops. The trimmed video was then placed in the same folder location of the MATLAB script to then load, when the script ran, onto the data processing software. If, for example, three hundred load/deflection data points were recorded then the MATLAB script would read the first frame and

posteriorly read equidistant frames from the whole video collecting three hundred frames in total. This, although complex in contrast to taking pictures at specific time periods, allowed for easier synchronization of the load/displacement with the crack propagation length after the testing.

The intention of the calibration section was to size the pixel in terms of millimeters. Instead of using a single gauge length (two dots), two rows of calibration dots on the top and bottom of where the intended crack would appear were drawn (refer to Figure 9a) Specimen coating and marking example b) Image processing capture requirements.Figure 9a) Specimen coating and marking example b) Image processing capture requirements.) then used to find the pixel size ratio. The calibration only requires one frame to measure a pixel size ratio. The frame chosen for calibration was the frame that correlates to the critical load which in script is referred to as the critical frame, since at this point in the testing, rotation from initial loading has reached stability and sits before the start of crack propagation where rotation from crack opening happens. The script then finds circles in the image where the dots are, then measures and records the distances between every adjacent circle center to then average all recorded distances. The intended distance between each adjacent dot is 5 mm, this is then divided by the average pixel distances taken from the average circle outputting a mm/pixel ratio. For each individual setup, the camera placement might have changed; this method allowed some undesired visible tilt of the specimen. This was compensated by creating a linear regression of each row of calibration dots (top and bottom) then using the average slope of both lines to compensate for tilt as the crack length propagated. It is important to mention that the rotation of the specimen when it was being loaded would stabilize within the first few frames. These first few frames can be neglected in the calculation being that the crack distance continues to be initial pre-crack length, A_o, until crack propagation starts.

Additionally the lens used to record video is considered a narrow lens, this makes image distortion from the lens neglectable. The workflow for calibration subsection can be seen in Figure 11.

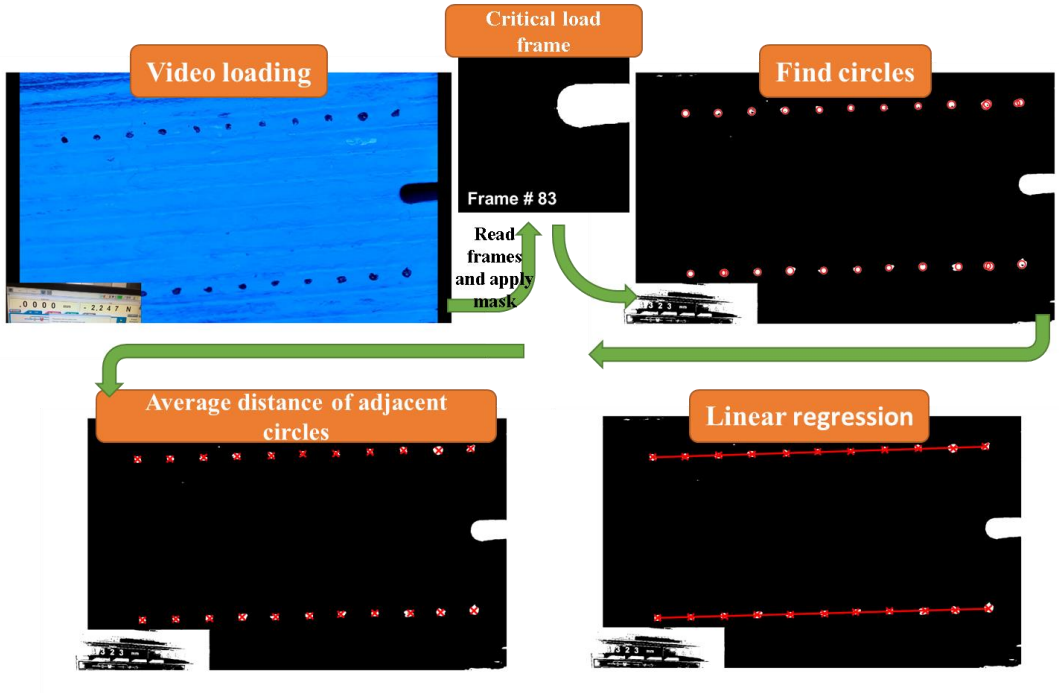

Figure 11 Calibration subsection workflow diagram.

3.3.2. Fracture Toughness Calculations

The fracture toughness calculation subsection of the data processing script includes postprocessing of the load and deflection data collected and the fracture toughness calculation mentioned in the literature review albeit an iteration of that equation (11) (equation (12) in subsection 5.3 Fracture Toughness Calculations) that considers the difference in bead width and layer interface width which was also taken from the referenced work for the formula described in the literature review (Mostovoy et al., 1967).

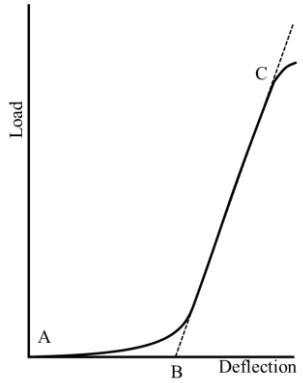

Figure 12 LvD offset correction method.

The plotted load vs deflection curve, LvD, which in the script for this work is called the corrected LvD plot. The load cell was calibrated before mounting the specimen, and when the specimen was mounted it still had a few millimeters in distance to advance before it started to apply load onto the specimen. Apart from this extra deflection, which was not relevant to the testing, the result had a toe which was a progressive loading that in other standards, like ASTM tensile D638, was mentioned to not be representative of the material's behavior. It is also important to note that this type of corrections are not mentioned as part of the DCB standard (ASTM, 2021a). The decision to offset the values where the linear region passes through the origin was to measure the distance where the loading onto the specimen starts rather than considering the region of the deflection where opening is not inflicting a load onto the specimen. As seen in Figure 12, point *A* represents the start of the test and line *BC* represents the regression of the linear region of the LvD plot. In this case *B* would be the new offset length of where the loading of the DCB starts.

Chapter 4: Results & Discussion

4.1. Exploratory work

There are parameters that were under review for testing in two exploratory rounds. The first round attempted to find a difference between the results of pre-loaded and no-pre-load testing using the load/displacement curve. For the second round of exploratory work, a crack tip sharpening technique was used. The theory behind the crack having to need a sharpened crack tip is that a dull tip (round crack tip) would capture behavior with respect to the structure rather than the material.

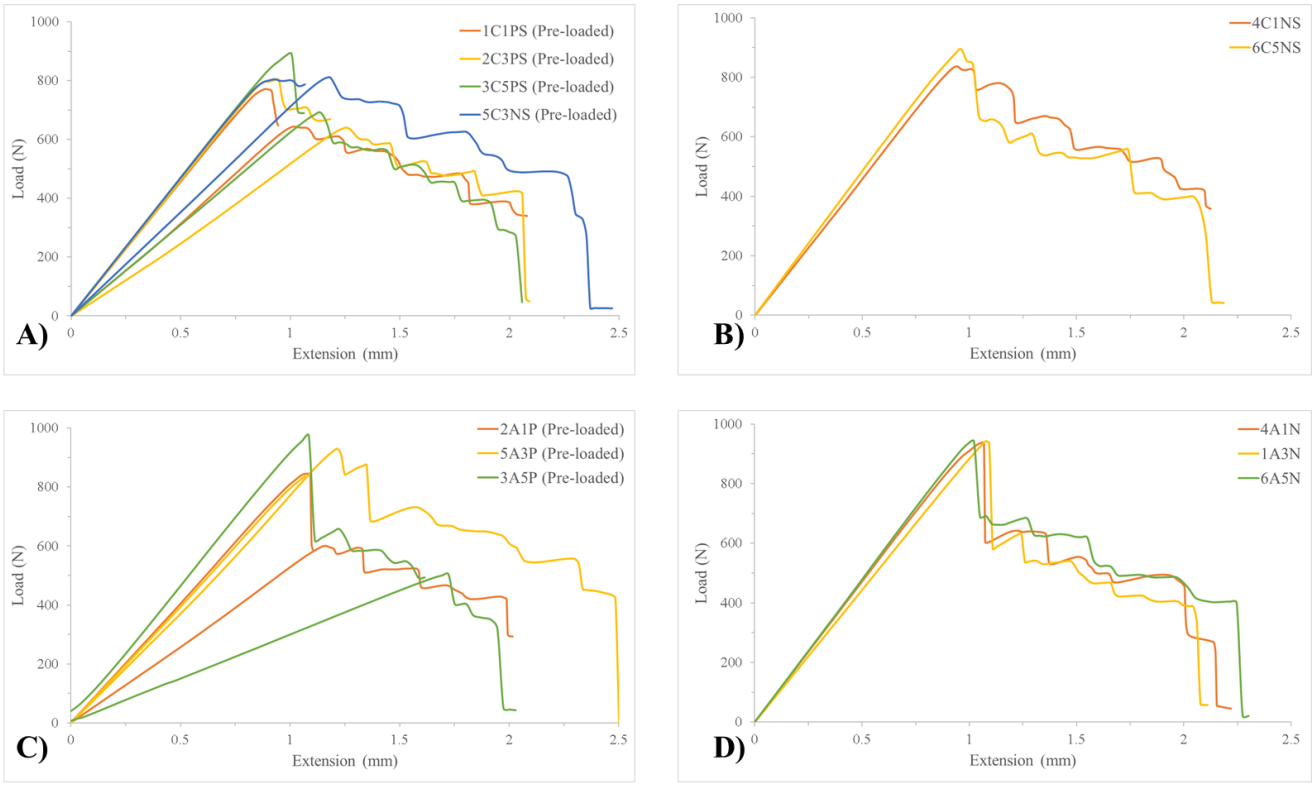

Figure 13 Load vs extension (crosshead deflection) curve of A) pre-loaded samples with crack sharpening, B) no-pre-load samples with crack sharpening, C) pre-loaded samples, and D) no-preload samples.

In the first round of tests (Figure 13 c and d there is a sudden, almost vertical, crack in the beginning of crack right after reaching critical load. This is described as unstable brittle fracture. As explained in the literature review section, this is not an ideal condition for detecting fracture

toughness. In contrast with the sharpened crack tip specimen, the dull pre-crack will take a bigger load (Figure 13A and B); this difference is not a material property but rather a structural one. This is due to the stress concentration being lower at the crack initiation due to the geometry of the pre-crack tip as explained in subsection 3.2 DCB Testing Procedure. It can also be observed that in the pre-loaded tests (Figure 13 a and c) the control of the where the pre-load stopped varied. This was since the test had to be manually stopped given that there was no efficient control, within the testing software, of where to stop the test. Ideally one would stop the test within 3-5 mm of crack propagation and then start the second part of the test. Given that there is virtually no difference between pre-load and no-pre-load it is recommended, for practical reasons, to use the no-preload for testing.

4.2. DCB Testing Results

For the results of DCB testing, each specimen should output a load vs deflection curve, LvD, and an R-plot. The R-plot displays the fracture toughness at all recorded points of the crack propagation length and in later iteration filtered data. The three deflection speed testing parameters were randomized using Minitab and the tests were performed with no pre-load and crack sharpening, given the results of the exploratory work. The fracture toughness calculations were done using the Mostovoy, 1967 et al. calculation, which in this work is referred to as the rigid specimen compliance calibration, RSCC. Calculations were done with all the data points from the critical load to the end of testing. That is, every load and deflection recorded after critical load was used to analyze behavior and recording intricacies. It is fit to explain that not all points are significant for fracture toughness calculations, for this, RSCC was used for a second round of results to calculate with a discrimination criterion where peaks in the data were selected to calculate fracture toughness.

4.2.1. Unfiltered DCB Testing Results

One of the advantages of the DCB mode-I testing is that a single specimen should output multiple G_{IC} values. The R-plot is where all the recorded G_{IC} values of a propagating crack of a single specimen can be seen. As seen in Figure 15, the resolution of data points taken from the Bluehill software depends on the deflection speed, that is the n values. The unfiltered R-plots also display outlier values as seen on Figure 14b, d, and f. A reason why there are high value outliers in the beginning may be because the crack initiation is taking structural properties rather than material properties as explained in the exploratory testing and literature review section, even after crack tip sharpening was done. This is an event that prevailed throughout all the tests and in a few cases, the load increased to a point as if no crack tip sharpening was done. This effect reduces the pool of potential valid fracture toughness results on a case-to-case basis. For the outliers towards the end of the test there are three theories surrounding this event which are not mutually exclusive from each other. A catastrophic fracture happened towards the end of the test which in video was seen as a large and fast crack propagation that tends to go out of frame. This makes the crack measurement lock at a specific length due to the crack tip going out of frame and not recording updated fracture resulting in large G_{IC} values. Immediately after, being that the fracture is catastrophic, the load should dramatically drop at the locked measured crack length resulting in small G_I values. Another theory was that the crack propagates at a much higher rate than the camera itself can capture during catastrophic fracture; this last theory is only speculation given that there is no actual proof of this happening. Given that the test is meant to be stopped at a specific crack

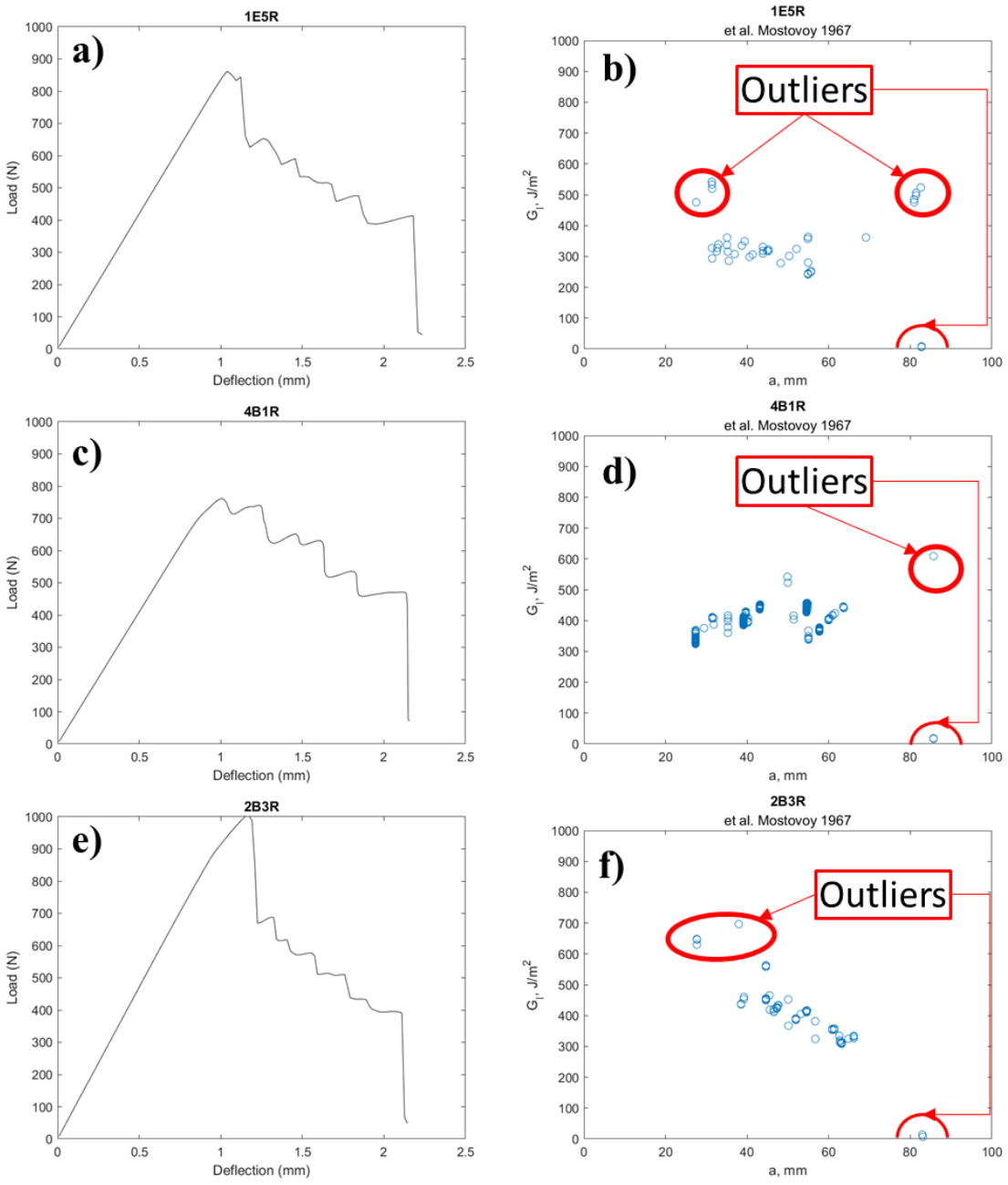

Figure 14 Unfiltered values of a) LvD and b) R-plot of specimen 1E5R, c) LvD and d) R-plot of specimen 4B1R, and e) LvD and f) R-plot of specimen 2B3R.

length this reveals that the test may be stopped at a reduced crack length threshold compared to that indicated by the standard D5528. This catastrophic fracture is consistent at a deflection point of 2 mm or a crack length of around 70 mm, which can be used to draw testing parameter relations

that are dependent on the specimen's length. All the unfiltered testing results can be seen in Appendix A1.

The fracture toughness results were plotted together along with their respective deflection speed groups into box plots (Figure 15). The plot box helped identify outliers in the values of G_{IC}. The way that the threshold is calculated is by calculating quartiles of a data set. The quartiles in question are Q_1 and Q_3 which are the medians of the lower and upper half of the data set numbers. The way that the outlier threshold was calculated is by getting the difference between Q_1 and Q_3, that is the inter-quartile range, IQR. The upper and lower thresholds for outliers are then calculated by the expressions:

$$Lower\ limit = Q_1 - (IQR * 1.5), \text{ and}$$

$$Upper\ limit = Q_3 + (IQR * 1.5)$$

this calculation is the preset and built into excel box plots. However these can be modified if done manually

The whiskers mark the error bars, that is the maximum and minimum values within the lower and upper limits calculated. This is the default calculation given by Microsoft Excel. It should be mentioned that the *x* inside the box marks the mean and the line inside the box marks the median. The line connecting the boxes is the mean line, connecting the mean values from the boxes pointing out differences of the mean G_{IC} values. This was marked to have a visual aid of how the values from the specimens relate to each other. Each specimen has the number of data points used to create the plots. The recording for LvD points was dependent on time and that is why at faster deflection speeds there are less G_{IC} points per specimen. Also the number of outliers is higher in the 5 mm/min rate than the other two data sets; no conclusion of why this happens have been made. It should be taken into consideration that the specimens are not set up in a specific order within the box plots.

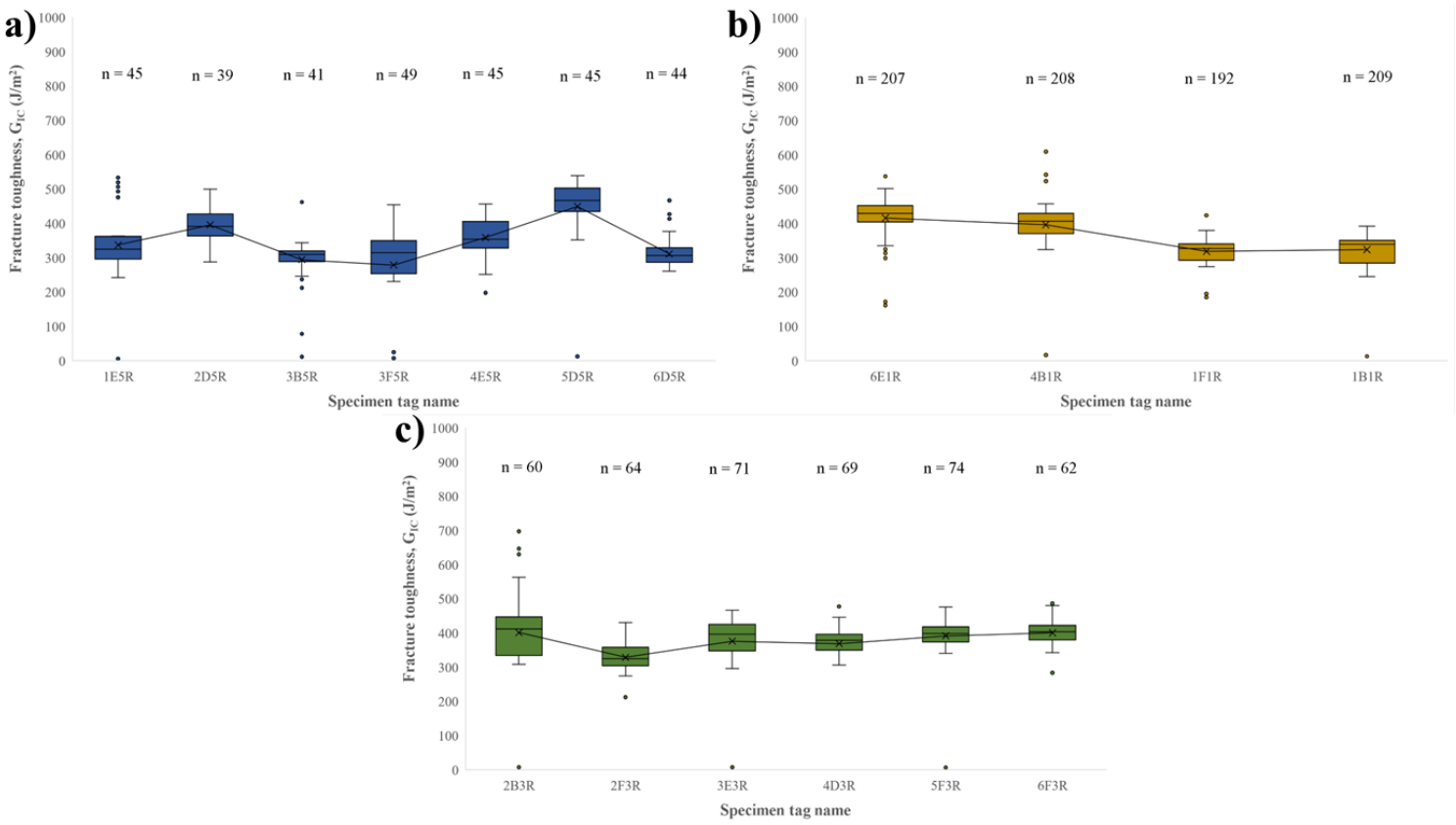

Figure 15 Fracture toughness, G_{IC}, unfiltered values of specimens, using RCBB model, in rate groups of a) 5 mm/min, b) 1 mm/min, and c) 3 mm/min.

4.2.2. Filtered DCB Testing Results

As seen in Figure 15, there are some outliers in the G_{IC} results. Some of the outliers are seen towards the end of the test but for a few specimens these outliers do not appear in this manner. This is explained by the fact that the test had to be stopped at a specific crack length and that there was no developed argument at the time to input into the testing software to stop the tests automatically which meant that the tests had to be stopped manually. Some of these tests were successfully stopped at the required crack length while others suffered catastrophic failure faster than the operator could stop the test. In Figure 16 an example of this is shown where Figure 16b was stopped successfully at the required crack length and Figure 16c where the test had catastrophic failure before reaching the intended crack length. Two things are happening at

catastrophic behavior: the crack extends beyond the frame of the camera fixing the crack length measurement and the specimen experiences extreme rotation due to the sudden release of energy which can also be referred to specimen instability point. For the latter event, even if the crack were still in frame, the measurements would not be accurate due to the extreme rotation and specimen instability which would cause inaccurate fracture toughness calculations.

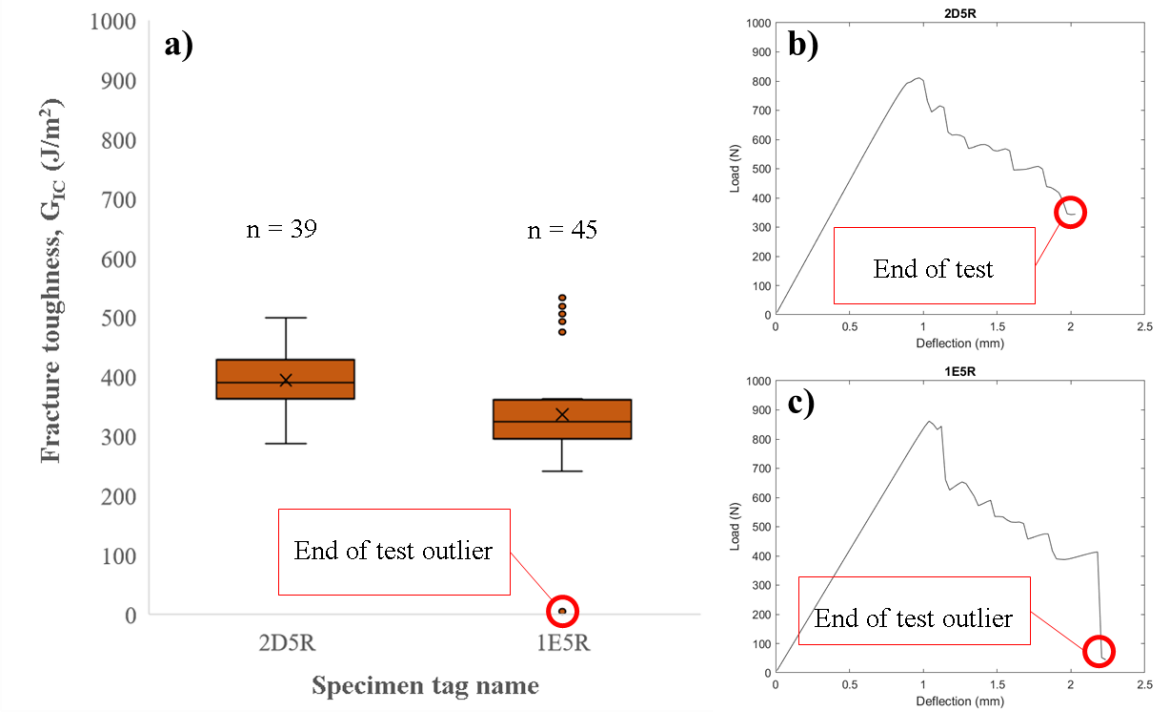

Figure 16 a) Box plot unfiltered values comparison between b) test stopped at the required crack length against c) test stopped after critical failure; both specimens shown were tested at a rate of 5 mm/min.

The other outliers that are seen exist at the beginning of the crack propagation (critical load section of the test). These appear to overestimate fracture toughness and they appear to happen in all specimens to varying degrees and agnostic to the strain rate. This is because the purpose of the crack tip sharpening did not have the intended impact and in some instances, it appeared as if the crack tip was not sharpened at all when comparing them to the critical loads seen in the unsharpened crack tip exploratory work (Figure 13c & d). In Figure 17 the extremes of the varying impact of the crack tip sharpening is shown where Figure 17b has a lower impact than intended

and Figure 17c has an impact more in tune to the desired results. While the loading resumes to normal behavior after the initial crack, this initial crack for these low impact crack tip sharpening does extend a rather large amount, lowering the amount of crack points useful for crack propagation.

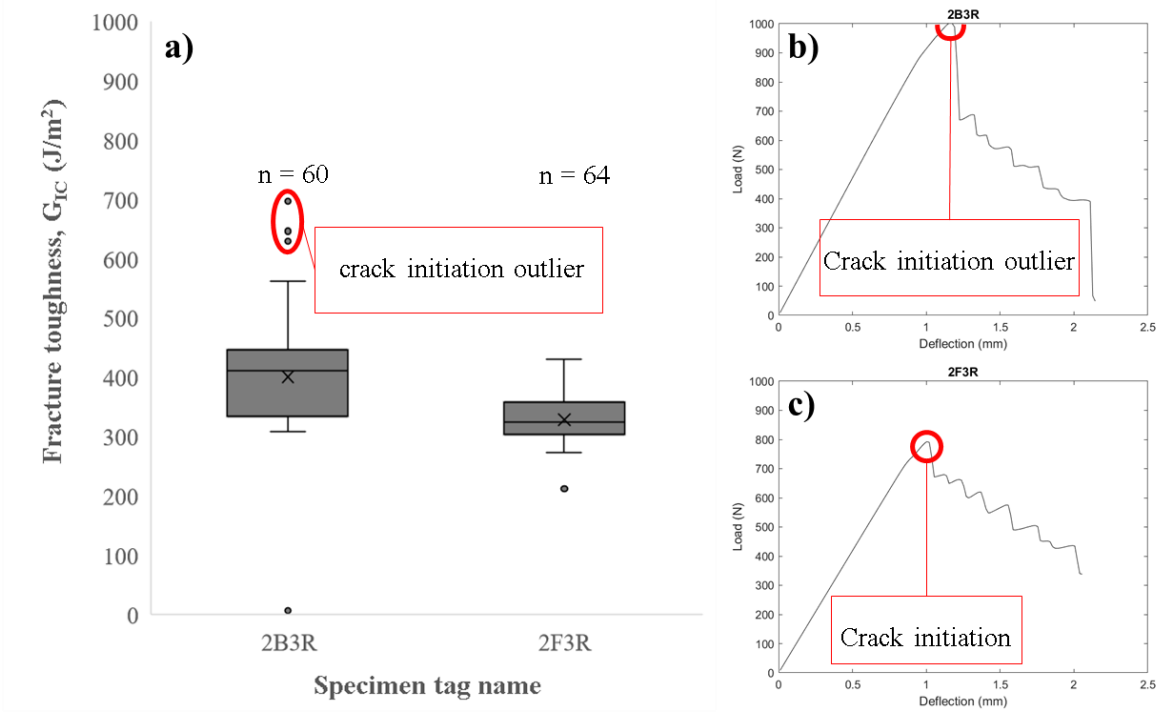

Figure 17 a) Box plot unfiltered values comparison between b) test of low impact crack sharpening against c) high impact crack sharpening; both specimens shown were tested at a rate of 3mm/min.

In addition to the outliers seen at the beginning and end of crack propagation, some data points, as the crack propagates, that are not representative of the material's behavior are those which get close to vertical in a downward trend. The results were filtered by only using peak values in the LvD graph for the fracture toughness calculations. This in turn helped eliminate the outliers seen towards the end of the testing. As for the outliers of the beginning of the test, being that some are also peak values (critical load), any peak value at the critical load deflection length and before this deflection were taken out of the calculations, by indexing the critical point and creating an array that only includes the values after the critical index within the software. As seen in Figure

19a, c, and e, the LvD plots show the peaks that were used to calculate the G_{IC} values for a single specimen as the crack propagates. These plots are paired with their respective R-plots (Figure 19) which used the RSCC fracture toughness calculation method. This method of discrimination was used mainly to take away the outliers from the fracture toughness calculations which were explained in the previous paragraphs. It should be noted that while most of the plots do not use any peak marked at the critical load and any peak before the critical load, there is one exemption, as seen in Figure 19c and d. This exception has 2 peak loads before the critical load, and it was considered to bypass the impact of no crack tip sharpening for which the critical load was considered in the calculation in this isolated case. It is also fit to mention that this failure type, from the non-linearity point (first peak) up to the fourth peak, appears to be ductile fracture

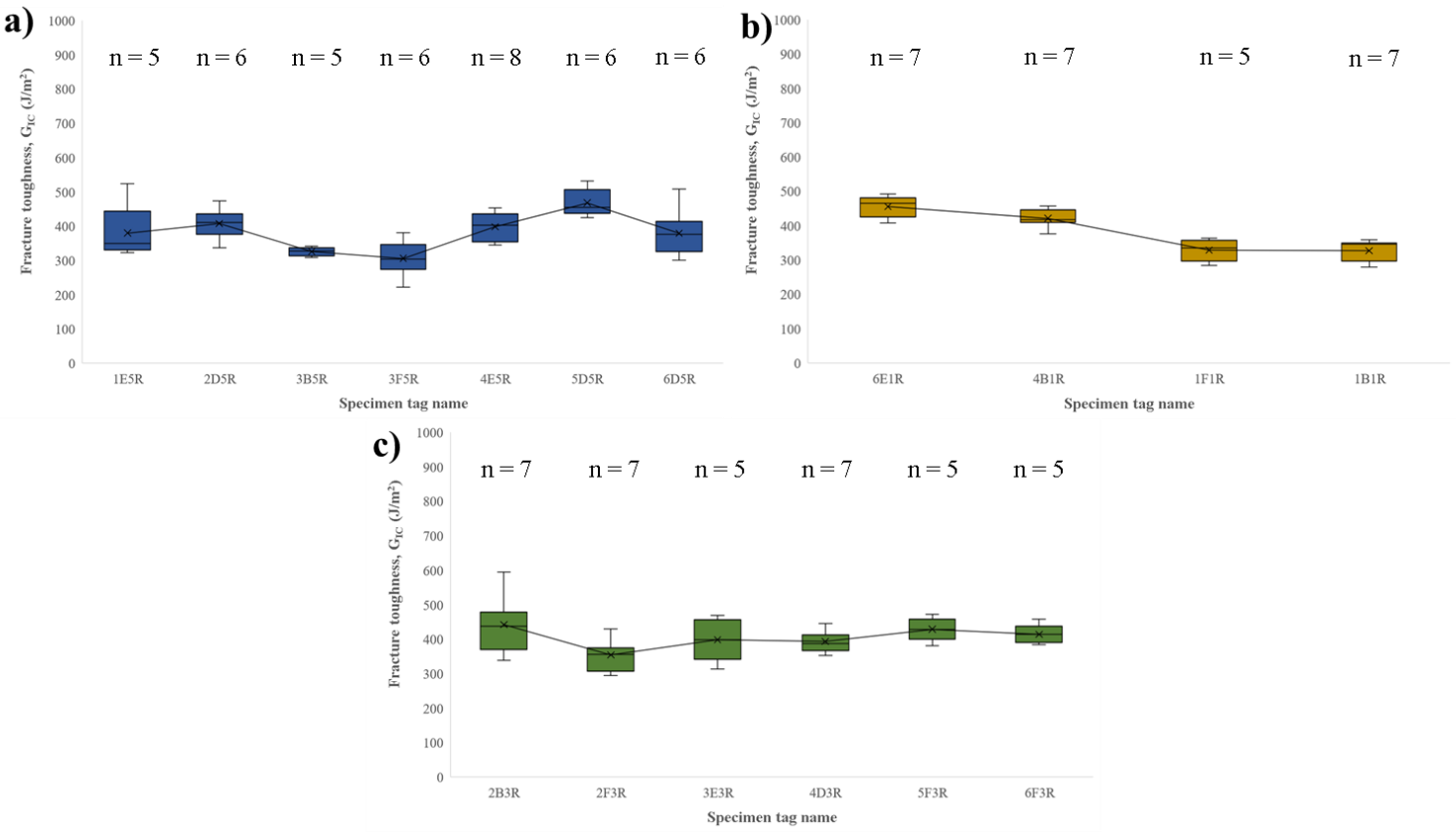

Figure 18 Fracture toughness, GIC, filtered values of specimens, using RSCC model, in rate groups of a) 5 mm/min, b) 1 mm/min, and c) 3 mm/min.

behavior. Specimen 5F3R was the only specimen that had this type of behavior. RSCC results were also grouped together in box plots as before in Figure 18.

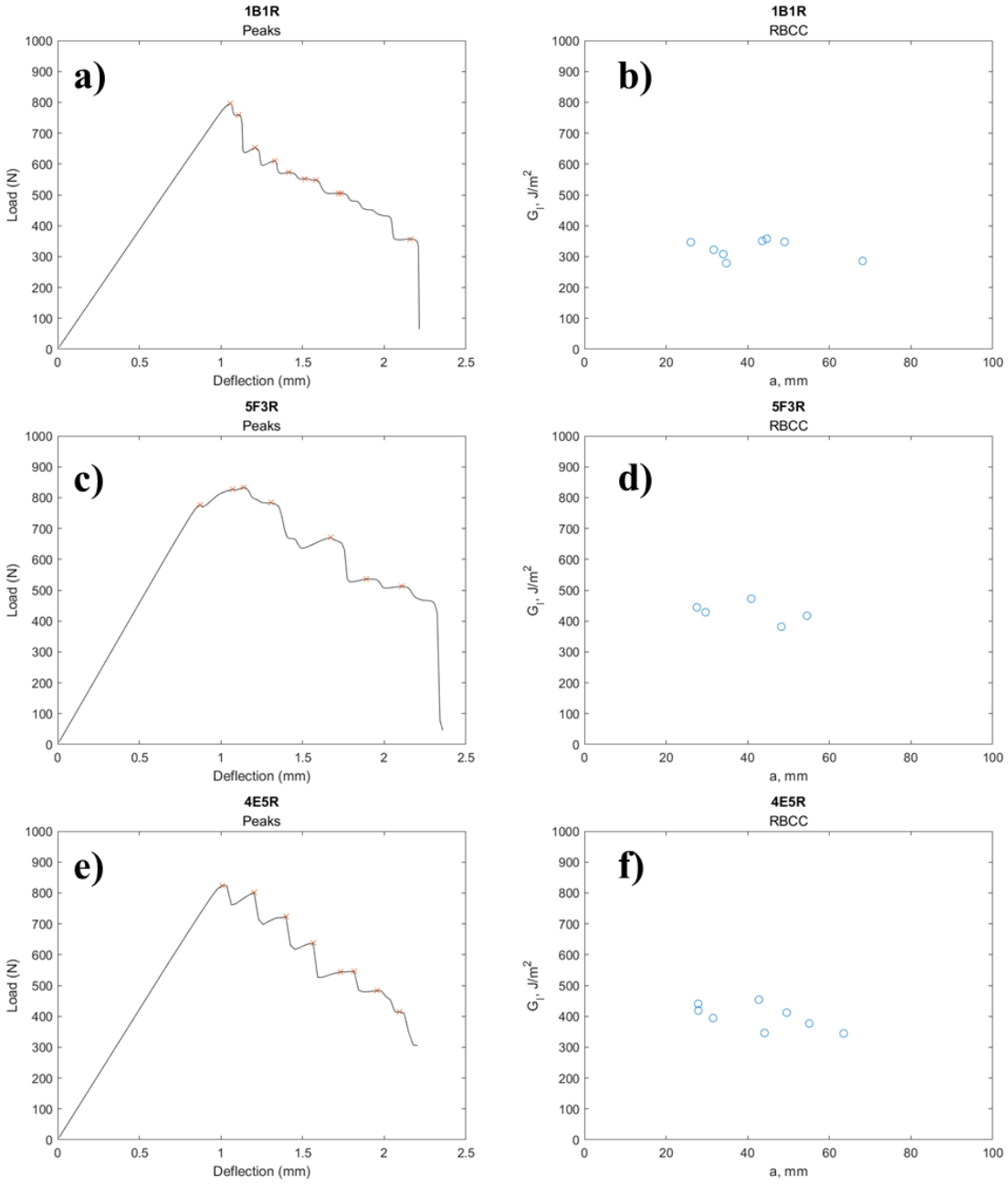

Figure 19 a) R-plot and b) peak values of specimen 1B1R, c) R-curve and d) peak values of specimen 4D3R, and e) R-curve and f) peak values of specimen 4E5R (filtered values).

The average G_{IC} for deflections speeds 1, 3, and 5(mm/min) were 377.89, 401.82, and 370.2 J/m^2 with standard deviations of 65.49, 30.45, and 55.52 respectively. A two- tail hypothesis t-test with the unfiltered values of fracture toughness was done. This compares the statistical significance of fracture toughness means at different deflection speeds. This thesis hypothesized that the mean values would be unequal and deflections speed does indeed have a significant impact in fracture toughness calculations. Hypotheses are represented as

$$H_0: \quad \mu_1 = \mu_2$$

$$H_T: \quad \mu_1 \neq \mu_2$$

where μ_1 is the mean of a rate and μ_2 is the mean of the rate it is being compared to. H_0 is the null hypothesis and H_T is the thesis hypothesis with level of significance, α, of 0.05. For all the comparisons, that is deflection speeds 5/3, 5/1, and 3/1 (mm/min) the t statistic fell inside the non-rejection region, with p-values being 0.2568, 0.8360, and 0.5858, respectively. These p-values are bigger than α which is further evidence that the null hypothesis is non-rejectable. Additionally, a one tail f-test was performed to see if there is a statistical difference variance using a 0.05 level of significance, α. The hypotheses are represented as

$$H_0: \quad \sigma_1 = \sigma_2$$

$$H_T: \quad \sigma_1 \neq \sigma_2$$

where σ_1 is the variance of a rate and σ_2 is the variance of the rate it is being compared to. The H here, as in the comparison before, represents the hypothesis of whether there is a statistical difference in variance. The p-values were 0.1042, 0.3334, and 0.0662 which are all bigger than α making in unable to prove H_T. In conclusion, there is no strong proof that there is a significant difference in the variance or in the mean when calculating fracture toughness.

Chapter 5: Conclusion & Future Work

5.1. DCB Testing Procedure and Specimen Fabrication

The results in the exploratory work show that pre-load against no-pre-load have virtually no difference. Although an argument can be made that the pre-load testing process can be improved with a better control technique or even applying live image processing of the crack propagation to stop the test at the required crack length; it has proven to be more practical to not stop the testing at all. Another of the results prove that sharpening the crack tip does yield better capture of the material property against the non-sharpened crack tip. One of the main differences is that the specimen, without crack tip sharpening, will take larger loads. In this work, approximately a 100 N difference was found which is approximately a 10% increase against the sharpened specimen data capture. For a non-sharpened crack tip specimen, the fracture transitions from an unstable brittle fracture to a stable brittle fracture. This contrasts with sharpened crack tips being that there is no fracture transitioning type and the crack stays as brittle stable fracture throughout. As theorized before, this may be due to the dull crack tip distributing the load along the contour of the specimen, recording the specimens' structure properties rather than the specimens' material properties. Another observation that was made is that if the crack tip sharpening is not effective will impact the results of fracture toughness. In at least one case where crack tip appeared to be untreated there was a downward trend throughout the rest of crack propagation. For fiber bridging, it is known that as the crack propagates fracture toughness increases this was not seen in any of the specimens implying there is no fiber bridging happening surface analysis would be recommended to confirm this. Additionally, further investigation would be recommended given that there may be variations in making this incision (sharpened crack tip) using different tools and techniques.

Given that there was little control over fabrication of the notch alignment with respect to the interlayer plane due to the limitations of waterjet fabrication (ideally these features should be as close as possible to fully parallel). Measurements around these features, including loading pins placement, were taken. A diagram showing the measurements and a table with the values can be seen in Appendix A2. All the testing was randomized, and these measurements were taken to find any correlation or trend that may exist pertaining to these measurements in the future. There is some tilt on specimens when recorded as it reaches its stability frame. This is due to the inconsistencies in fabrication of the specimens, specifically when water-jetted. What happened is that the interlayer is not aligned with notch, and, in consequence, the loading pin holes. This will introduce undesired shear loads that are not being compensated for in the calculations portion. This is mentioned as something that has to be carefully considered.

It is fit to report that the corrector fluid could not dry up fast enough before being tested. This for other types of testing is not considered a problem being that deflection or strain is dependent on markings; for this work it had a great impact on a few of the tests. Being that the corrector was somewhat viscous for a good portion of these tests it became a problem when processing the video being that the crack was not visible even as it propagated an example of this event can be seen in Figure 20. This was solved by drying, with a fan, each specimen right after taking it out of the conditioning chamber. Although this proved to be a good solution, it goes against the conditioning standards. For future reference it is fit to mention hypothesized solutions; that is, use a dry white paint or powder-based primer that would have the same impact of contrasting the values in the specimen and it did not depend on drying up. Another optional solution is to apply the coating before conditioning. The standard calls for drying the material for condition as a second option, this would work in tandem with the corrector fluid as it would dry it

too making it brittle while testing. This high viscosity corrector fluid was seen in 1 of the rate 3 mm/ min specimens and in 4 of the 1 mm/min rate specimen. That is, 5 specimens out of the 23 tested could not be measured at all due to this problem and as such their results are not included in this manuscript. Additionally one of the specimens could not be tested at all due to the conditions it was poorly water-jetted where the pins could not fit in the manufactured pinholes.

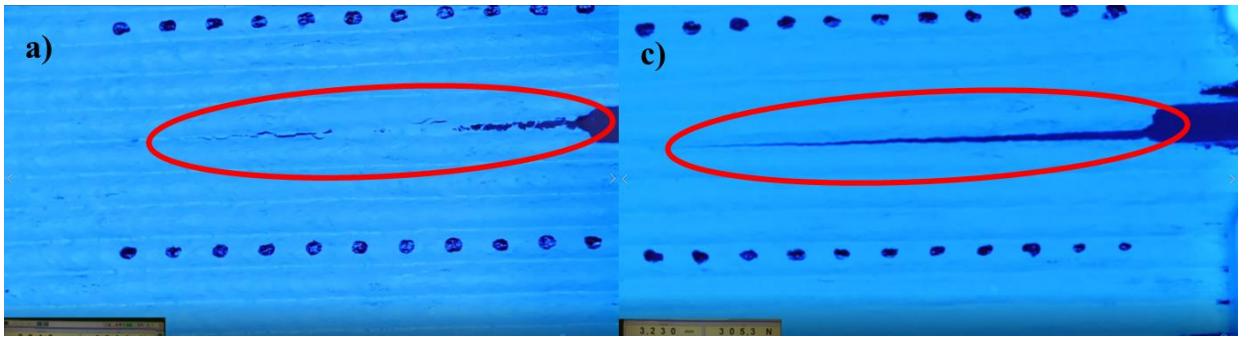

Figure 20 Comparison of a) not fully dried coating and b) dried coating.

5.2. Data Processing

The data and image processing required some time to set up the physical setup for recording; however, it proved to be a novel and efficient way of capturing the material behavior. Next step towards this is to make the MATLAB script more efficient. There are a few ways this can be improved. Other than having to change the calculations for fracture toughness, being that the formula may change on a case-to-case basis, there are many opportunities to improve in the image processing section.

One of these improvements may fall under fully automating the recognition of the calibration dots. As it stands right now, two regions of interest, ROIs, need to be set up manually to efficiently detect calibration dots. An improvement along this work included lighting to contrast surface covered with white corrector fluid against the background (crack propagation) and the

black marker dots. This helped better differentiate markings and background against the surface of the specimen at the moment of applying the binary mask which in turn gives space for improvement in the recognition of calibration dots detection by automizing the process. Similarly, the crack propagation also needed a ROI to be manually setup within the software which can also be improved upon by automizing.

The data processing software exists only as a live script in MATLAB. An app based on this script within the MATLAB software will further improve upon the processing with an interface capable of controlling values by asking for inputs pertaining to the induvial specimen to be processed (geometrical and binary mask values) and having modules that exist for the processing of the data. One module that could be added is a video trimming for the video recording of the specimen. The video before it could be processed needed to be trimmed from the moment where the tests begin to right where it ends, leaving out frames where the test was not happening. Having this integrated into the processing of data would make for more agile data processing.

5.3. FRACTURE TOUGHNESS CALCULATIONS

The RSCC fracture toughness calculations were taken from a formula used to test adhesive where the stiffness of the material being adhered is significantly larger than the adhesive being tested (see Figure 6). The specific formula used is a variation of the formula (11) from the literature review that considers side groves.

$$G_{IC} = \frac{P_c^2}{2b_n}\frac{24}{3Ebh^3}[3(a + a_0)^2 = h] \tag{12}$$

Catastrophic fracture was recorded for some of the specimens because it is difficult to manually stop the crack propagation at a specific length. This is because the limit of how much the crack should propagate was taken from the ASTM D5528 standard. While this was possible to

record on traditionally manufactured parts the results imply that the distance of how the crack propagates should be shorter. Given that the method for measuring the crack allows for a higher resolution there is no problem to shorten this distance. Additionally, it should be mentioned that crack tip sharpening, while somewhat effective as seen in the results from the exploratory work, there were still some overestimation G_{IC} at the beginning of testing. Not only was it observed in the results that at the initial crack propagation it overestimates fracture toughness but for 2 specimens, both at a rate 5 mm/min, it appeared to be that there was no impact in the initial crack propagation at all from the crack sharpening. Although the calculation worked as the crack propagated it is fit to recommend to either use a different method to sharpen the crack or to not take it into account the initial portion of the crack propagated with the rest of the fracture toughness calculations. This work resulted in an average fracture toughness of 383.3 J/m^2 compared to neat ABS which has a G_{IC} of 3947.37 J/m^2 which is a 90% decrease(Greenhalgh, 2009). According to a cited work it was expected to be a decrease in fracture toughness as a result of adding fibers and that the matrix was 3d printed. A similar results are seen in small-scale AM with an average G_{IC} of 360 J/m^2 with a standard deviation of 60 (Young et al., 2018). This cited work was based on ASTM standard D5528 with modification in the specimens' geometry.

5.4. CONCLUDING REMARKS

It would be proper to discuss some differentiation of what values should be fit to calculate fracture toughness. It is recommended to use the peaks of the crack propagation rather than all the values after crack starts to propagate. That is because it seems to be that the sudden drops in load are not representative of the materials behavior. The reason why this was challenged is that the novel method of recording seemed promising recording actual crack values compared to being recorded with a microscope as the standards calls in the traditional way to measure crack

propagation. After running a hypothesis test it was found that deflection speed has no impact on the fracture toughness calculations.

The recording system has proven to be effective and there have been some protocols and parameters that have been recognize in different aspects of the testing method that will serve for future testing and potentially in the standardization of this type of testing.

Measurements were taken of the specimens' notch fabrication. Given the limitations of the water-jet manufacturing, which was outsourced, the alignment of the notch with the layer interface imperfections was visible on a mesoscale using OGP Smartscope Flash (Quality Vision International inc., Rochester, NY, USA). Reference geometries, as seen in Figure 21a, were constructed directly referencing points of interest in the geometry (crack tip, pin holes, notch positions and interlayer positions). In Figure 21b additional constructions were made to use them as references for measurements. Lastly in Figure 16c measurements were taken, this includes the perpendicular distance, width 14, from the load line (center to center of pin holes) to the sharpened

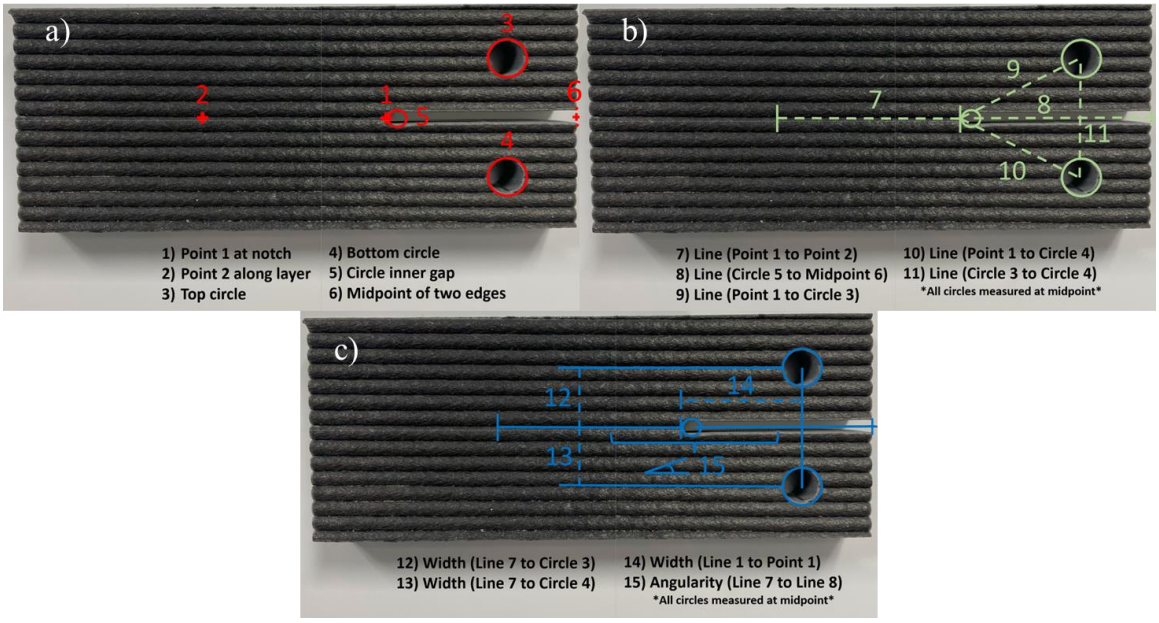

Figure 21 a) geometrical construct directly referencing specimens' geometry. b) Line constructs referencing the constructs from 1 to 6. C) Measurements taken for calculations and manufacturing correlations with results.

crack tip, perpendicular distances, widths 12 and 13, from interlayer line to pinhole centers, and angle, angularity 15, between interlayer line to load line. A more detailed explanation of these measurements and measurements for all 23 specimens tested (23 excludes specimens tested in the exploratory work) can be seen in Appendix A2. The reason for taking these measurements is to find correlations, in future work, that may exist between the results and behaviors of the test with the manufacturing intricacies of water-jet.

References

ASTM D638-22, 2022. "Standard Test Method for Tensile Properties of Plastics." ASTM International, West Conshohocken, PA [WWW Document]. URL https://compass.astm.org/document/?contentCode=ASTM%7CD0638-22%7Cen-US (accessed 3.20.23).

ASTM D5528, 2021a. "Standard Test Method for Mode I Interlaminar Fracture Toughness of Unidirectional Fiber-Reinforced Polymer Matrix Composites." ASTM International, West Conshohocken, PA. [WWW Document]. URL https://www.astm.org/d5528_d5528m-21.html (accessed 1.17.23).

ASTM D618-21, 2021b. "Standard Practice for Conditioning Plastics for Testing." ASTM International, West Conshohocken, PA [WWW Document]. URL https://www.astm.org/d0618-21.html (accessed 3.20.23).

ASTM D256-10, 2018a. "Standard Test Methods for Determining the Izod Pendulum Impact Resistance of Plastics." ASTM International, West Conshohocken, PA. [WWW Document]. URL https://compass.astm.org/document/?contentCode=ASTM%7CD0256-10R18%7Cen-US (accessed 3.20.23).

ASTM D6110-18, 2018b. "Standard Test Method for Determining the Charpy Impact Resistance of Notched Specimens of Plastics." ASTM International, West Conshohocken, PA. [WWW Document]. URL https://compass.astm.org/document/?contentCode=ASTM%7CD6110-18%7Cen-US&proxycl=https%3A%2F%2Fsecure.astm.org&fromLogin=true (accessed 3.20.23).

ASTM D3039/3039M, 2017a. "Standard Test Method for Tensile Properties of Polymer Matrix Composite Materials." ASTM International, West Conshohocken, PA [WWW Document]. URL https://compass.astm.org/document/?contentCode=ASTM%7CD3039_D3039M-17%7Cen-US&proxycl=https%3A%2F%2Fsecure.astm.org&fromLogin=true (accessed 3.20.23).

ASTM D790, 2017b. "Standard Test Methods for Flexural Properties of Unreinforced and Reinforced Plastics and Electrical Insulating Materials." ASTM International, West Conshohocken, PA [WWW Document]. URL https://compass.astm.org/document/?contentCode=ASTM%7CD0790-17%7Cen-US (accessed 3.9.23).

Billah, K.M.M., Lorenzana, F.A.R., Martinez, N.L., Wicker, R.B., Espalin, D., 2020. Thermomechanical characterization of short carbon fiber and short glass fiber-reinforced ABS used in large format additive manufacturing. Additive Manufacturing 35, 101299. https://doi.org/10.1016/j.addma.2020.101299

Borish, M., Post, B.K., Roschli, A., Chesser, P.C., Love, L.J., Gaul, K.T., Sallas, M., Tsiamis, N., 2019. In-Situ Thermal Imaging for Single Layer Build Time Alteration in Large-Scale Polymer Additive Manufacturing. Procedia Manufacturing, 47th SME North American Manufacturing Research Conference, NAMRC 47, Pennsylvania, USA. 34, 482–488. https://doi.org/10.1016/j.promfg.2019.06.202

Caltagirone, P.E., Cousins, D.D., Snowberg, D., Stebner, D.A.P., 2020. DETERMINING MODE I FRACTURE TOUGHNESS OF ADHESIVE COMPOSITE JOINTS: AUTONOMOUS CRACK TRACKING USING MATLAB DEVELOPED PROGRAM.

Colón Quintana, J.L., Slattery, L., Pinkham, J., Keaton, J., Lopez-Anido, R.A., Sharp, K., 2022. Effects of Fiber Orientation on the Coefficient of Thermal Expansion of Fiber-Filled Polymer Systems in Large Format Polymer Extrusion-Based Additive Manufacturing. Materials 15, 2764. https://doi.org/10.3390/ma15082764

Curran, S., Chambon, P., Lind, R., Love, L., Wagner, R., Whitted, S., Smith, D., Post, B., Graves, R., Blue, C., Green, J., Keller, M., 2016. Big Area Additive Manufacturing and Hardware-in-the-Loop for Rapid Vehicle Powertrain Prototyping: A Case Study on the Development of a 3-D-Printed Shelby Cobra. Presented at the SAE 2016 World Congress and Exhibition, pp. 2016-01–0328. https://doi.org/10.4271/2016-01-0328

Davies, P., Benzeggagh, M.L., 1989. Chapter 3 - Interlaminar Mode-I Fracture Testing, in: Friedrich, K. (Ed.), Composite Materials Series, Application of Fracture Mechanics to Composite Materials. Elsevier, pp. 81–112. https://doi.org/10.1016/B978-0-444-87286-9.50007-3

Duty, C., Love, L., 2015. Cincinnati Big Area Additive Manufacturing (BAAM) (No. ORNL/TM-2015/100, 1210140, CRADA/NFE-14-04957). https://doi.org/10.2172/1210140

Forster, A.M., 2015. Materials Testing Standards for Additive Manufacturing of Polymer Materials: State of the Art and Standards Applicability (No. NIST IR 8059). National Institute of Standards and Technology. https://doi.org/10.6028/NIST.IR.8059

Greenhalgh, E., 2009. Failure Analysis and Fractography of Polymer Composites. Elsevier.

Hill, C., Bedsole, R., Rowe, K., Duty, C., Ajinjeru, C., Kunc, V., Riha, D., 2018. Big Area Additive Manufacturing (BAAM) Materials Development and Reinforcement with Advanced Composites (No. IACMI/-0015-2017/3.6). Inst. for Advanced Composites Manufacturing Innovation (IACMI), Knoxville, TN (United States). https://doi.org/10.2172/1434289

Khan, R., 2019. Fiber bridging in composite laminates: A literature review. Composite Structures 229, 111418. https://doi.org/10.1016/j.compstruct.2019.111418

Kinloch, A.J., Shaw, S.J., Tod, D.A., Hunston, D.L., 1983. Deformation and fracture behaviour of a rubber-toughened epoxy: 1. Microstructure and fracture studies. Polymer 24, 1341–1354. https://doi.org/10.1016/0032-3861(83)90070-8

Kishore, V., Ajinjeru, C., Nycz, A., Post, B., Lindahl, J., Kunc, V., Duty, C., 2017. Infrared preheating to improve interlayer strength of big area additive manufacturing (BAAM) components. Additive Manufacturing 14, 7–12. https://doi.org/10.1016/j.addma.2016.11.008

Kumar, V., Alwekar, S.P., Kunc, V., Cakmak, E., Kishore, V., Smith, T., Lindahl, J., Vaidya, U., Blue, C., Theodore, M., Kim, S., Hassen, A.A., 2021. High-performance molded composites using additively manufactured preforms with controlled fiber and pore morphology. Additive Manufacturing 37, 101733. https://doi.org/10.1016/j.addma.2020.101733

Meraz Trejo, E., Jimenez, X., Billah, K.M.M., Seppala, J., Wicker, R., Espalin, D., 2020. Compressive deformation analysis of large area pellet-fed material extrusion 3D printed parts in relation to in situ thermal imaging. Additive Manufacturing 33, 101099. https://doi.org/10.1016/j.addma.2020.101099

Mostovoy, S., Crosley, P., Ripling, E., 1967. Use of Crack-Line-Loaded Specimens for Measuring Plane-Strain Fracture Toughness. Journal of Materials 2, 661-.

Musio-Sale, M., Nazzaro, P.L., Peterson, E., 2020. Visions, Concepts, and Applications in Additive Manufacturing for Yacht Design, in: Di Nicolantonio, M., Rossi, E., Alexander, T. (Eds.), Advances in Additive Manufacturing, Modeling Systems and 3D Prototyping, Advances in Intelligent Systems and Computing. Springer International Publishing, Cham, pp. 401–410. https://doi.org/10.1007/978-3-030-20216-3_37

Nestor Perez, 2004. 6 The Energy Principle, in: Fracture Mechanics. Springer, Boston.

Nycz, A., Kishore, V., Lindahl, J., Duty, C., Carnal, C., Kunc, V., 2020. Controlling substrate temperature with infrared heating to improve mechanical properties of large-scale printed parts. Additive Manufacturing 33, 101068. https://doi.org/10.1016/j.addma.2020.101068

Pappas, J.M., Thakur, A.R., Leu, M.C., Dong, X., 2021. A Comparative Study of Pellet-Based Extrusion Deposition of Short, Long, and Continuous Carbon Fiber-Reinforced Polymer

Composites for Large-Scale Additive Manufacturing. Journal of Manufacturing Science and Engineering 143. https://doi.org/10.1115/1.4049646
Ripling, E.J., Mostovoy, S., Corten, H.T., 1971. Fracture Mechanics: A Tool for Evaluating Structural Adhesives. The Journal of Adhesion 3, 107–123. https://doi.org/10.1080/00218467108081158
Schnittker, K., Arrieta, E., Jimenez, X., Espalin, D., Wicker, R.B., Roberson, D.A., 2019. Integrating digital image correlation in mechanical testing for the materials characterization of big area additive manufacturing feedstock. Additive Manufacturing 26, 129–137. https://doi.org/10.1016/j.addma.2018.12.016
Smiley, A.J., Pipes, R.B., 1987. Rate Effects on Mode I Interlaminar Fracture Toughness in Composite Materials. Journal of Composite Materials 21, 670–687. https://doi.org/10.1177/002199838702100706
Spoerk, M., Savandaiah, C., Arbeiter, F., Traxler, G., Cardon, L., Holzer, C., Sapkota, J., 2018. Anisotropic properties of oriented short carbon fibre filled polypropylene parts fabricated by extrusion-based additive manufacturing. Composites Part A: Applied Science and Manufacturing 113, 95–104. https://doi.org/10.1016/j.compositesa.2018.06.018
Spreeman, M.E., Stretz, H.A., Dadmun, M.D., 2019. Role of compatibilizer in 3D printing of polymer blends. Additive Manufacturing 27, 267–277. https://doi.org/10.1016/j.addma.2019.03.009
Winter, K., Wilfert, J., Häupler, B., Erlmann, J., Altstädt, V., 2022. Large Scale 3D Printing: Influence of Fillers on Warp Deformation and on Mechanical Properties of Printed Polypropylene Components. Macromolecular Materials and Engineering 307, 2100528. https://doi.org/10.1002/mame.202100528
Yamawaki, M., Kouno, Y., 2018. Fabrication and mechanical characterization of continuous carbon fiber-reinforced thermoplastic using a preform by three-dimensional printing and via hot-press molding. Advanced Composite Materials 27, 209–219. https://doi.org/10.1080/09243046.2017.1368840
Yang, D., Zhang, H., Wu, J., McCarthy, E.D., 2021. Fibre flow and void formation in 3D printing of short-fibre reinforced thermoplastic composites: An experimental benchmark exercise. Additive Manufacturing 37, 101686. https://doi.org/10.1016/j.addma.2020.101686
Yeole, P., Kim, S., Hassen, A.A., Kumar, V., Kunc, V., Vaidya, U., 2021. Large-scale additive manufacturing tooling for extrusion-compression molds. Additive Manufacturing Letters 1, 100007. https://doi.org/10.1016/j.addlet.2021.100007
Young, D., Wetmore, N., Czabaj, M., 2018. Interlayer fracture toughness of additively manufactured unreinforced and carbon-fiber-reinforced acrylonitrile butadiene styrene. Additive Manufacturing 22, 508–515. https://doi.org/10.1016/j.addma.2018.02.023

Appendix

A1. DCB Testing Results

The testing results are grouped by specimen. See tag on the title of each graph (E.g. 1B1R):

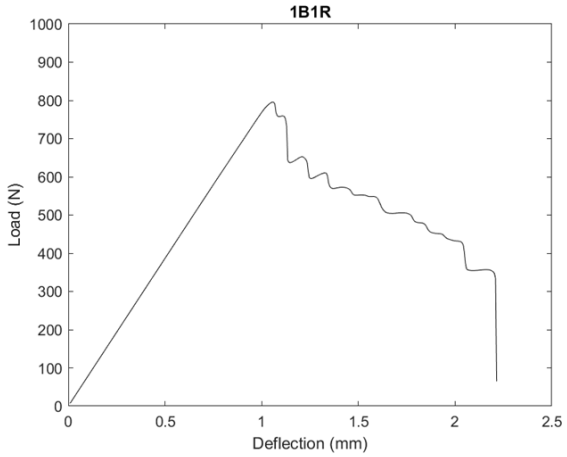

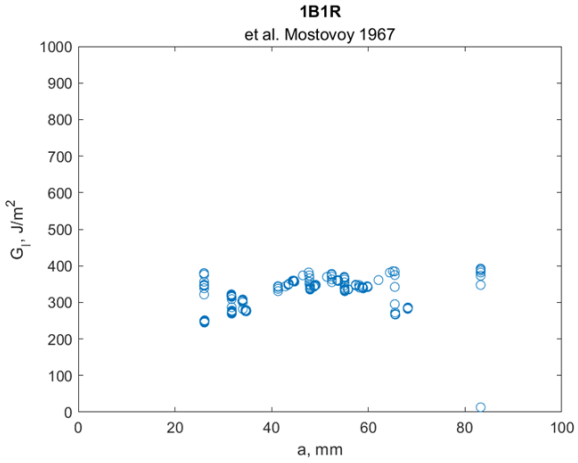

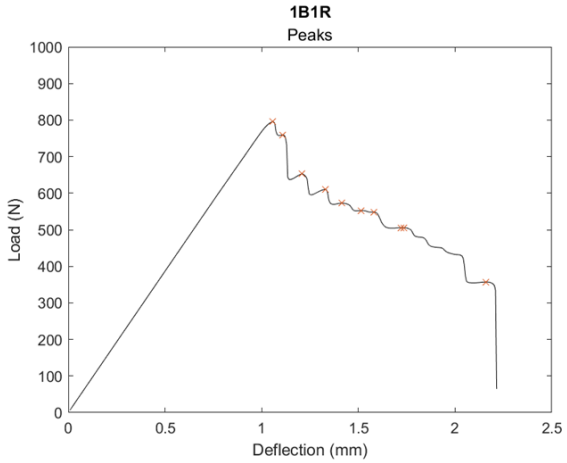

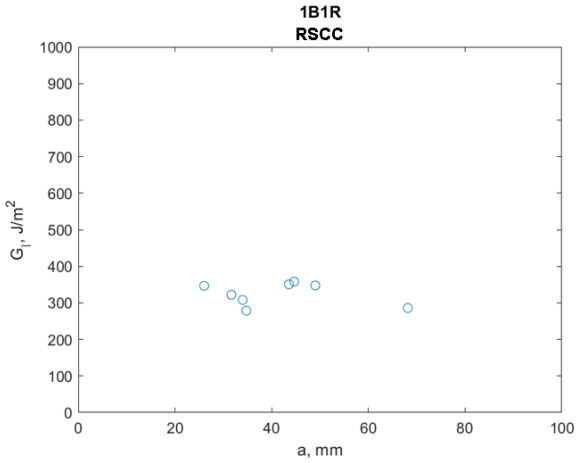

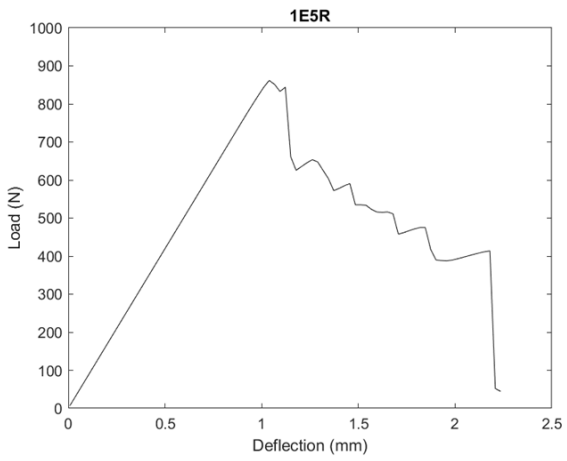
1E5R
Load (N)
Deflection (mm)

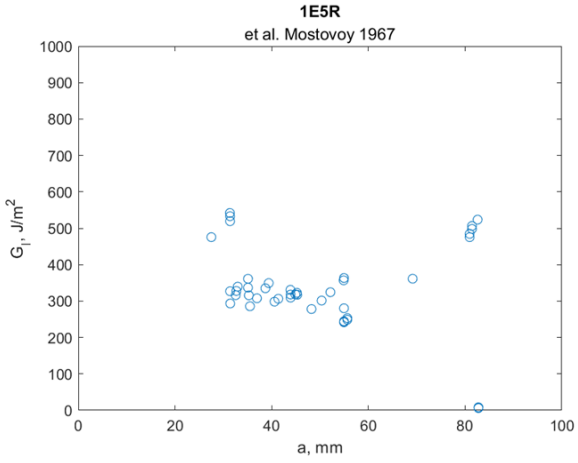
1E5R
et al. Mostovoy 1967
G_I, J/m^2
a, mm

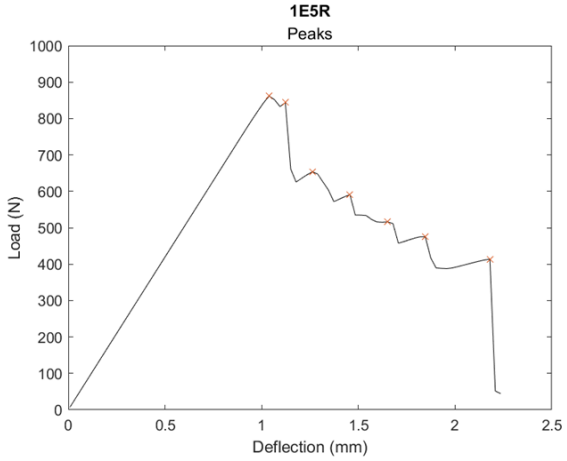
1E5R
Peaks
Load (N)
Deflection (mm)

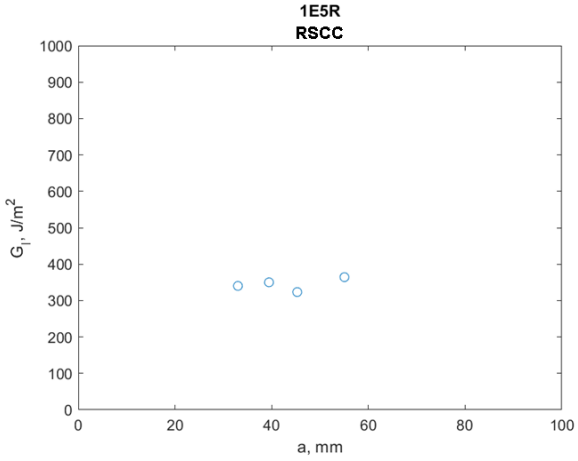
1E5R
RSCC
G_I, J/m^2
a, mm

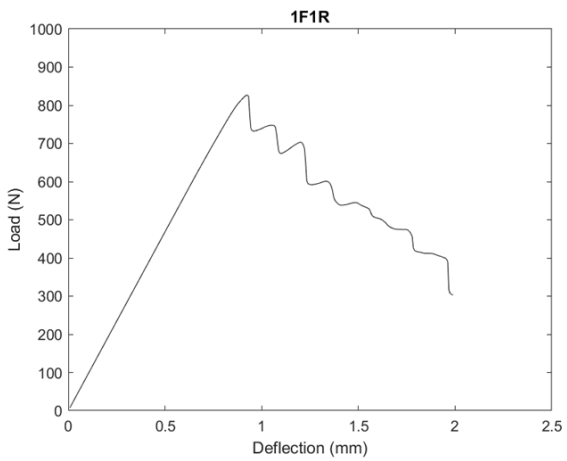
1F1R
Load (N)
Deflection (mm)

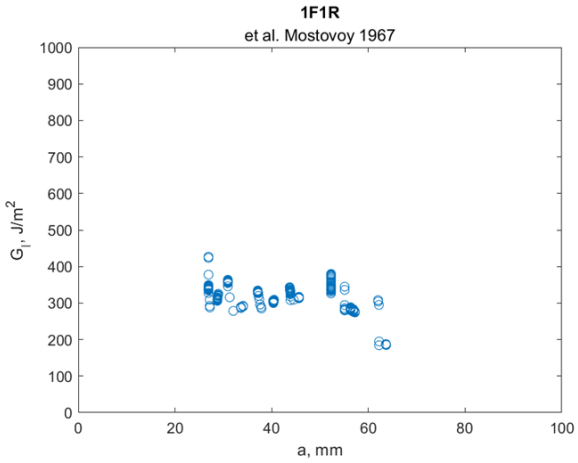
1F1R
et al. Mostovoy 1967
G_I, J/m^2
a, mm

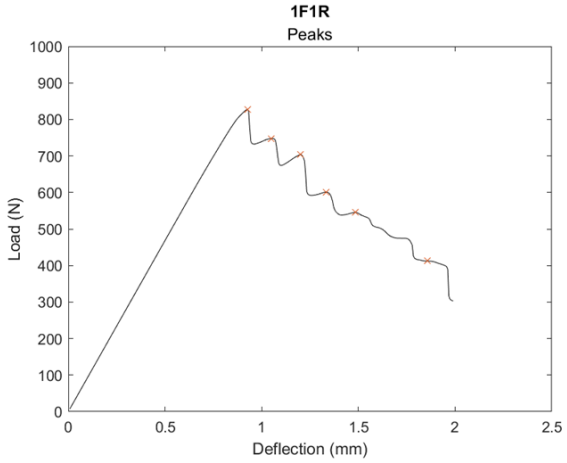
1F1R
Peaks
Load (N)
Deflection (mm)

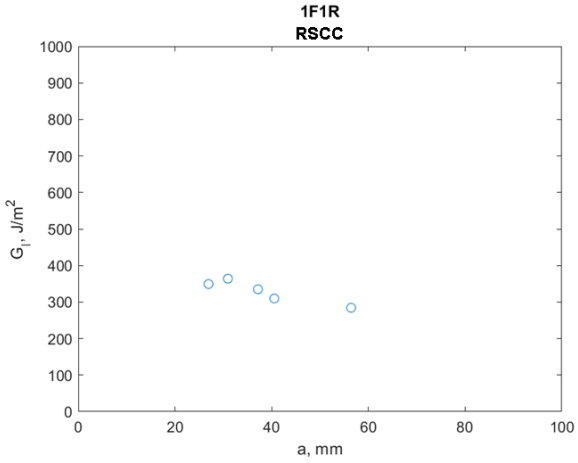
1F1R
RSCC
G_I, J/m^2
a, mm

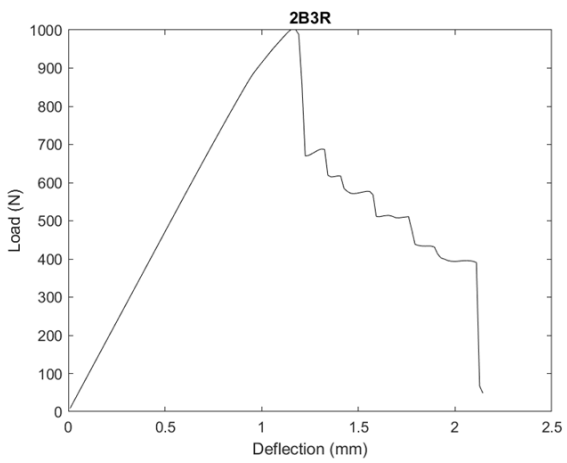
2B3R
Load (N)
Deflection (mm)

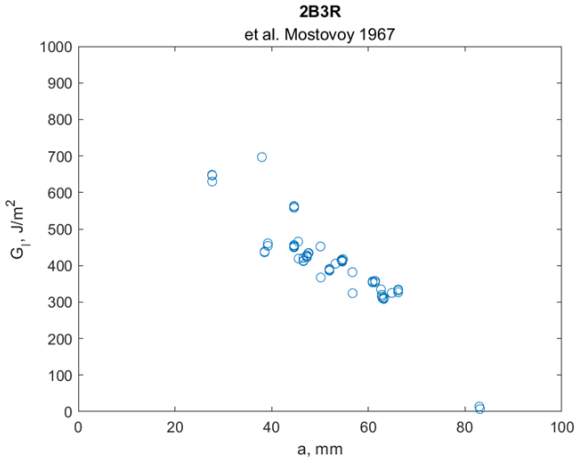
2B3R
et al. Mostovoy 1967
G_I, J/m^2
a, mm

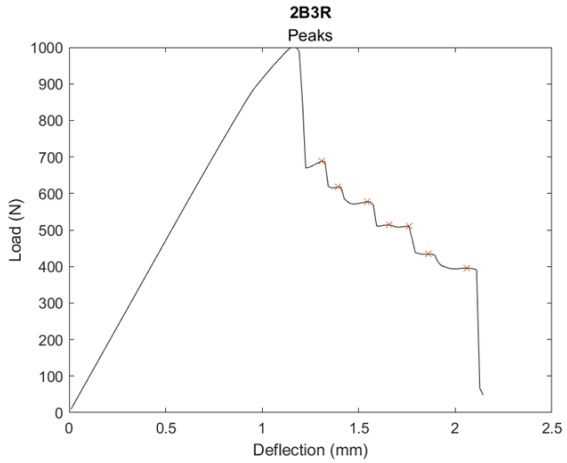
2B3R
Peaks
Load (N)
Deflection (mm)

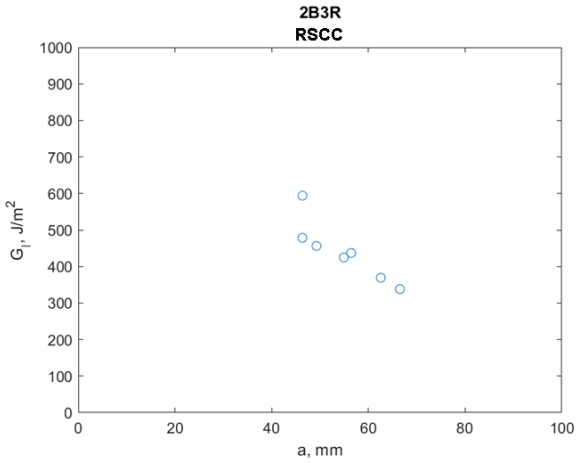
2B3R
RSCC
G_I, J/m^2
a, mm

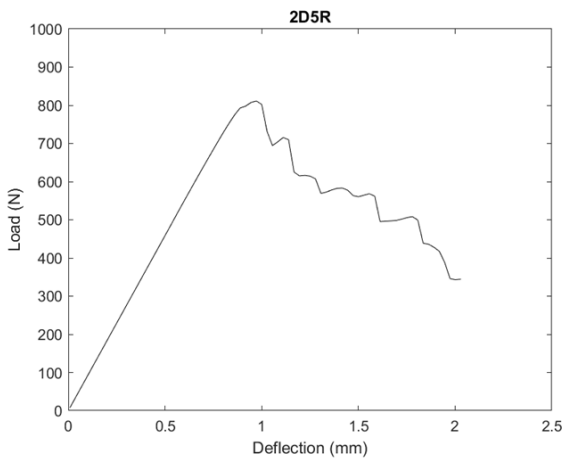
2D5R
Load (N)
Deflection (mm)

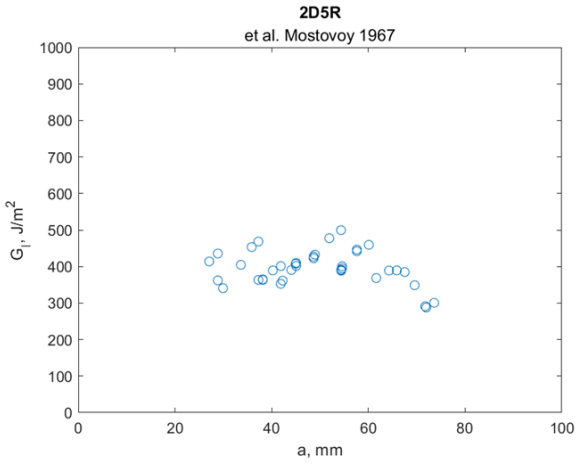
2D5R
et al. Mostovoy 1967
G_I, J/m^2
a, mm

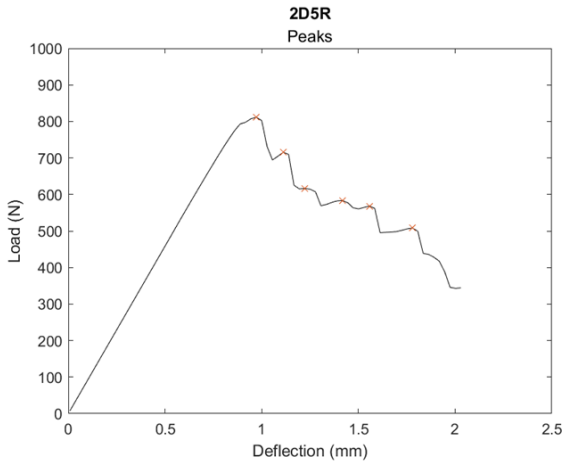
2D5R
Peaks
Load (N)
Deflection (mm)

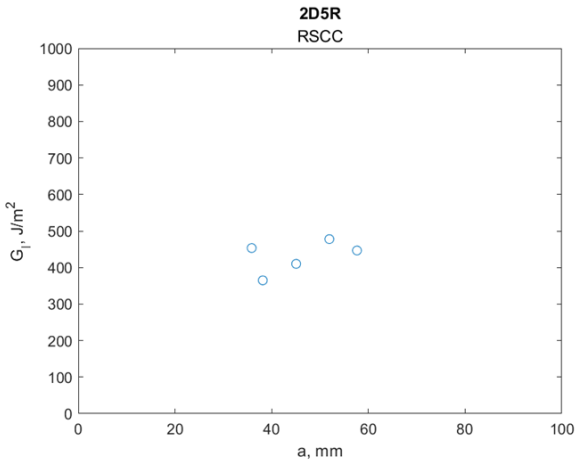
2D5R
RSCC
G_I, J/m^2
a, mm

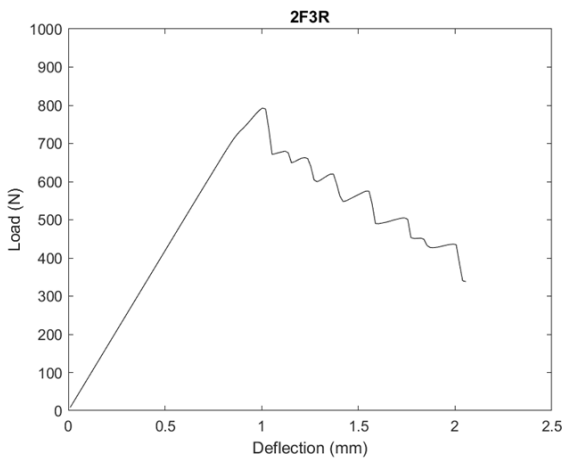
2F3R
Load (N)
Deflection (mm)

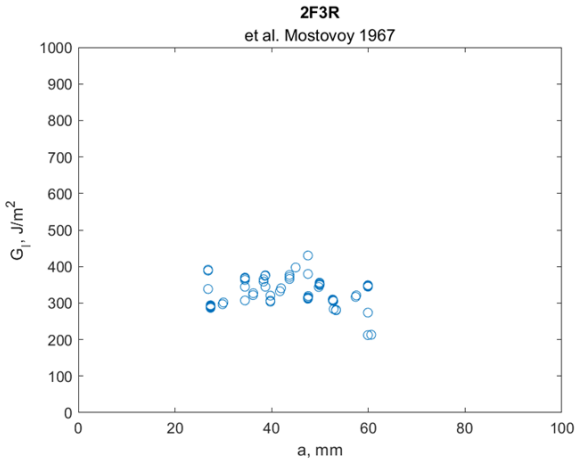
2F3R
et al. Mostovoy 1967
G_I, J/m^2
a, mm

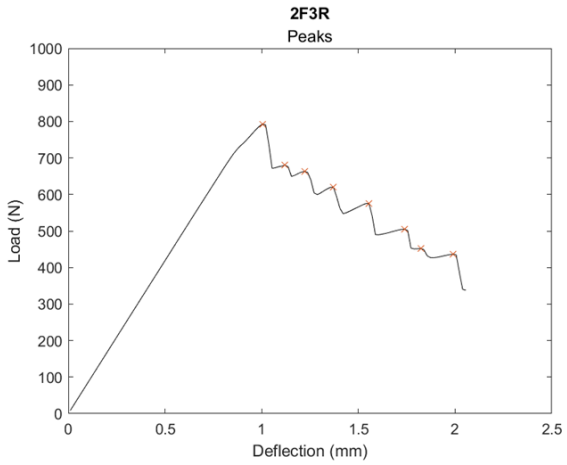
2F3R
Peaks
Load (N)
Deflection (mm)

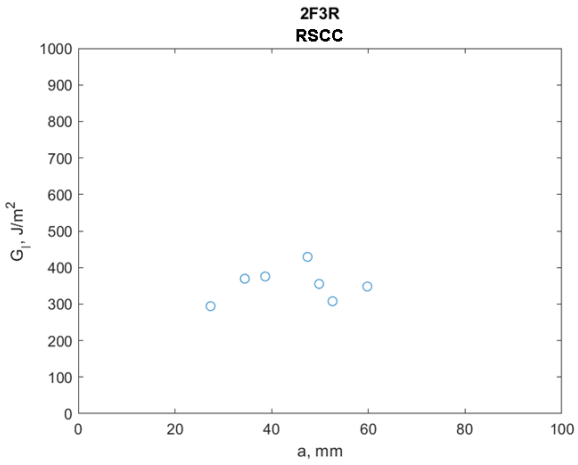
2F3R
RSCC
G_I, J/m^2
a, mm

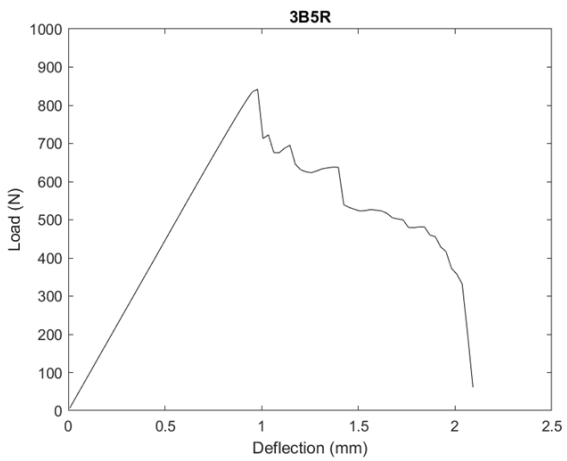
3B5R
Load (N)
Deflection (mm)

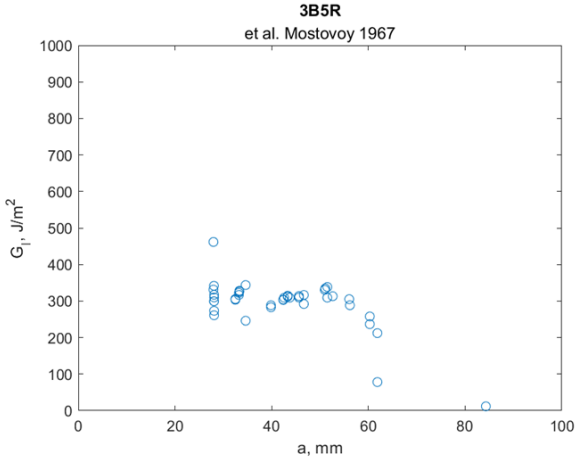
3B5R
et al. Mostovoy 1967
G_I, J/m^2
a, mm

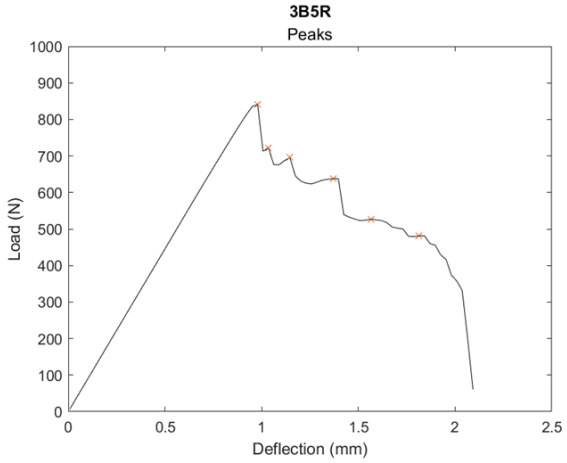
3B5R
Peaks
Load (N)
Deflection (mm)

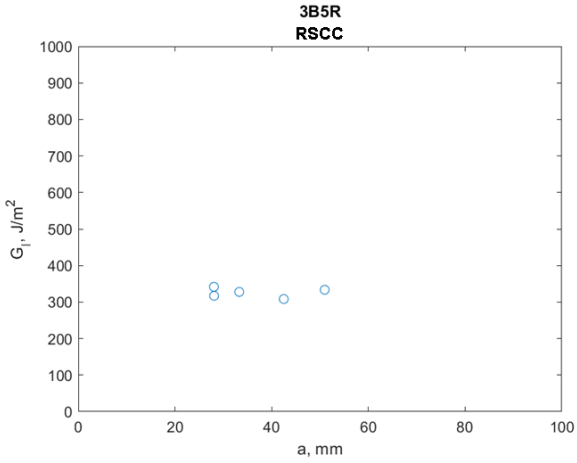
3B5R
RSCC
G_I, J/m^2
a, mm

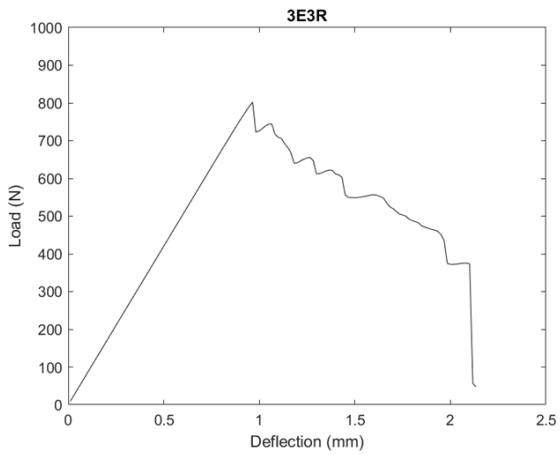
3E3R
Load (N)
Deflection (mm)

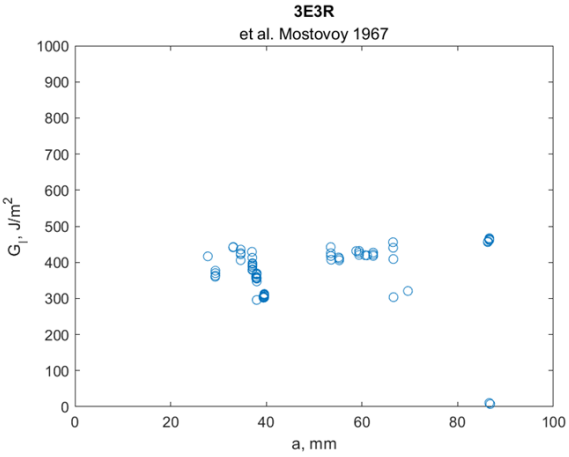
3E3R
et al. Mostovoy 1967
G_I, J/m^2
a, mm

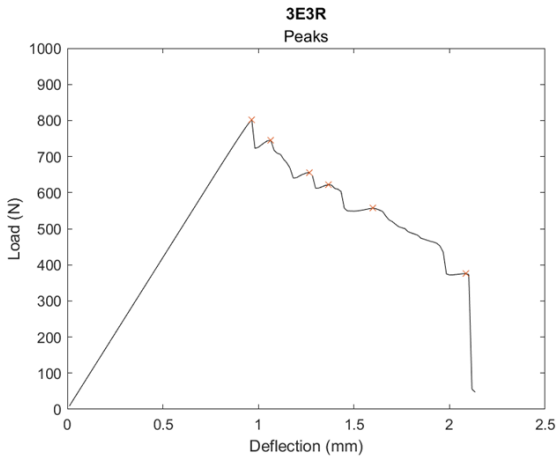
3E3R
Peaks
Load (N)
Deflection (mm)

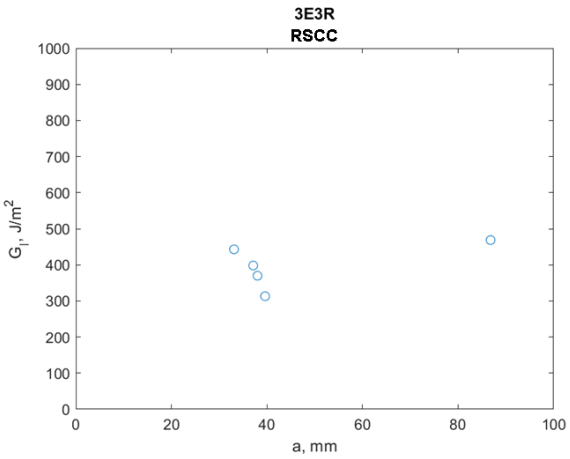
3E3R
RSCC
G_I, J/m^2
a, mm

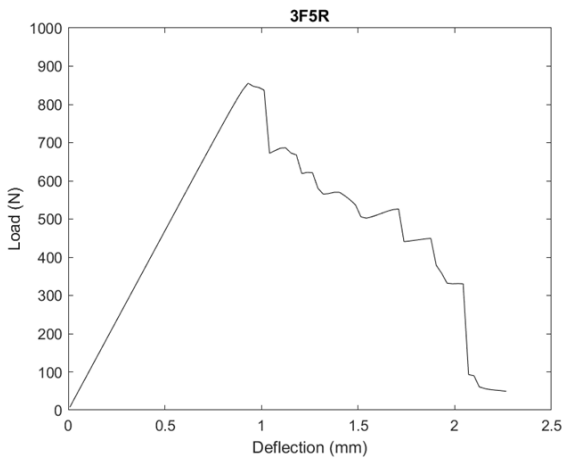
3F5R
Load (N)
Deflection (mm)


3F5R
et al. Mostovoy 1967
G_I, J/m^2
a, mm

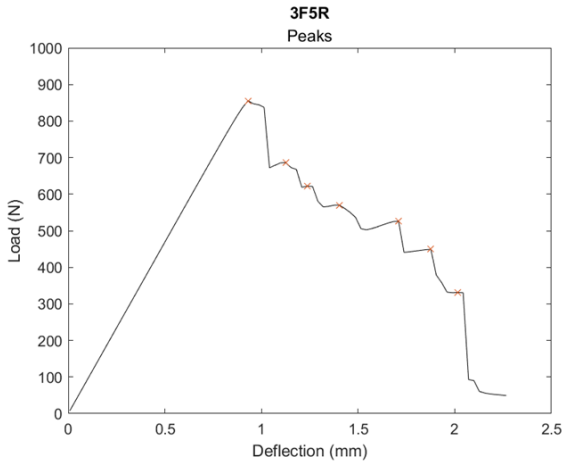
3F5R
Peaks
Load (N)
Deflection (mm)

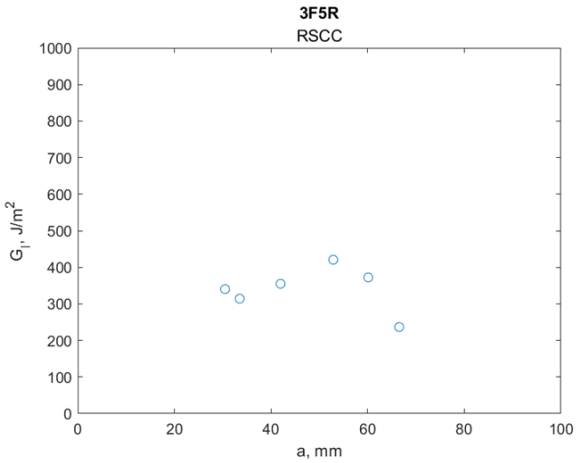
3F5R
RSCC
G_I, J/m^2
a, mm

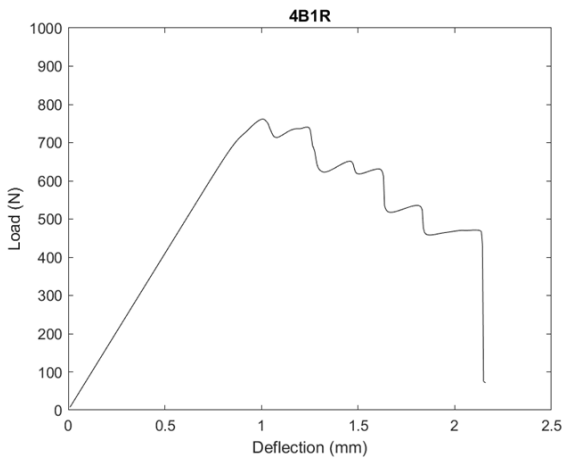
4B1R
Load (N)
Deflection (mm)

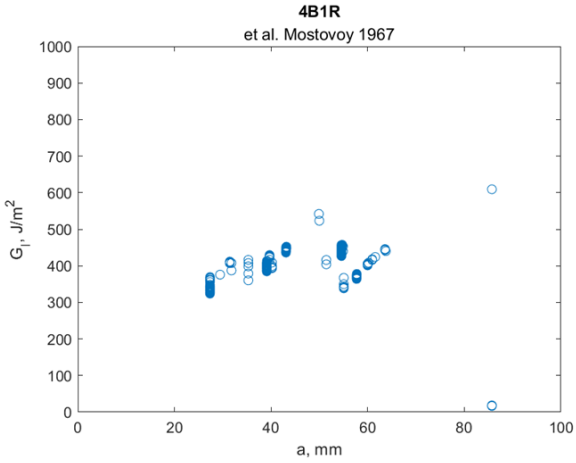
4B1R
et al. Mostovoy 1967
G_I, J/m^2
a, mm

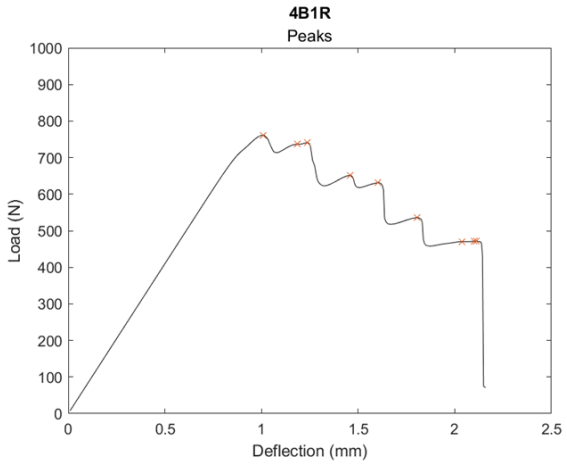
4B1R
Peaks
Load (N)
Deflection (mm)

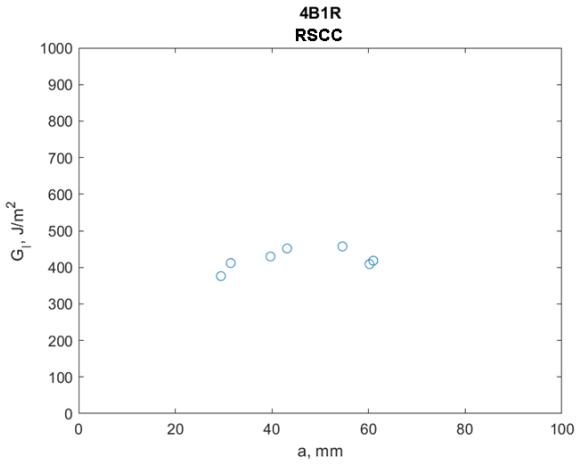
4B1R
RSCC
G_I, J/m^2
a, mm

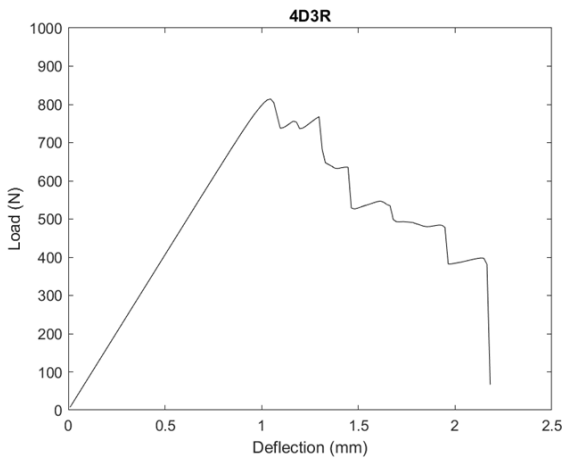
4D3R
Load (N)
Deflection (mm)

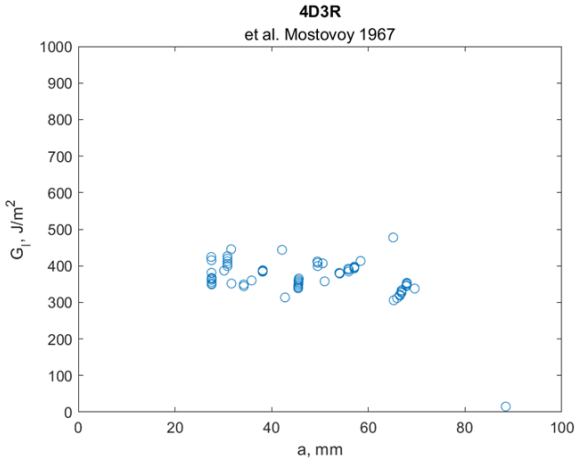
4D3R
et al. Mostovoy 1967
G_I, J/m^2
a, mm

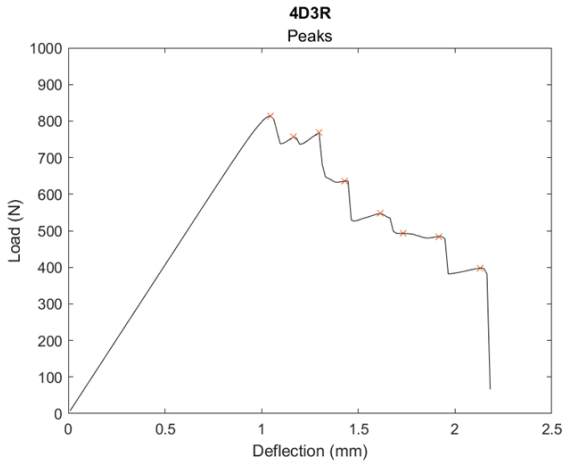
4D3R
Peaks
Load (N)
Deflection (mm)

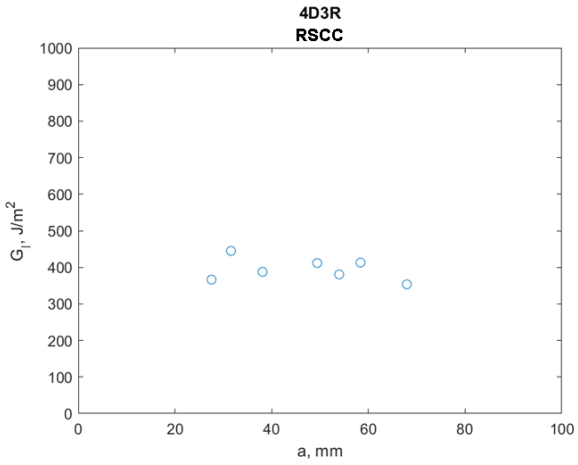
4D3R
RSCC
G_I, J/m^2
a, mm

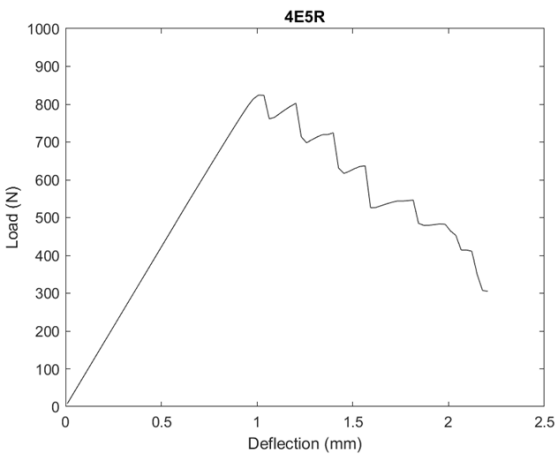
4E5R
Load (N)
Deflection (mm)

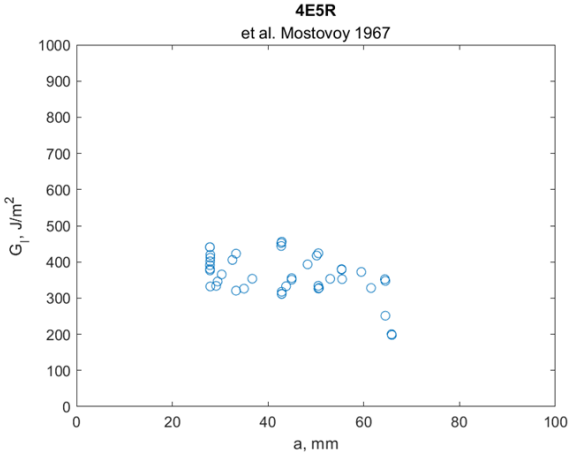
4E5R
et al. Mostovoy 1967
G_I, J/m^2
a, mm

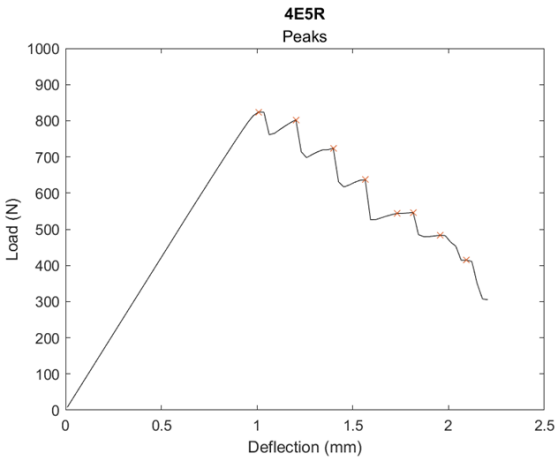
4E5R
Peaks
Load (N)
Deflection (mm)

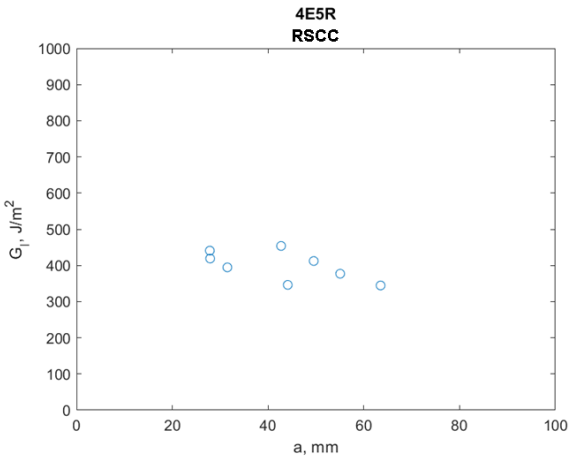
4E5R
RSCC
G_I, J/m^2
a, mm

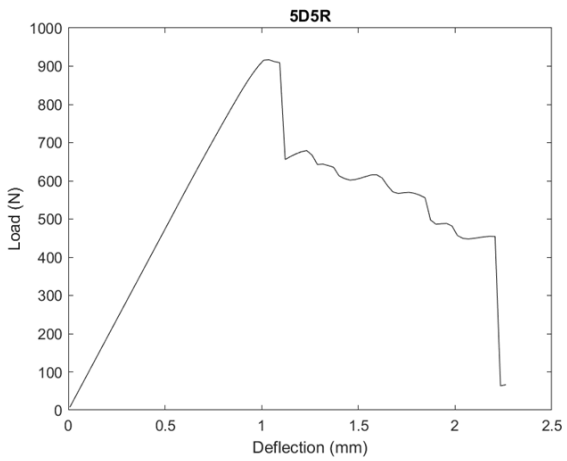
5D5R
Load (N)
Deflection (mm)

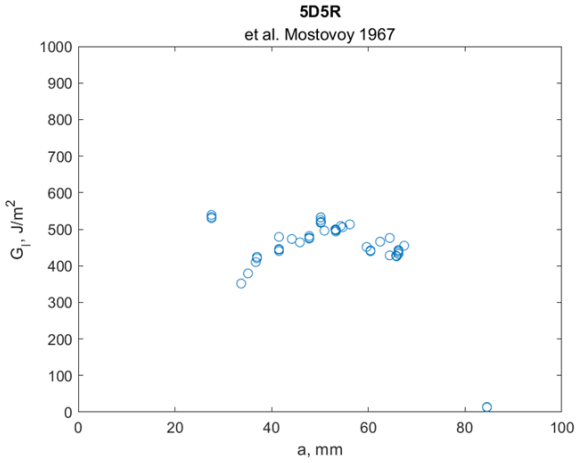
5D5R
et al. Mostovoy 1967
G_I, J/m^2
a, mm

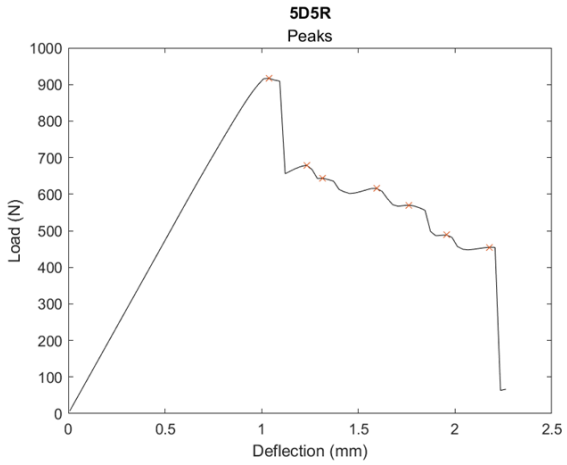
5D5R
Peaks
Load (N)
Deflection (mm)

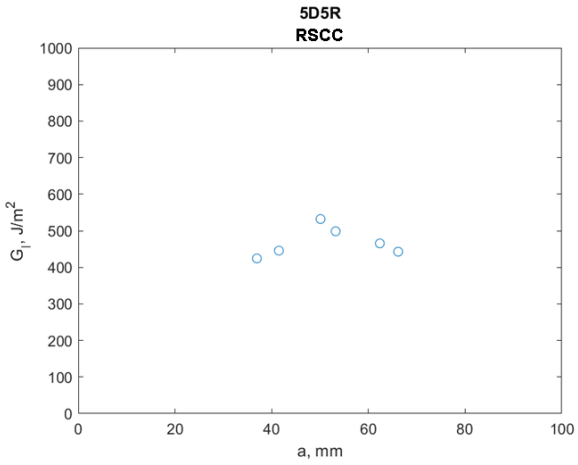
5D5R
RSCC
G_I, J/m^2
a, mm

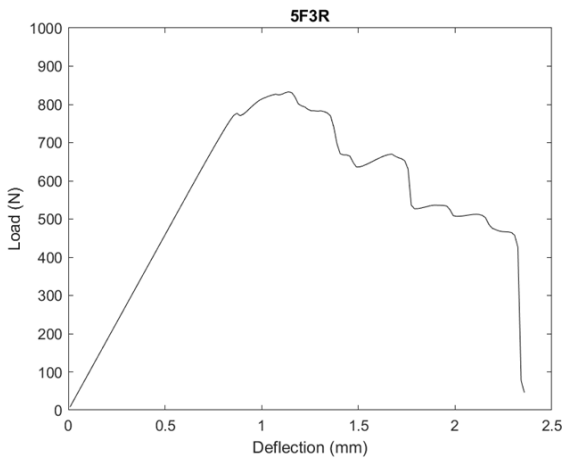
5F3R
Load (N)
Deflection (mm)

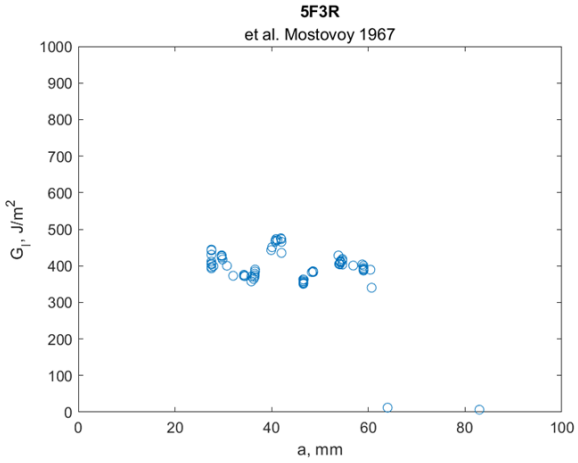
5F3R
et al. Mostovoy 1967
G_I, J/m^2
a, mm

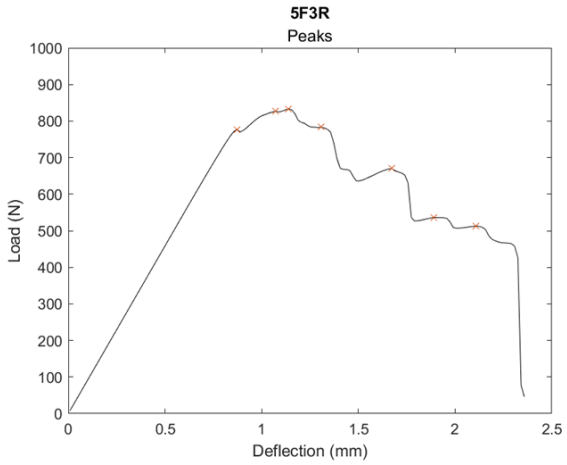
5F3R
Peaks
Load (N)
Deflection (mm)

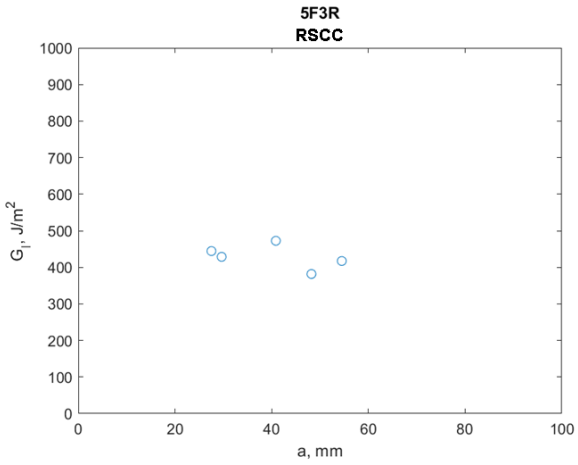
5F3R
RSCC
G_I, J/m^2
a, mm

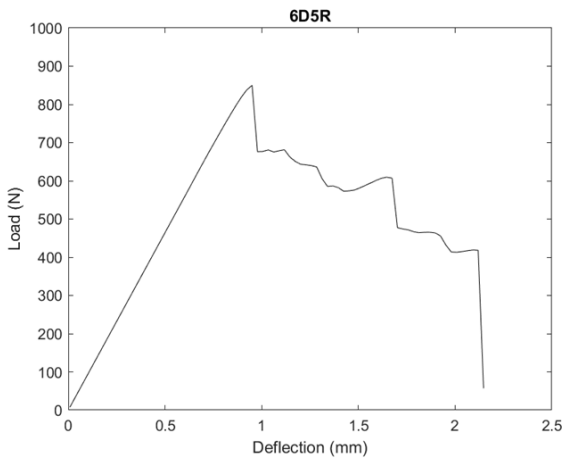
6D5R
Load (N)
Deflection (mm)

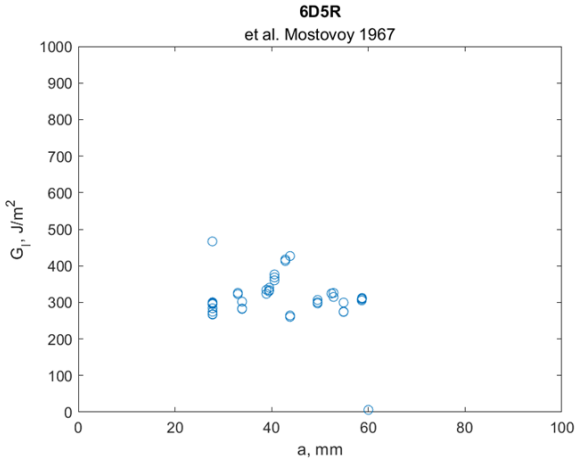
6D5R
et al. Mostovoy 1967
G_I, J/m^2
a, mm

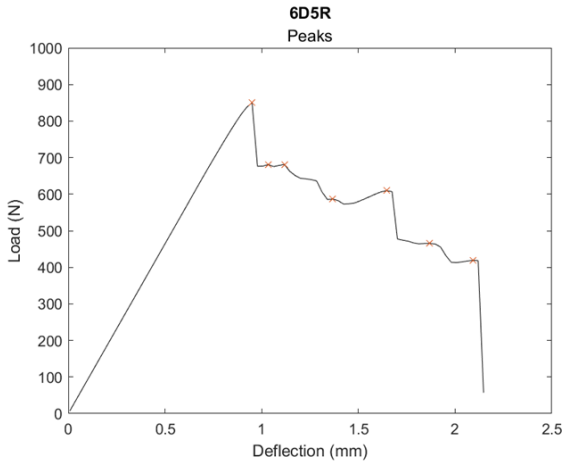
6D5R
Peaks
Load (N)
Deflection (mm)

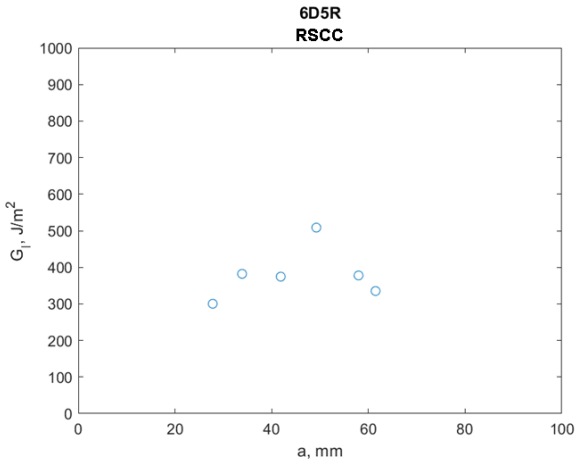
6D5R
RSCC
G_I, J/m^2
a, mm

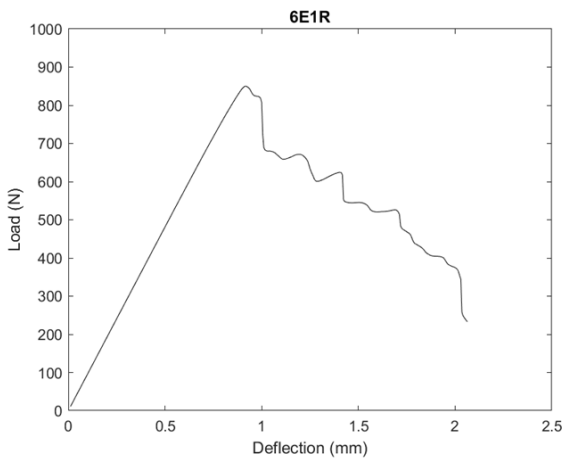
6E1R
Load (N)
Deflection (mm)

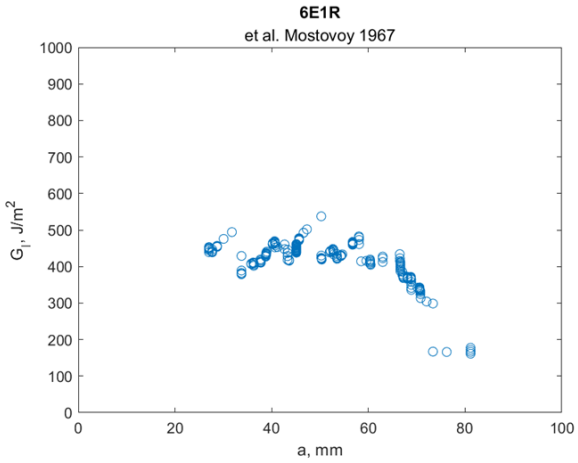
6E1R
et al. Mostovoy 1967
G_I, J/m^2
a, mm

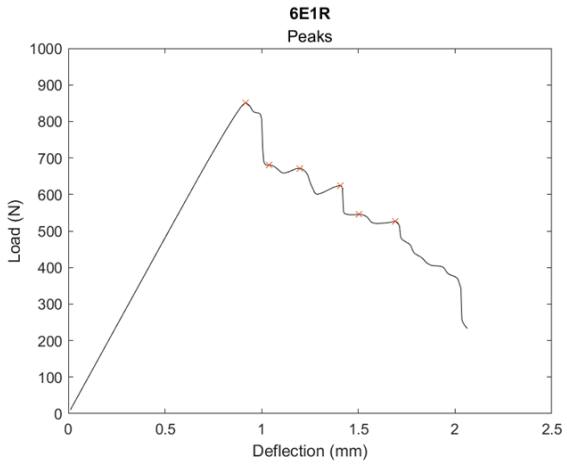
6E1R
Peaks
Load (N)
Deflection (mm)

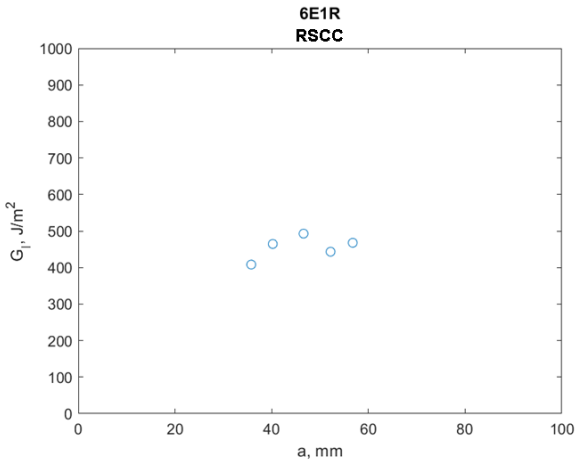
6E1R
RSCC
G_I, J/m^2
a, mm

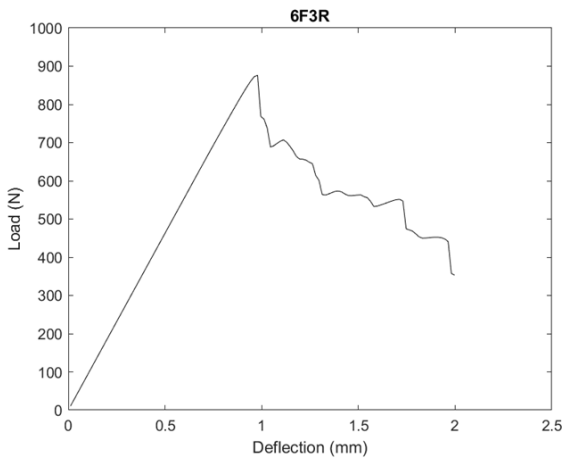
6F3R
Load (N)
Deflection (mm)

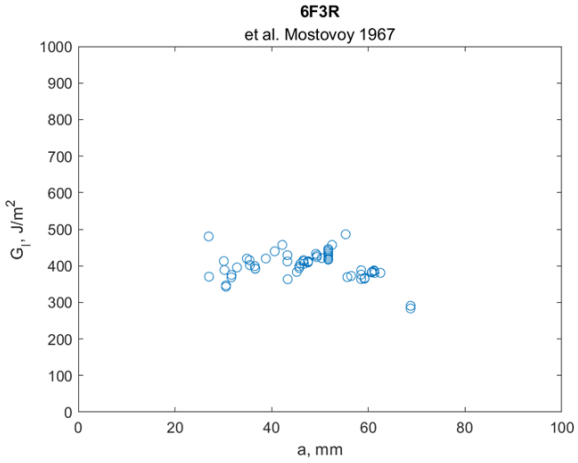
6F3R
et al. Mostovoy 1967
G_I, J/m^2
a, mm

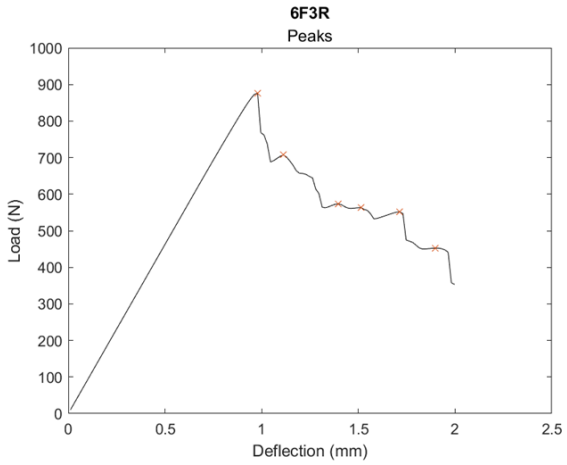
6F3R
Peaks
Load (N)
Deflection (mm)

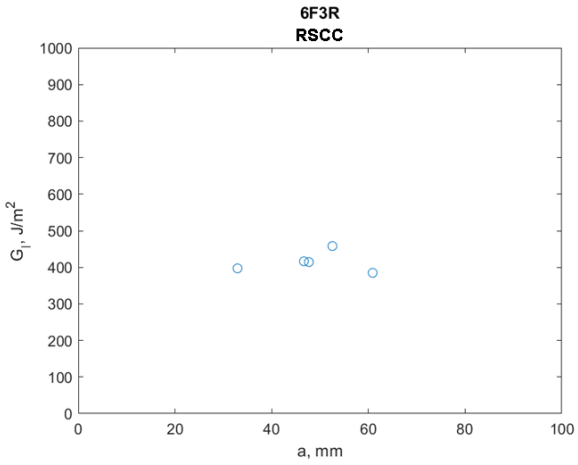
6F3R
RSCC
G_I, J/m^2
a, mm

A2. DCB Measurements

Measurements are first taken as seen in the example picture a) first. Posteriorly line constructs are taken to use as reference for measurements as seen in picture b). Finally measurements are taken of the distance of the top and bottom pin-hole perpendicular to the interlayer line, *7*, the measurement 14, which is perpendicular to the line connecting the pin-holes, line *11,* is the distance from the load line to the tip of the pre-crack, A_0, which was used in the script as the initial distance for fracture toughness calculations.

The references and measurements were taken step by step, hence the numbers and order fashion. From step 1 to 6 we have all the references taken from the sample in question, i.e. 1B, 5F, etc. From steps 7 to 11 were additional constructions needed to take measurements using the references from 1 to 6. The last 4 steps were measurements taken using both constructs and references. It should be noted that while the previous statements are always true, individual features are not always in the same step. In the following picture it is easy to differentiate since all features have coordinates and which steps were used to construct or measure under the column called *Reference*.

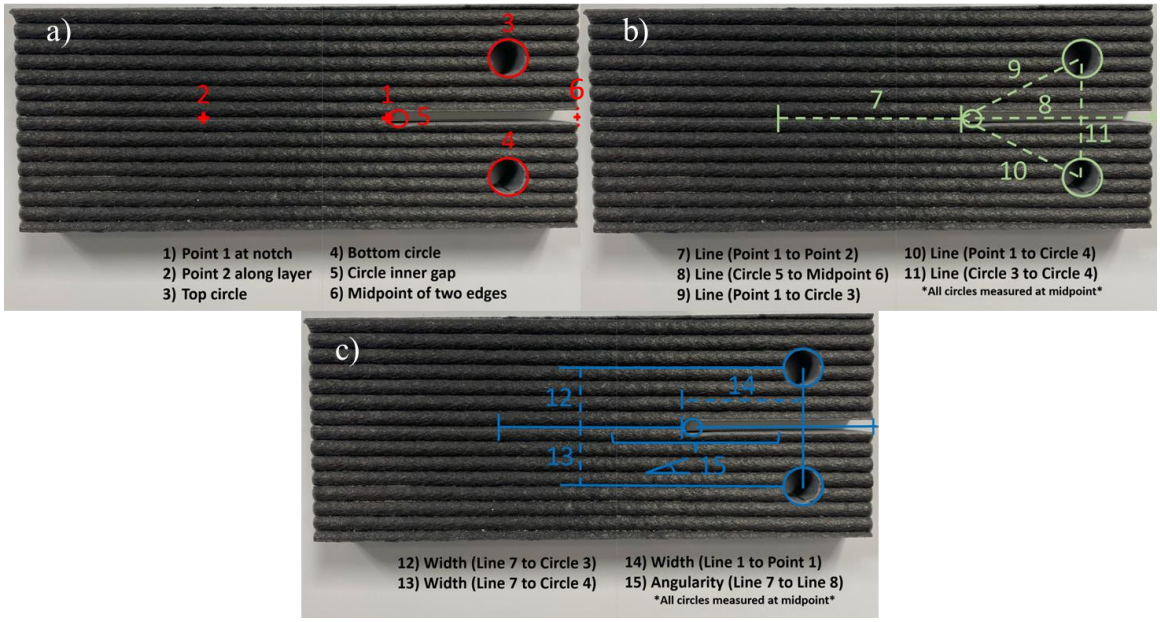

DCB_1C						
Step	Feature	X/R Location	Y/A Location	Z Location	Size	Reference
1	Point	168.33015	58.20604	39.83692		
2	Circle	195.80111	46.34863	39.83692	7.5479	
3	Circle	194.8865	72.86092	39.8369	7.68395	
4	Midpoint	211.22537	60.32861	39.83742	2.56946	
5	Circle	170.44774	58.91669	39.83742	3.14192	
6	Point	137.57908	57.41193	39.83692		
7	Line	152.95462	57.80898	39.83692	1.47928	6 1
8	Line	190.83655	59.62265	39.83742	-178.017	4 5
9	Line	195.34381	59.60478	39.83691	-88.0242	3 2
10	Line	182.06563	52.27733	39.83692	-23.3467	1 2
11	Line	181.60833	65.53348	39.83691	28.89171	1 3
12	Width	181.84502	58.67227	39.83692	27.04582	1 9
13	Angularity				0.27047	8 7
14	Width	195.06675	65.88103	39.83691	13.96443	7 3
15	Width	195.63895	52.62785	39.83692	12.56264	7 2

DCB_1D						
Step	Feature	X/R Location	Y/A Location	Z Location	Size	Reference
1	Point	239.00281	59.76495	40.42642		
2	Point	227.29886	60.30335	40.42642		
3	Circle	265.67375	72.34833	40.42642	6.49742	
4	Circle	264.82817	45.90138	40.42592	6.45504	
5	Circle	240.46938	59.96843	40.42592	1.84034	
6	Midpoint	281.53134	58.63246	40.42592	1.53365	
7	Line	233.15084	60.03415	40.42642	177.3662	1 2
8	Line	261.00036	59.30045	40.42592	-1.86349	5 6
9	Line	253.07156	66.15838	40.42617	26.15937	5 3
10	Line	252.64877	52.9349	40.42592	-30.0062	5 4
11	Line	265.25096	59.12485	40.42617	-91.8313	3 4
12	Width	265.35677	65.45777	40.42642	13.7957	7 3
13	Width	265.1191	52.22577	40.42617	12.66217	7 4
14	Width	252.1237	59.34544	40.42629	26.2552	11 1
15	Angularity				0.55236	7 8

DCB_1E						
Step	Feature	X/R Location	Y/A Location	Z Location	Size	Reference
1	Point	213.63599	70.24269	40.42542		
2	Point	189.29678	70.05417	40.42542		
3	Circle	241.13099	83.61383	40.42592	7.72985	
4	Circle	241.17619	57.1294	40.42592	7.79799	
5	Circle	215.9252	70.43721	40.42592	2.56319	
6	Midpoint	256.91814	70.40728	40.42592	2.82403	
7	Line	201.46639	70.14843	40.42542	-179.556	1 2
8	Line	236.42167	70.42224	40.42592	-0.04184	5 6
9	Line	228.52809	77.02552	40.42592	27.59884	5 3
10	Line	228.55069	63.7833	40.42592	-27.7902	5 4
11	Line	241.15359	70.37161	40.42592	-89.9022	3 4
12	Width	241.18195	77.03513	40.42567	13.15779	7 3
13	Width	241.12458	63.7923	40.42567	13.3262	7 4
14	Width	227.39486	70.26617	40.42567	27.51778	11 1
15	Angularity				0.34743	7 8

DCB_1F						
Step	Feature	X/R Location	Y/A Location	Z Location	Size	Reference
1	Point	247.83625	54.96446	40.42642		
2	Point	234.12297	54.88548	40.42642		
3	Circle	275.01619	67.51404	40.42642	7.60358	
4	Circle	274.4915	41.02051	40.42642	7.51913	
5	Circle	249.61559	54.80804	40.42642	2.57126	
6	Midpoint	290.65448	54.05919	40.42642	2.69254	
7	Line	240.97961	54.92497	40.42642	-179.67	1 2
8	Line	270.13503	54.43361	40.42642	-1.04537	5 6
9	Line	262.31589	61.16104	40.42642	26.57535	5 3
10	Line	262.05355	47.91428	40.42642	-28.9975	5 4
11	Line	274.75384	54.26728	40.42642	-91.1346	3 4
12	Width	275.05188	61.31773	40.42642	12.39282	7 3
13	Width	274.4509	48.06902	40.42642	14.09724	7 4
14	Width	261.29667	54.69789	40.42642	26.92612	11 1
15	Angularity				0.98521	7 8

DCB_2B						
Step	Feature	X/R Location	Y/A Location	Z Location	Size	Reference
1	Point	146.59592	53.0558	38.98292		
2	Point	139.59794	53.10081	38.98292		
3	Circle	174.444	65.54132	38.98292	7.6804	
4	Circle	174.04963	39.12034	38.98292	7.68692	
5	Circle	149.04171	52.8524	38.98292	2.76957	
6	Midpoint	190.07008	52.23448	38.98292	2.70687	
7	Line	143.09693	53.07831	38.98292	179.6315	1 2
8	Line	169.5559	52.54344	38.98292	-0.86286	5 6
9	Line	161.74286	59.19686	38.98292	26.54298	5 3
10	Line	161.54567	45.98637	38.98292	-28.7716	5 4
11	Line	174.24681	52.33083	38.98292	-90.8552	3 4
12	Width	174.40328	59.20927	38.98292	12.66436	7 3
13	Width	174.09387	45.9995	38.98292	13.75861	7 4
14	Width	160.4237	52.8494	38.98292	27.65863	11 1
15	Angularity				0.35405	7 8

DCB_2D						
Step	Feature	X/R Location	Y/A Location	Z Location	Size	Reference
1	Point	260.44178	42.02816	40.42592		
2	Point	245.32411	41.67824	40.42592		
3	Circle	287.37308	55.50119	40.42592	7.57261	
4	Circle	287.65978	29.11191	40.42592	7.6394	
5	Circle	262.21565	42.02044	40.42592	2.50781	
6	Midpoint	303.33391	42.52871	40.42592	2.77392	
7	Line	252.88294	41.8532	40.42592	-178.674	1 2
8	Line	282.77478	42.27458	40.42592	0.70821	5 6
9	Line	274.79436	48.76082	40.42592	28.18488	5 3
10	Line	274.93771	35.56618	40.42592	-26.9	5 4
11	Line	287.51643	42.30655	40.42592	-89.3776	3 4
12	Width	287.52171	49.0798	40.42592	12.84622	7 3
13	Width	287.50309	35.88141	40.42592	13.54263	7 4
14	Width	273.97902	42.17523	40.42592	27.07608	11 1
15	Angularity				0.44336	7 8

DCB_2E						
Step	Feature	X/R Location	Y/A Location	Z Location	Size	Reference
1	Point	218.60944	89.13698	40.42542		
2	Point	187.16153	89.13693	40.42542		
3	Circle	245.95255	102.1619	40.42542	7.71538	
4	Circle	245.95887	75.74434	40.42542	7.63749	
5	Circle	220.76242	88.97617	40.42542	2.64294	
6	Midpoint	261.76114	88.99635	40.42542	2.80755	
7	Line	202.88548	89.13695	40.42542	-180	1 2
8	Line	241.26178	88.98626	40.42542	0.0282	5 6
9	Line	233.35749	95.56903	40.42542	27.62973	5 3
10	Line	233.36065	82.36025	40.42542	-27.7061	5 4
11	Line	245.95571	88.95312	40.42542	-89.9863	3 4
12	Width	245.95256	95.64946	40.42542	13.02487	7 3
13	Width	245.95886	82.44068	40.42542	13.39268	7 4
14	Width	232.28255	89.14025	40.42542	27.34623	11 1
15	Angularity				0.02011	7 8

DCB_2F						
Step	Feature	X/R Location	Y/A Location	Z Location	Size	Reference
1	Point	268.55442	45.63084	40.42642		
2	Point	249.71296	45.83313	40.42642		
3	Circle	295.67798	58.56641	40.42642	7.52863	
4	Circle	295.12096	32.16441	40.42642	7.56104	
5	Circle	270.15719	45.9477	40.42642	2.42642	
6	Midpoint	311.00942	45.04878	40.42642	2.6794	
7	Line	259.13369	45.73198	40.42642	179.3849	1 2
8	Line	290.5833	45.49824	40.42642	-1.26054	5 6
9	Line	282.91759	52.25705	40.42642	26.31001	5 3
10	Line	282.63907	39.05605	40.42642	-28.9045	5 4
11	Line	295.39947	45.36541	40.42642	-91.2086	3 4
12	Width	295.60699	51.95378	40.42642	13.22602	7 3
13	Width	295.19171	38.75425	40.42642	13.18044	7 4
14	Width	281.97377	45.34772	40.42642	26.84468	11 1
15	Angularity				0.46028	7 8

DCB_3B						
Step	Feature	X/R Location	Y/A Location	Z Location	Size	Reference
1	Point	198.73523	58.97516	40.42642		
2	Point	187.26458	58.97515	40.42642		
3	Circle	226.96377	71.37844	40.42642	7.8768	
4	Circle	226.38148	44.91728	40.42642	7.81428	
5	Circle	201.43293	58.666	40.42642	2.7623	
6	Midpoint	242.4531	57.89107	40.42642	2.88702	
7	Line	192.9999	58.97515	40.42642	-180	1 2
8	Line	221.94301	58.27853	40.42642	-1.08227	5 6
9	Line	214.19835	65.02222	40.42642	26.46986	5 3
10	Line	213.90721	51.79164	40.42642	-28.8584	5 4
11	Line	226.67263	58.14786	40.42642	-91.2606	3 4
12	Width	226.96378	65.17681	40.42642	12.40326	7 3
13	Width	226.38148	51.94623	40.42642	14.0579	7 4
14	Width	212.70626	58.66772	40.42642	27.94884	11 1
15	Angularity				0.77495	7 8

DCB_3D						
Step	Feature	X/R Location	Y/A Location	Z Location	Size	Reference
1	Point	229.8976	49.63743	40.42592		
2	Point	215.26153	49.63741	40.42592		
3	Circle	257.47349	61.89386	40.42542	7.62185	
4	Circle	257.37249	35.47557	40.42542	7.65344	
5	Circle	232.11396	48.76211	40.42542	2.59353	
6	Midpoint	273.21775	48.69334	40.42542	2.82091	
7	Line	222.57957	49.63742	40.42592	-180	1 2
8	Line	252.66585	48.72772	40.42542	-0.09586	5 6
9	Line	244.79372	55.32798	40.42542	27.37617	5 3
10	Line	244.74322	42.11884	40.42542	-27.7453	5 4
11	Line	257.42299	48.68472	40.42542	-90.2191	3 4
12	Width	257.4735	55.76567	40.42567	12.25639	7 3
13	Width	257.37248	42.55652	40.42567	14.16189	7 4
14	Width	243.66192	49.58481	40.42567	27.52884	11 1
15	Angularity				0.06883	7 8

DCB_3E						
Step	Feature	X/R Location	Y/A Location	Z Location	Size	Reference
1	Point	222.4737	70.53773	40.42542		
2	Point	186.98286	70.11118	40.42542		
3	Circle	250.19483	83.44002	40.42592	7.74107	
4	Circle	250.30666	56.98831	40.42592	7.74084	
5	Circle	225.10309	70.1449	40.42592	2.74596	
6	Midpoint	266.05719	70.37796	40.42592	2.8474	
7	Line	204.72828	70.32445	40.42542	-179.311	1 2
8	Line	245.58014	70.26143	40.42592	0.32605	5 6
9	Line	237.64896	76.79246	40.42592	27.91735	5 3
10	Line	237.70487	63.5666	40.42592	-27.5652	5 4
11	Line	250.25074	70.21416	40.42592	-89.7578	3 4
12	Width	250.27035	77.15636	40.42567	12.56822	7 3
13	Width	250.22324	63.92927	40.42567	13.88292	7 4
14	Width	236.36129	70.59644	40.42567	27.77542	11 1
15	Angularity				0.25913	7 8

DCB_3F						
Step	Feature	X/R Location	Y/A Location	Z Location	Size	Reference
1	Point	225.32283	54.91413	40.42642		
2	Point	207.45037	54.71459	40.42642		
3	Circle	251.97251	68.36936	40.42642	7.66605	
4	Circle	252.17496	41.93389	40.42642	7.59022	
5	Circle	226.91449	54.98006	40.42642	2.63841	
6	Midpoint	267.92121	55.36575	40.42642	2.73229	
7	Line	216.3866	54.81436	40.42642	-179.36	1 2
8	Line	247.41785	55.17291	40.42642	0.53888	5 6
9	Line	239.4435	61.67471	40.42642	28.11701	5 3
10	Line	239.54472	48.45697	40.42642	-27.3148	5 4
11	Line	252.07373	55.15162	40.42642	-89.5612	3 4
12	Width	252.04595	61.79133	40.42642	13.15687	7 3
13	Width	252.10083	48.57308	40.42642	13.27921	7 4
14	Width	238.69841	55.01656	40.42642	26.75194	11 1
15	Angularity				0.07214	7 8

DCB_4B						
Step	Feature	X/R Location	Y/A Location	Z Location	Size	Reference
1	Point	193.45338	58.68161	40.42642		
2	Point	180.31279	58.68161	40.42642		
3	Circle	220.73431	71.80131	40.42642	7.71944	
4	Circle	220.90175	45.34809	40.42642	7.76269	
5	Circle	195.54225	58.43485	40.42642	2.70967	
6	Midpoint	236.69916	58.79191	40.42642	2.74443	
7	Line	186.88309	58.68161	40.42642	-180	1 2
8	Line	216.1207	58.61338	40.42642	0.49706	5 6
9	Line	208.13828	65.11808	40.42642	27.94962	5 3
10	Line	208.222	51.89147	40.42642	-27.296	5 4
11	Line	220.81803	58.5747	40.42642	-89.6374	3 4
12	Width	220.73432	65.24147	40.42642	13.11968	7 3
13	Width	220.90174	52.01486	40.42642	13.33354	7 4
14	Width	207.13482	58.76821	40.42642	27.36342	11 1
15	Angularity				0.35703	7 8

DCB_4D						
Step	Feature	X/R Location	Y/A Location	Z Location	Size	Reference
1	Point	243.38482	46.62199	40.42542		
2	Point	218.06438	46.29396	40.42542		
3	Circle	270.76004	60.50066	40.42542	7.75065	
4	Circle	271.02046	33.93556	40.42542	7.71291	
5	Circle	245.59252	47.03604	40.42542	2.79525	
6	Midpoint	286.55574	47.49538	40.42542	3.08445	
7	Line	230.7246	46.45798	40.42542	-179.258	1 2
8	Line	266.07413	47.26571	40.42542	0.64246	5 6
9	Line	258.17628	53.76835	40.42542	28.14677	5 3
10	Line	258.30649	40.4858	40.42542	-27.2575	5 4
11	Line	270.89025	47.21811	40.42542	-89.4383	3 4
12	Width	270.84762	53.73979	40.42542	13.52289	7 3
13	Width	270.93598	40.4567	40.42542	13.04336	7 4
14	Width	257.13913	46.75683	40.42542	27.50995	11 1
15	Angularity				0.07133	7 8

DCB_4E						
Step	Feature	X/R Location	Y/A Location	Z Location	Size	Reference
1	Point	210.57856	68.95502	40.42592		
2	Point	196.66852	68.89101	40.42592		
3	Circle	238.34027	83.2419	40.42592	7.73745	
4	Circle	238.48491	56.59516	40.42592	7.77141	
5	Circle	213.15371	69.82095	40.42592	2.6943	
6	Midpoint	254.15602	70.01582	40.42567	2.87819	
7	Line	203.62354	68.92301	40.42592	-179.736	1 2
8	Line	233.65487	69.91839	40.42579	0.27229	5 6
9	Line	225.74699	76.53143	40.42592	28.05143	5 3
10	Line	225.81931	63.20806	40.42592	-27.5697	5 4
11	Line	238.41259	69.91853	40.42592	-89.689	3 4
12	Width	238.37285	76.16248	40.42592	14.15899	7 3
13	Width	238.45618	62.83916	40.42592	12.48813	7 4
14	Width	224.49778	69.03057	40.42592	27.83885	11 1
15	Angularity				0.0062	7 8

DCB_4F						
Step	Feature	X/R Location	Y/A Location	Z Location	Size	Reference
1	Point	224.13588	55.89026	40.42642		
2	Point	203.50901	55.89024	40.42642		
3	Circle	251.40133	69.72474	40.42642	7.74953	
4	Circle	251.35293	43.33345	40.42642	7.6941	
5	Circle	225.97278	56.50387	40.42642	2.46508	
6	Midpoint	267.20128	56.53194	40.42642	2.92642	
7	Line	213.82245	55.89025	40.42642	-180	1 2
8	Line	246.58703	56.51791	40.42642	0.03901	5 6
9	Line	238.68706	63.11431	40.42642	27.47094	5 3
10	Line	238.66286	49.91866	40.42642	-27.426	5 4
11	Line	251.37713	56.5291	40.42642	-90.1051	3 4
12	Width	251.40133	62.80751	40.42642	13.83446	7 3
13	Width	251.35293	49.61187	40.42642	12.55683	7 4
14	Width	237.75588	55.86528	40.42642	27.24003	11 1
15	Angularity				0.02804	7 8

DCB_5B						
Step	Feature	X/R Location	Y/A Location	Z Location	Size	Reference
1	Point	205.54849	57.61248	40.42642		
2	Point	194.27733	57.52796	40.42642		
3	Circle	232.40575	70.9274	40.42642	7.75285	
4	Circle	232.72866	44.50771	40.42642	7.70983	
5	Circle	207.40176	57.5307	40.42642	2.72098	
6	Midpoint	248.42329	58.06637	40.42642	2.74438	
7	Line	199.91291	57.57022	40.42642	-179.57	1 2
8	Line	227.91253	57.79853	40.42642	0.74814	5 6
9	Line	219.90376	64.22905	40.42642	28.18162	5 3
10	Line	220.06521	51.01921	40.42642	-27.212	5 4
11	Line	232.56721	57.71756	40.42642	-89.2997	3 4
12	Width	232.45491	64.371	40.42642	13.11315	7 3
13	Width	232.67877	51.16163	40.42642	13.30821	7 4
14	Width	219.05647	57.77758	40.42642	27.01799	11 1
15	Angularity				0.22805	7 8

DCB_5D						
Step	Feature	X/R Location	Y/A Location	Z Location	Size	Reference
1	Point	205.67424	46.09391	40.42542		
2	Point	178.48202	45.76732	40.42542		
3	Circle	233.05455	60.06474	40.42542	7.6327	
4	Circle	233.39124	33.58688	40.42542	7.59559	
5	Circle	208.15081	46.48958	40.42542	2.57044	
6	Midpoint	249.18201	47.12533	40.42542	2.74738	
7	Line	192.07813	45.93062	40.42542	-179.312	1 2
8	Line	228.66641	46.80746	40.42542	0.88768	5 6
9	Line	220.60268	53.27716	40.42542	28.59503	5 3
10	Line	220.77103	40.03823	40.42542	-27.0758	5 4
11	Line	233.2229	46.82581	40.42542	-89.2715	3 4
12	Width	233.13646	53.24474	40.42542	13.64099	7 3
13	Width	233.31415	40.00592	40.42542	12.83901	7 4
14	Width	219.45099	46.2691	40.42542	27.55574	11 1
15	Angularity				0.14293	7 8

DCB_5E						
Step	Feature	X/R Location	Y/A Location	Z Location	Size	Reference
1	Point	164.1331	69.82115	40.42592		
2	Point	132.90198	69.95166	40.42592		
3	Circle	191.04696	83.40865	40.42542	7.67761	
4	Circle	191.1124	56.96127	40.42542	7.65019	
5	Circle	165.89411	70.19276	40.42542	2.63365	
6	Midpoint	206.91396	70.26844	40.42542	2.9839	
7	Line	148.51754	69.88641	40.42592	179.7606	1 2
8	Line	186.40404	70.2306	40.42542	0.10571	5 6
9	Line	178.47054	76.80071	40.42542	27.71848	5 3
10	Line	178.50326	63.57702	40.42542	-27.685	5 4
11	Line	191.07968	70.18496	40.42542	-89.8582	3 4
12	Width	191.01834	76.55878	40.42567	13.69986	7 3
13	Width	191.13903	63.33473	40.42567	12.74702	7 4
14	Width	177.60676	69.85448	40.42567	26.9474	11 1
15	Angularity				0.2471	7 8

DCB_5F						
Step	Feature	X/R Location	Y/A Location	Z Location	Size	Reference
1	Point	206.56876	48.36822	40.42642		
2	Point	192.17869	48.72425	40.42642		
3	Circle	234.49144	60.68621	40.42642	7.66599	
4	Circle	233.68073	34.23318	40.42642	7.57398	
5	Circle	209.08269	48.32301	40.42642	2.60674	
6	Midpoint	249.94422	47.01278	40.42642	2.85159	
7	Line	199.37373	48.54624	40.42642	178.5827	1 2
8	Line	229.51346	47.6679	40.42642	-1.83657	5 6
9	Line	221.78707	54.50461	40.42642	25.94629	5 3
10	Line	221.38171	41.27809	40.42642	-29.8042	5 4
11	Line	234.08609	47.45969	40.42642	-91.7554	3 4
12	Width	234.33061	54.18578	40.42642	13.00485	7 3
13	Width	233.84719	40.96119	40.42642	13.46015	7 4
14	Width	220.32842	47.94653	40.42642	27.53224	11 1
15	Angularity				0.29918	7 8

DCB_6D						
Step	Feature	X/R Location	Y/A Location	Z Location	Size	Reference
1	Point	223.24772	45.7519	40.42542		
2	Point	203.83879	46.17592	40.42542		
3	Circle	251.26298	58.19484	40.42542	7.56147	
4	Circle	250.67429	31.74527	40.42542	7.5294	
5	Circle	225.74559	45.52711	40.42542	2.55413	
6	Midpoint	266.83849	44.67577	40.42542	2.70682	
7	Line	213.54326	45.96391	40.42542	178.7485	1 2
8	Line	246.29204	45.10144	40.42542	-1.18685	5 6
9	Line	238.50429	51.86097	40.42542	26.40142	5 3
10	Line	238.20994	38.63619	40.42542	-28.936	5 4
11	Line	250.96863	44.97006	40.42542	-91.275	3 4
12	Width	251.12045	51.67046	40.42542	13.05187	7 3
13	Width	250.82067	38.44579	40.42542	13.40425	7 4
14	Width	237.11001	45.44336	40.42542	27.73144	11 1
15	Angularity				0.0464	7 8

DCB_6E						
Step	Feature	X/R Location	Y/A Location	Z Location	Size	Reference
1	Point	206.91418	68.77649	40.42542		
2	Point	190.89171	69.34507	40.42542		
3	Circle	234.3522	81.40608	40.42542	7.51995	
4	Circle	233.49843	55.01631	40.42542	7.61023	
5	Circle	208.66595	69.02499	40.42542	2.53683	
6	Midpoint	249.74243	67.74541	40.42542	2.63437	
7	Line	198.90295	69.06078	40.42542	177.9676	1 2
8	Line	229.20419	68.3852	40.42542	-1.78426	5 6
9	Line	221.50907	75.21553	40.42542	25.73463	5 3
10	Line	221.08219	62.02065	40.42542	-29.4285	5 4
11	Line	233.92532	68.21119	40.42542	-91.853	3 4
12	Width	234.11114	74.613	40.42542	13.59471	7 3
13	Width	233.72555	61.41665	40.42542	12.80873	7 4
14	Width	220.41476	68.33971	40.42542	27.01529	11 1
15	Angularity				0.17797	7 8

DCB_6F						
Step	Feature	X/R Location	Y/A Location	Z Location	Size	Reference
1	Point	210.89146	64.32839	40.42642		
2	Point	188.88518	65.1865	40.42642		
3	Circle	238.28753	77.05183	40.42642	7.52752	
4	Circle	237.41856	50.62731	40.42642	7.46586	
5	Circle	212.68724	64.71303	40.42642	2.52416	
6	Midpoint	253.72264	63.39441	40.42642	2.54252	
7	Line	199.88832	64.75745	40.42642	177.7669	1 2
8	Line	233.20494	64.05372	40.42642	-1.84049	5 6
9	Line	225.48738	70.88243	40.42642	25.73309	5 3
10	Line	225.0529	57.67017	40.42642	-29.6637	5 4
11	Line	237.85305	63.83957	40.42642	-91.8835	3 4
12	Width	238.01904	70.16644	40.42642	13.78125	7 3
13	Width	237.66515	56.95103	40.42642	12.65707	7 4
14	Width	224.36572	63.88529	40.42642	26.96309	11 1
15	Angularity				0.2813	7 8

A3. Data Processing MATLAB Code

Full crack propagation script for DCB testing

VIDEO TO FRAME

```
%%------------------Code by: Luis A Camacho------------------------------%%
clc
clear all
close all;
imtool close all

% Input name of specimen
specimen = input('Specimen Name:','s');
xls_filename = [specimen,'.xlsx'];
vid_filename = [specimen, '_Trim.mp4'];

% Load Video and Raw Data
cd RawData\
[rawdata] = xlsread(xls_filename);
cd ..
cd DCBVideos\
Vidorig = VideoReader(vid_filename);
cd ..
load = rawdata(:,2); % Load data from excel file
deflection = rawdata(:,3); % deflection data from excel file

TNF = Vidorig.NumFrames; % total number of frames in the video
frames = length(load)-1; % number of frames to be extracted (dependant on on
the number of data points from Instron
TNFoF= TNF/(frames); % TNF over the number of frames to be extracted
frames_indx = round(TNFoF : TNFoF : TNF);
frames_indx = [1, frames_indx];
% Read frames individual frames and apply mask
% Section break to modulate blue filter (0-255)
for x = 1:length(frames_indx)
    img = read(Vidorig, frames_indx(1, x));
    % Apply Binary mask
    binary_imgs(:, :, x) = crackcreateMask(img);
end

% Notification sound that binary conversion is done
% Define the frequency and duration of the sound
```

```
frequency = 440; % Hz
duration = 1; % seconds
% Generate a time vector
fs = 44100; % sample rate (in samples per second)
t = linspace(0, duration, duration * fs);
% Generate the audio data for a sine wave
audio_data = sin(2 * pi * frequency * t);
% Play the sound
sound(audio_data, fs);
```

CALIBRATION

```
% Find index of critical load (max)
[maxload criticalindx] = max(load);
binary_im = binary_imgs(:, :, criticalindx-1);

% Mark ROIs for calibration dots
imshow(binary_im)
troiMask = roipoly();
broiMask = roipoly();
```

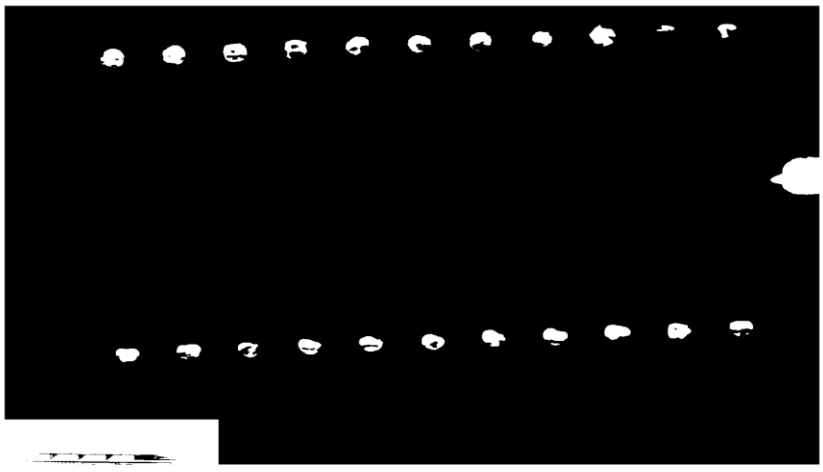

```
close;
% Detect circles
troiBinaryImg = binary_im & troiMask;
broiBinaryImg = binary_im & broiMask;
[tcenters,tradii] = imfindcircles(troiBinaryImg, [16
35],'ObjectPolarity','bright','Sensitivity',0.91);
```

```
 [bcenters,bradii] = imfindcircles(broiBinaryImg, [16
35],'ObjectPolarity','bright','Sensitivity',0.91);

 % Show preview of the circles
 figure(1)
 imshow(binary_im);
 hold on;
 viscircles(tcenters,tradii,'LineWidth',2,'Color','r');
 viscircles(bcenters,bradii,'LineWidth',2,'Color','r');
 hold off;

 % Prompt the image with circles for preview
 ginput(1);
```

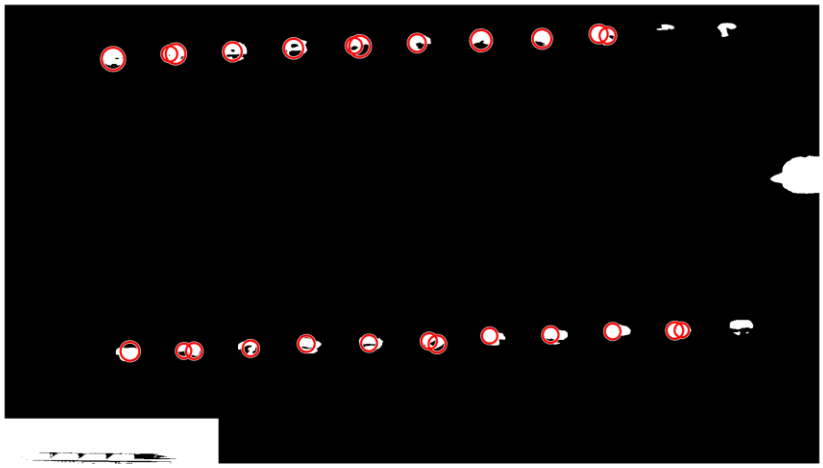

```
 close;

 % Sorting rows in preparation for stacked cricles portion
 tcenters = sortrows(tcenters, 1); % Ordered top row values
 bcenters = sortrows(bcenters, 1); % Ordered bottom row values
 last_val = tcenters(end, :);
 xmin = 80; % minimum x distance calibration threshold

 % Add zero at the beginning of array (for loop requirement)
 tcenters = [zeros(1,size(tcenters,2)); tcenters];
 bcenters = [zeros(1,size(bcenters,2)); bcenters];

 % Repeat last value of the array if needed (for loop requirment)
 if xmin < (tcenters(end, 1)-tcenters(end-1, 1))
 last_val = tcenters(end, :);
 tcenters(end+1, :) = last_val(1, :);
```

```
 end
 if xmin < bcenters(end, 1)-bcenters(end-1, 1)
 last_val = bcenters(end, :);
 bcenters(end+1, :) = last_val(1, :);
 end

 % Averging stacked circles
 x = 0;
 y = 0;
 trvx = [];
 trvy = [];
 brvx = [];
 brvy = [];

 for i = 2:(length(tcenters)-1)
     cxd = tcenters(i+1, 1)-tcenters(i, 1); % For loop current x distances
     cxd2 = tcenters(i, 1)-tcenters(i-1, 1);
     if cxd < xmin
         x = (tcenters(i+1, 1) + tcenters(i, 1))/2;
         y = (tcenters(i+1, 2) + tcenters(i, 2))/2;
         if x ~= 0 && y ~= 0
         trvx = [trvx, x];
         trvy = [trvy, y];
         end
     elseif xmin < cxd2
         trvx = [trvx, tcenters(i, 1)];
         trvy = [trvy, tcenters(i, 2)];
     end
 end
 trv1 = [trvx', trvy']; % top row centers

 for i = 2:(length(bcenters)-1)
     cxd = bcenters(i+1, 1)-bcenters(i, 1); % Current x distance between i and
i+1 values
     cxd2 = bcenters(i, 1)-bcenters(i-1, 1); % Current x distance between i-1
and i values
     if cxd < xmin % if distance of next dot is less than threshold record
         x = (bcenters(i+1, 1) + bcenters(i, 1))/2;
         y = (bcenters(i+1, 2) + bcenters(i, 2))/2;
         if x ~= 0 && y ~= 0 % eliminate zero values
         brvx = [brvx, x];
         brvy = [brvy, y];
         end
     elseif xmin < cxd2 % record else if distance of previous dot more than
threshold
```

```
        brvx = [brvx, bcenters(i, 1)];
        brvy = [brvy, bcenters(i, 2)];
    end
end
brv1 = [brvx', brvy'];

% Show preview of the circles
figure(2)
imshow(binary_im);
hold on
plot(trvx', trvy','x', 'LineWidth', 3,'Color','r', 'MarkerSize', 15);
plot(brvx', brvy','x', 'LineWidth', 3,'Color','r', 'MarkerSize', 15);
hold off

% Prompt the image with circles for preview
ginput(1);
```

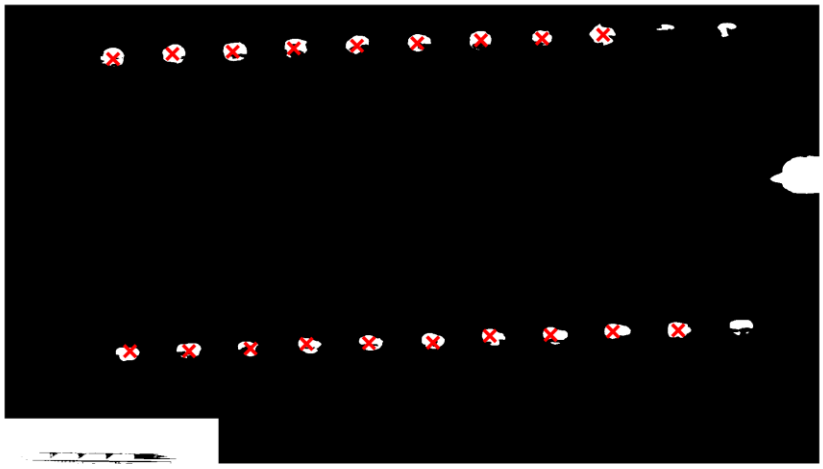

```
close;

% Use coordinates of centroids and the distance inbetween
d = [];
d2 = [];
for i = 1:(length(trv1)-1)
    d = [d (sqrt((trv1(i+1, 1)-trv1(i, 1))^2 + (trv1(i+1, 2)-trv1(i, 2))^2))];
end
for i = 1:(length(brv1)-1)
    d2 = [d2 (sqrt((brv1(i+1, 1)-brv1(i, 1))^2 + (brv1(i+1, 2)-brv1(i,
2))^2))];
end
```

```
d = (mean(d)+mean(d2))/2;

% Calculate the pixel size ratio using the selected circle
px_size = (5*0.997875)/ d; % Pixel size ration mm/p

% linear regression and slope extraction
pt = polyfit(trvx', trvy', 1);
ft = polyval(pt, trvx');
pb = polyfit(brvx', brvy', 1);
fb = polyval(pb, brvx');
m = abs((pt(1)+pb(1))/2); % Average slope

figure(3)
imshow(binary_im)
hold on
plot(trvx', trvy','x', trvx', ft, '-', 'LineWidth', 3,'Color','r',
'MarkerSize', 15);
plot(brvx', brvy','x', brvx', fb, '-', 'LineWidth', 3,'Color','r',
'MarkerSize', 15);
hold off

% Prompt the image with linear regression for preview
ginput(1);
```

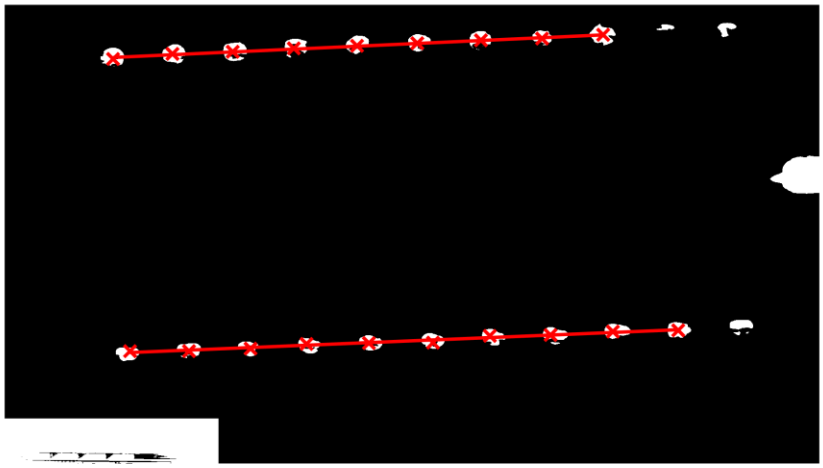

```
close;
```

CRACK PROPAGATION DETECTION

```
% Setup a region of interest where the crack will propagate
figure;
imshow(binary_im);

roiMask = roipoly();
```

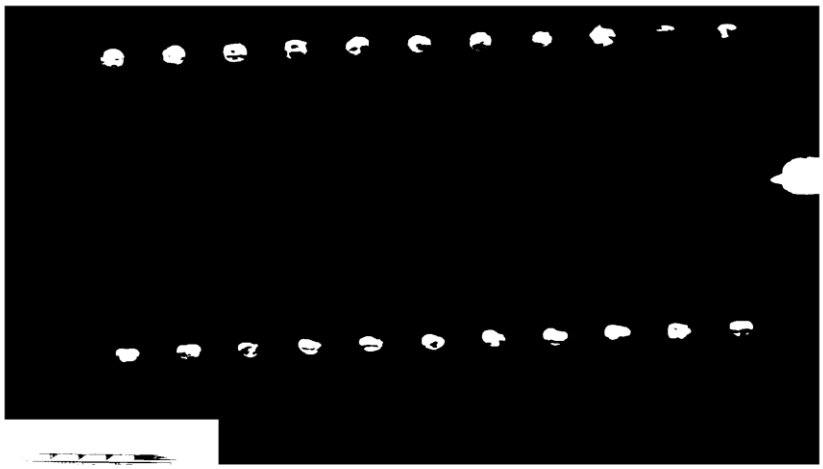

```
roiBinaryImg = binary_im & roiMask;

close;
% Extract crack initiation location with critical load frame
sz = size(binary_im); %Size of image
Pixels = find(roiBinaryImg == 1); % find the values withn the ROI that
correspond to the crack
[r,c] = ind2sub(sz, Pixels); % Get the indexes of the values
Cracktip_i = min(c); % Initial Find the tip of the crack
% Set up values for previous value cracktip as A_o
prevC = Cracktip_i;

for j = criticalindx:length(frames_indx)
    roiBinaryImgs = binary_imgs(:, :, j) & roiMask;
    Pixels = find(roiBinaryImgs==1);
    [r,c] = ind2sub(sz, Pixels);
    currA = min(c);

    % Check if the current A is less than the previous value
    if currA > prevC % in the video the crack moves negative along x axis
        % Replace with previous value
```

```
        Cracktip(j, 1) = prevC;
    else
        % Store the current value as the new previous value
        prevC = currA;
        Cracktip(j, 1) = currA;
    end
end

% Create a new figure
figure;
% Display the images and and the line of tip crack
for i = criticalindx:(length(frames_indx))
    % Display the current image and crack tip propagation
    imshow(binary_imgs(:,:,i));
    line([Cracktip(i) Cracktip(i)], [1 size(binary_im, 1)], 'Color', 'r',
'LineWidth', 2);
    % Pause for a short time to allow the image to be viewed
    pause(0.03);
end
```

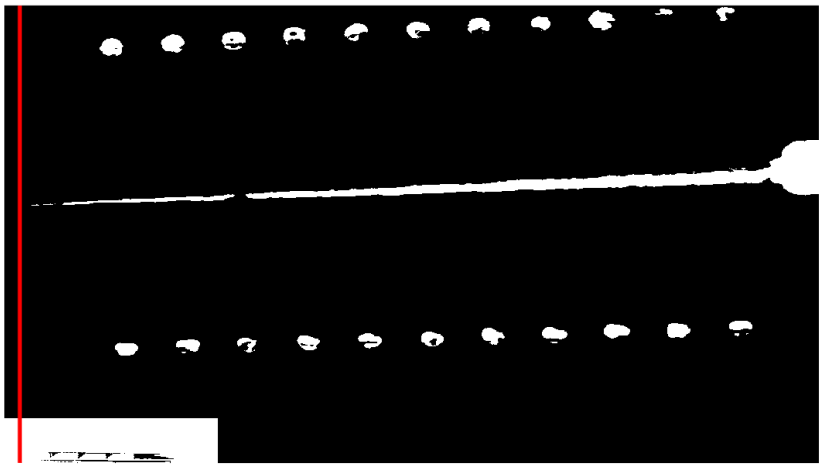

```
Cracktip = nonzeros(Cracktip);
for i = 2:length(Cracktip)
    x_crack(i, 1) = abs(Cracktip(i)-Cracktip_i).*px_size;
end
```

CALCULATIONS FOR FRACTURE TOUGHNESS, G_I, AND PLOTS FOR LOAD VS DEFLECTION AND FRACTURE TOUGHNESS

```
% Rotation Compensation & Notch tip to load vector distance
A_o = rawdata(1,4); % in millimeters
for i = 1:length(x_crack)
    y = x_crack(i)*m;
    x_crackcomp(i, 1) = (sqrt((x_crack(i)^2)+y^2)+A_o)/1000;
end

% Derive load and deflection curve to get max slope
dload = gradient(load);
[dload_max, index] = max(dload);
deflection_max = deflection(index);
deflection_maxslope = deflection(index(1));
load_maxslope = load(index(1));

% Find slope of linear region, E
span = 5; %span of linear region
q = index(1)-span; %Lower span of linear region
r = index(1)+span; %higher span of linear region
Linear_region_load = load(q:r);
Linear_region_deflection = deflection(q:r);
x = [ones(length(Linear_region_deflection),1) Linear_region_deflection];
slopeoflinearregion = (x)\Linear_region_load;

% Eliminate toe and shift to origin with slope of linear region and x intercept
E = slopeoflinearregion(2);
y_intercept = slopeoflinearregion(1);
x_intercept = y_intercept/E;
deflection_i = deflection+x_intercept;
for p = 1:index
    deflection_i(p) = (load(p)/E); % Units in meters
end
% convert deflection into meters
deflection_i = deflection_i/1000;

[load_peaks peakindxs] = findpeaks(load,'MinPeakHeight', 200,
'MinPeakProminence',1*10^-15);
deflection_peaks = deflection_i(peakindxs);
% Threshold peak values with critical index to not get peaks before max
% value
[critLoadpeak critical_peak] = max(load_peaks);
```

```
threshold = deflection_peaks(critical_peak);
deflection_peaks_filtered = deflection_peaks(deflection_peaks >= threshold);
load_peaks_filtered =  load_peaks(deflection_peaks >= threshold);
peakindxs_filtered = peakindxs(deflection_peaks >= threshold);
crack_peaks = x_crackcomp((peakindxs_filtered-criticalindx)+1); % millimeters

%%%%%%%%%%%%%%%%%%%%%%%%%%%%%%%%%%%%%%%%%%%%%%%%%%%%%%%%%%%%%%%%
%%%% Plot load vs deflection with peaks (corrected) %%%%
%%%%%%%%%%%%%%%%%%%%%%%%%%%%%%%%%%%%%%%%%%%%%%%%%%%%%%%%%%%%%%%%

clear xlim ylim
figure;
plot(deflection_i*1000,load,'k');
grid off
title(specimen, 'Peaks')
xlabel('Deflection (mm)')
ylabel('Load (N)')
ylim([0 1000])
xlim([0 2.5])
hold on
plot(deflection_peaks_filtered*1000 ,load_peaks_filtered,'x')
hold off
```

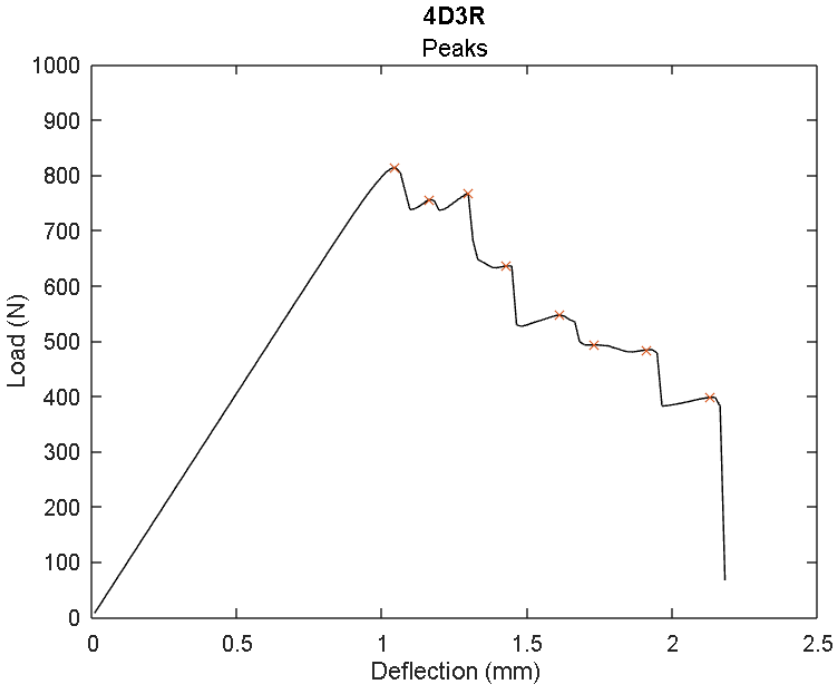


```
% Material and specimen constants
```

```
 E_m = 1.2411*10^10; % Material flexural modulus N/mm^2 (TechmerPM datasheet)
 h = 25.5/1000; % Nominal height of specimen meters
 bn = 14.7/1000; %Nominal bead width meters
 b = 12.7/1000; % Nominal interlayer width meters
 a_c = 0.6*h; % empirical correction factor, et al. Mostovoy, 1976

 % G_IC, et al. Mostovoy 1967
 for i = criticalindx:length(load)
     G_IM(i-criticalindx+1, 1) = ((load(i,
1)^2)/(2*bn))*(24/(3*E_m*b*(h^3)))*((3*((x_crackcomp(i-criticalindx+1,
1)+a_c)^2)) + (h^2));
 end

 % G_IC, Rigid Specimen Compliance Calibration
 for i = 2:(length(load_peaks_filtered))
     G_I(i-1, 1) = ((load_peaks_filtered(i,
1)^2)/(2*bn))*(24/(3*E_m*b*(h^3)))*((3*((crack_peaks(i, 1)+a_c)^2)) + (h^2));
 end

 crack_peaks_i = crack_peaks(2:(length(crack_peaks)));
 %%%%%%%%%%%%%%%%%%%%%%%
 %%%% Plot R curves %%%%
 %%%%%%%%%%%%%%%%%%%%%%%

 %%%%%%%%%%%%%%%%%%%%%%%
 %%%% Mostovoy Plot %%%%
 %%%%%%%%%%%%%%%%%%%%%%%
 clear xlim ylim
 figure
 plot(x_crackcomp*1000,G_IM,'o');
 title(specimen, 'et al. Mostovoy 1967')
 xlim([0 100])
 ylim([0 1000])
 xlabel('a, mm')
 ylabel('G_I, J/m^2')
```

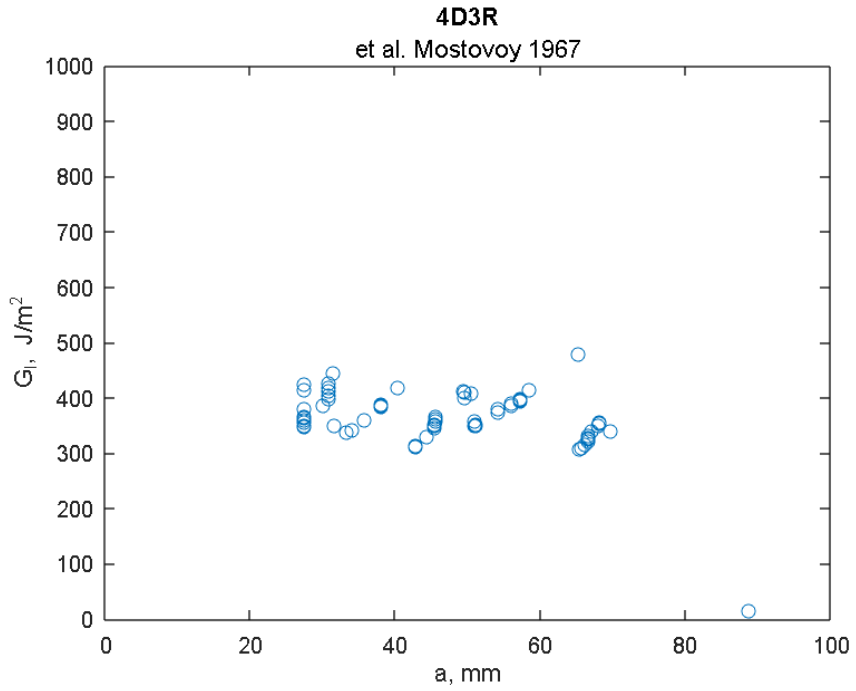


```
%%%%%%%%%%%%%%%%%%%
%%%% RBCC Plot %%%%
%%%%%%%%%%%%%%%%%%%
clear xlim ylim
figure
plot(crack_peaks_i*1000,G_I,'o');
title(specimen, 'RSCC')
xlim([0 100])
ylim([0 1000])
xlabel('a, mm')
ylabel('G_I, J/m^2')
```

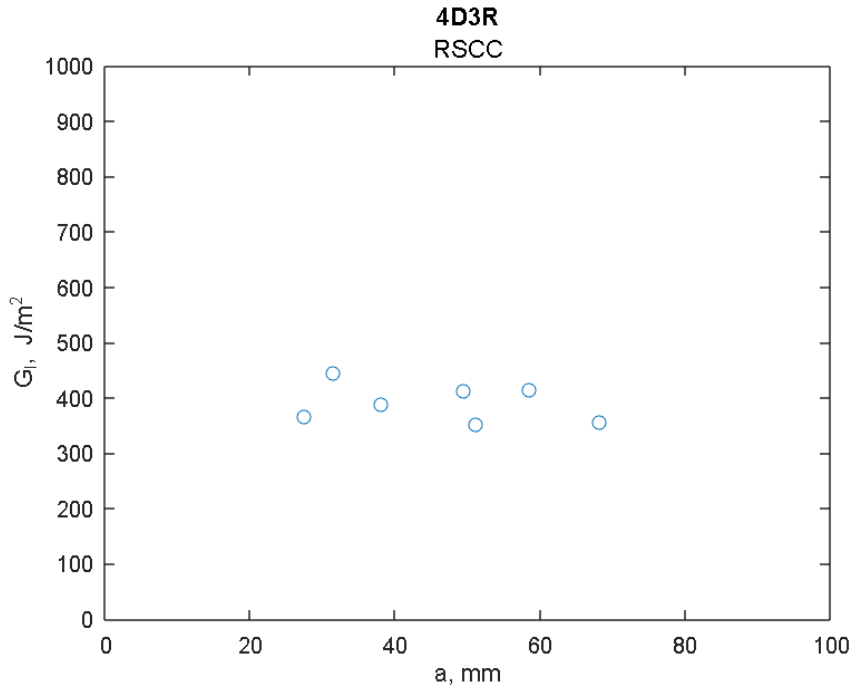

SAVE FIGURES

```
% Current folder path
currentFolder = pwd;
% Createa folder with specimen name (inputed at the beginnning)
mkdir(specimen);

% Save the figures in the new folder
cd(specimen);

% Plot load vs deflection (corrected)
clear xlim ylim
figure;
plot(deflection_i*1000,load,'k');
grid off
title(specimen, 'Peaks')
xlabel('Deflection (mm)')
ylabel('Load (N)')
ylim([0 1000])
xlim([0 2.5])
hold on
```

```
plot(deflection_peaks*1000 ,load_peaks,'x')
hold off
saveas(gcf, 'LvDPlot_peaks', 'png');

% Mostovoy Plot
clear xlim ylim
figure
plot(x_crackcomp*1000,G_I1,'o');
title(specimen, 'et al. Mostovoy 1967')
xlim([0 100])
ylim([0 1000])
xlabel('a, mm')
ylabel('G_I, J/m^2')
saveas(gcf, 'MostovoyRcurve', 'png');

% RBCC (Rigid Beam compliance calibration)
clear xlim ylim
figure
plot(crack_peaks_i*1000,G_I,'o');
title(specimen, 'RSCC')
xlim([0 100])
ylim([0 1000])
xlabel('a, mm')
ylabel('G_I, J/m^2')
saveas(gcf, 'Rigid_Specimen_ComplianceCalibration', 'png');

cd ..

clear figures
```

Vita

Luis Alfonso Camacho, born in El Paso, TX and raised in Nuevo Casas Grandes, Chihuahua, Mexico. Has a bachelor's degree in mechanical engineering from the University of Texas At El Paso (UTEP). He is working at the W.M. Keck Center for 3D Innovation within The University of Texas at El Paso (UTEP) under mentor Dr. David Espalin completing his master's degree in mechanical engineering. He has presented his research on Southwest Emerging Technologies Symposium on two occasions in the topics of material characterization process validation for large-scale additive manufacturing, AM, and generating breakable support structures in large-scale AM. He is currently pursuing a publication and has been selected to be in Fabric Freeform Symposium for his work in the validation of material characterization processes large-scale AM.

Contact Information: lacamacho@miners.utep.edu